MASTER

Energy analysis of a propeller in open water using control volumes in CFD simulations

Bergsma, S.

Award date:
2019

EINDHOVEN UNIVERSITY OF TECHNOLOGY

&

WÄRTSILÄ NETHERLANDS B.V.

GRADUATION THESIS FOR THE MASTER APPLIED PHYSICS. THE RESEARCH IS
CONDUCTED AT WÄRTSILÄ IN DRUNEN.

Energy analysis of a propeller in open water using control volumes in CFD simulations

Author:
S. Bergsma   (0843241)

Supervisors:
dr. M.J. Bijlard (Wärtsilä)
dr. ir. P.W. Stoltenkamp (Wärtsilä)
prof. dr. ir. G.J.F. van Heijst (TU/e)

Exam committee:
prof. dr. ir. G.J.F. van Heijst (TU/e)
dr. M.J. Bijlard (Wärtsilä)
dr. M. Duran Matute (TU/e)
dr. ir. L.P.J. Kamp (TU/e)
dr. ir. T.A.J. van Hooff (TU/e)

August 26, 2019

R-1991-A

Abstract

Improving the efficiency of a propeller is of great importance in the marine industry because of the stringent regulations and the increasing fuel costs. The efficiency of a propeller can be improved by optimizing the design of the propeller and by using Energy Saving Devices (ESDs). One of the most popular ESDs is the Propeller Boss Cap Fins (PBCF), because of its low costs and easy installation. In order to investigate whether an ESD can significantly increase the efficiency of a propeller, an analysis tool can be used to measure the energy losses. One of the methods that can be used is the control volume method.

The goal of this study is to analyse the energy losses of a propeller using the control volume method and to improve this method by using multiple control volumes. After this, the method will be used to investigate the effects of the PBCF and to evaluate when a PBCF can sufficiently increase the efficiency of a propeller.

First, we compare the result of our simulations to the results of a previous study. The simulations are performed using the SST $k - \omega$ model with the Sliding Mesh method to simulate the rotation. As a result of this comparison, it can be assumed that the control volume method can be used to measure the energy losses in transient $k - \omega$ simulations.

Hereafter, the same propellers were investigated using the Standard $k - \epsilon$ model with the Moving Reference Frame method to simulate the rotation. The quasi-steady $k - \epsilon$ simulations can be used to give a general indication of the large scale energy losses. This analysis method is most useful for propellers with similar geometries, considering that the relative difference between the losses is more important when comparing the propellers than the exact values of the energy losses.

Two different configurations with multiple control volumes are investigated. These simulations confirm that the choice of control volume affects the results. Therefore it is important to use identical control volumes when comparing propellers. Multiple control volumes in one simulation can also be useful to investigate the energy losses at different areas around the propeller.

The introduced methods are used to analyse the effects of the PBCF. The PBCF suppresses the hub vortex and as a result of this reduces the rotational losses. The multiple control volume configuration shows that the rotational losses are only reduced close to the hub. This implies that the percentage of rotational losses close to the hub can provide a good indication whether a PBCF can sufficiently increase the efficiency of a propeller.

After using the methods to analyse the energy losses for a propeller with a PBCF, it can be concluded that the control volume method can be a helpful tool to investigate whether an ESD can significantly enhance the efficiency of a propeller.

Contents

1 | Introduction

1.1   Energy saving in marine industries

The demand for energy is increasing every day, while the fossil fuel energy resources are finite. Because of this, the price of fuel is rising and expected to rise even more. The fuel price is a large burden to shipping companies, since fuel costs are a large portion of the operation costs. Therefore improving the efficiency and saving energy has been a hot topic in marine industries for years.

Not only the fuel price causes a high interest in saving energy. Because of global warming the regulations on the exhaust of gases from ships has been strengthened. The first international ship energy efficiency regulations were defined in 2013. As a result shipping companies are faced with several environmental requirements to lower environmental pollution [1].

Because of the rise of fuel prices and the strict regulations on emission and pollution, improving the efficiency of the propulsion system is one of the most important goals while designing a propeller. The efficiency of a propeller can be enhanced in different ways. For new build ships the propeller can be designed to be as efficient possible. A shipowner can also choose to buy a new propeller. Purchasing a new propeller can be very expensive, while the expected gains can be small. Because of this, investing in a new propeller usually is not feasible, as the payback time of a new propeller can be very long. Therefore shipowners are looking for cheaper ways to enhance the efficiency of their ship. Energy Saving Devices are often used to enhance the efficiency of a propeller.

1.2   Energy Saving Devices (ESDs)

ESDs are retrofitted structures and modifications of the propeller, hull or rudder with the primary goal of reducing the fuel consumption of the ship [2]. For more than 30 years ESDs have been designed and built to improve the fuel efficiency of ships [3]. ESDs can be divided in three categories, which are shown in Figure 1.1 [4]. They are divided by their placement around the propeller. This suggests that an ESD is always in just one of these areas and does not influence the other regions, which is a simplified representation. In reality, an ESD can have an effect in all regions and can also be placed in overlapping regions.

In Zone I the ESD is placed in front of the propeller. These devices are often called Pre-Swirl devices. These devices aim to modify the flow that enters the propeller by manipulating the boundary layer or by pre-swirling the flow. This can result in a more homogeneous velocity distribution in the wake field or a reduction of the rotational swirl in the downstream fluid [2].
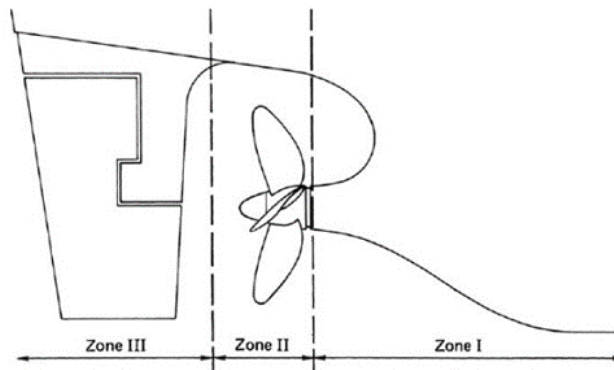
Figure 1.1: ESD Classification Zones [4]

The devices in Zone II operate directly on the propeller. This includes modification of the propeller blades or attachment of free rotating mechanisms that use the remaining kinetic energy in the propeller slipstream [2].

The last zone, Zone III, is situated behind the propeller. The devices used in this zone are often called Post-Swirl devices and take advantage of the kinetic energy found within the rotational swirl of the slipstream. From this kinetic energy they can create additional thrust [2].

Some of the most common ESDs are presented in Figure 1.2.

(a) Pre-Swirl Stator [5] **(b)** Mewis Duct [6]

(c) Propeller Boss Cap Fins [7] **(d)** Grim Vane Wheel [8]

Figure 1.2: Energy Saving Devices

In Figure 1.2a the Pre-Swirl Stator is shown. It is a set of fins radially attached to the hull. These provide pre-swirl to the propeller inflow, in a direction to meet the rotating blades of the propeller. This reduces the losses in the slipstream. As a result of the pre-swirl, the loading on the propeller is increased and translated into additional thrust. Power gains of up to 4.2% have been achieved using this ESD [9].

Figure 1.2b shows the Mewis Duct. This is the combination of a duct and the Pre-Swirl stator. The duct straightens and accelerates the flow into the propeller and also produces a net forward thrust. Again, the fins provides a pre-swirl to the flow which reduces the losses in the slipstream and increases the thrust. The Mewis duct is analysed using Computational Fluid Dynamics computations. In these computations an efficiency gain of 2.9 to 4.3% is found [10].

In Figure 1.2c the Propeller Boss Cap Fins installed on a propeller can be seen. A PBCF is a hubcap with small fins. The PBCF has been introduced in 1988 by Ouchi. More than 2000 sets have been sold since then [11]. The main goal of the PBCF is to reduce the hub vortex. When water passes a propeller, it is accelerated and twisted. This creates vortices at the root of the trailing edges. These root vortices travel around the hubcap and normally merge together after the hubcap. This results in a very strong vortex called the hub vortex. The PBCF disturbs the propeller root vortices and, by avoiding their merging, reduces the hub drag and increases the propulsion efficiency [12]. The original measured efficiency increase in model experiments by Ouchi was 1 to 2% [13]. More recently results were published where an increase of 1 to 1.5% was measured [14]. Model and full scale tests on the PBCF fitted to an Aframax tanker predict a higher efficiency enhancement of 3.5% [15].

The ESD that is shown in Figure 1.2d is the Grim Vane Wheel. This is a rotational device that freely rotates in the propeller slipstream to produce additional thrust. The inner part of the Grim Vane Wheel recovers kinetic energy from the rotational swirl in the flow of the slipstream. The outer part of the wheel behaves as a normal propeller. It therefore produces thrust from the energy in the slipstream [4]. The efficiency gain of the Grim Vane Wheel is estimated to be around 6% [16].

1.3 Costs and savings of Energy Saving Devices on an Aframax tanker

The ESDs discussed in the previous section are predicted to enhance the efficiency by 1 to 6%. This can have a large effect on the fuel costs and emission. In order to prove that an efficiency increase of 1% can have a big influence, we will calculate the savings of an Aframax tanker with an efficiency gain of 1, 2 and 5%. Consider an Aframax tanker, as shown in Figure 1.3, with a length of approximately 250 meters and a width of approximately 44 meters.

Figure 1.3: An Aframax tanker with a length of approximately 250 meters and a width of approximately 44 meters [17]

The propeller on this ship, with a diameter of 7.6 meters, rotates at 92 rotations per minute and requires 14500 kW. If we assume that the ship sails for 300 days per year, using the current fuel costs, this ship can save $476 000 over 10 years when the efficiency is increased by just 1% [18]. When the efficiency is increased by 2%, the savings are doubled to $952 000 and enhancing the efficiency by 5% results in a saving of $2 380 000. In Table 1.1 an estimation has been made for the costs and gains of the ESDs shown in the previous section for this Aframax tanker.

Table 1.1: Costs and gains of ESDs for an Aframax tanker

ESD	Efficiency gain	Cost of ESD [19]	Longest Payback Time	Shortest Payback Time
Pre-Swirl Stator	4.2%	$250 000 - $300 000	1.50 years	1.25 years
Mewis Duct	2.9 to 4.3%	$525 000 - $575 000	3.80 years	2.56 years
PBCF	1.0 to 3.5%	$100 000 - $150 000	3.15 years	1.00 years
Grim Vane Wheel	6%	$525 000 - $575 000	2.01 years	1.84 years

The payback time of these ESDs ranges from 1 year to almost 4 years. So after a maximum of 4 years, the shipowners will profit from the ESD that has been installed on their ship. Shipowners often do not invest in ESDs. The big barrier towards implementing different Energy Saving Devices is the lack of known performance and the low confidence in their reliability [20]. The price of an ESD can be high, as presented in Table 1.1. The Grim Vane Wheel is predicted to have a high efficiency gain and the payback time is relatively short. From this calculation we can conclude that the shipowners should invest in the Grim Vane Wheel. Every ship and propeller, however, is different and because of this the efficiency gain is only a rough estimation. Combining this with the lack of knowledge of the working principles of ESDs can keep the shipowners from investing in these devices.

The Propeller Boss Cap Fins, in comparison to the other ESDs, is relatively inexpensive. The payback time is still reasonable and the risk is smaller due to the lower price. Because of this, shipowners will be less reluctant to install this device. Another big advantage of the PBCF in comparison with the other ESDs is the easy installation. It can be installed in 5-6 hours by 4 workers [21]. The installation can be done underwater, therefore the PBCF can be installed at every stop and the ship does not have to be in a drydock [22]. Because of the lower price and easy and fast installation, the PBCF is known to be one of the most used ESDs [23]. Since early 1990 more than 3100 PBCFs were installed on vessels all around the world [24].

1.4 Analysis of energy losses

Many ESDs are available in the market, however, there are uncertainties on their working principles. More knowledge about the working principles of ESDs and the efficiency increase of the propeller is desired. The way in which the efficiency increase as a result of a device can be measured accurately is still under discussion and no methodology that provides an accurate answer before sea trials has been found yet [25].

Model tests are often used to test the efficiency of a propeller. The main issue with experiments is that Froude and Reynolds number similarities cannot be achieved when conducting the experiments. Because of this corrections for scaling effects need to be made. Model tests with ESDs are even more difficult. In full scale ESDs mostly operate in the boundary layer. This boundary layer is thinner in full scale than in model scale. This can lead to wrong outcomes from the experiments due to scaling issues [2]. Computational Fluid Dynamics (CFD) can be a good alternative for experiments.

Different methods have been used in CFD to determine the energy losses. The first studies were based on potential flow assumptions. In 1995 Dyne suggested a propulsive efficiency based on wake losses and gains [26]. A disadvantage of the potential flow method is that it assumes that the flow is inviscid. As a consequence this does not take into account viscous effects, which is one of the main components of energy losses. More recently Schuiling & van Terwisga introduced a method using control volumes in RANS simulations [27]. These simulations include viscosity. In their method a control volume is placed around a propeller. Based on the conservation of mass, Newton's second law and the first law of thermodynamics they formulated an energy equation. From this equation they derived the different energy losses in the control volume using surface and volume integrals.

Using control volumes has disadvantages. The results are affected by the choice of the control volume. Many interesting flow phenomena, such as viscous dissipation, occur close to the propeller, while other processes will occur in their own specific region. It is difficult to correctly investigate the regions in which the losses occur using control volumes. The control volume method, however, is an easy and computational inexpensive method to give a general idea about the different energy losses of the propeller. This analysis method could be improved by using multiple control volumes in one simulation.

1.5 Goal of the research

Improving the efficiency of a propeller is of great importance in the marine industry because of the stringent regulations and the increasing fuel costs. The efficiency of a propeller can be improved by optimizing the design of the propeller and by using Energy Saving Devices. One of the most popular ESDs is the PBCF, because of its low costs and easy installation. In order to investigate whether an ESD can significantly increase the efficiency, an analysis tool can be used to measure the energy losses. One of these methods is the control volume method. The biggest disadvantage of this method is the influence of the choice of the control volume.

The goal of this study is to analyse the energy losses of a propeller using the control volume method and to improve this method by using multiple control volumes. After this, the method will be used to investigate the effects of the PBCF and to evaluate when a PBCF can sufficiently increase the efficiency of a propeller.

In Chapter 2 the relevant theory will be discussed. The numerical methods that have been used will be explained in Chapter 3. The results of the energy analysis of different propellers will be discussed in Chapter 4. The PBCF will be investigated in Chapter 5. In Chapter 6 the conclusion will be presented.

2 | Theory

In the previous chapter it was explained that understanding the energy losses is important to be able to save energy in maritime industries. The first studies of energy losses were based on potential flows, which does not take into account viscous effect. More recently the control volume method was presented, which does take viscous effects into account. This study will focus on analysing the energy losses of a propeller in open water by using the control volume method. In this chapter the relevant theory for this method will be presented.

In section 2.1.1 the momentum theory of Rankine will be explained. From this theory the ideal efficiency can be derived. Unfortunately the ideal efficiency is never the actual efficiency of the propeller. Section 2.1.2 will give a short introduction into the efficiency of the propeller and the different energy losses. After understanding the efficiency, the open water characteristics will be explained in section 2.1.3 which are used to characterise the performance of a propeller.

After the explanation of the efficiency and the performance of a propeller, the relevant theory of the control volume method will be explained. The control volume method is based on the conservation of mass, linear momentum and energy. The conservation laws will be explained in section 2.2. In section 2.2.4 the conservation of energy will be applied on a propeller and the different losses will be explained further.

2.1 Propeller efficiency and performance

Numerous models to calculate the optimal propeller efficiency have been developed. The basic concepts and implications for the understanding of the propeller efficiency and performance will be discussed in this section.

2.1.1 Momentum theory

A basic model for a propeller was first developed in the 19th century by Rankine [28]. The propeller is modelled by a pressure jump over an infinitesimally thin disk, called the actuator disk. This simple model calculates the 1D characteristics of the flow at the disk and far up- and downstream of the propeller. All effects of gravity and viscosity are neglected in this approach.

Consider an actuator disk with area A placed in a purely axial flow with a constant inlet velocity v_{in}, as shown in Figure 2.1. The only force that acts on the fluid is the thrust T generated by the propeller. The propeller induces a velocity v_p, therefore the total velocity at the disk is $v_a = v_{in} + v_p$. The flow is assumed to be incompressible. The pressure far upstream and downstream is assumed to be equal to the free-stream static pressure p_0.

Bernoulli's conservation of head, H, can be applied upstream and downstream of the actuator disk to find the relation between the thrust, T, and the velocity far downstream of the disk, $v_{out} = v_{in} + v_b$. In the upstream situation Bernoulli's conservation of head can be described as

$$H = p_0 + \frac{1}{2}\rho v_{in}^2 = p_{before} + \frac{1}{2}\rho v_a^2, \tag{2.1}$$

where p_{before} is the pressure just before the disk and ρ is the density of the fluid. For the downstream situation Bernoulli's conservation of head is

$$H = p_0 + \frac{1}{2}\rho v_{out}^2 = p_{after} + \frac{1}{2}\rho v_a^2, \tag{2.2}$$

where p_{after} is the pressure just after the disk. Subtracting equation (2.1) from equation (2.2) gives the pressure jump over the disk, which is coupled to the thrust generated by the propeller. The thrust is a
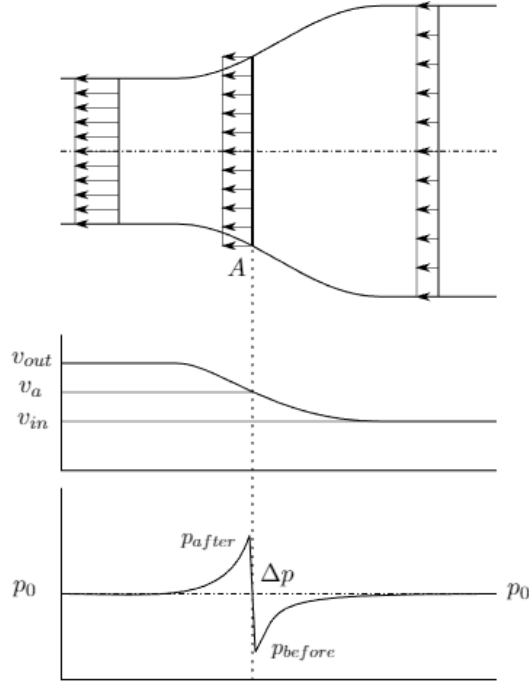
Figure 2.1: Diagram of the momentum theory, with p_0 the atmospheric pressure, p_{before} the pressure just before the actuator disk, p_{after} the pressure just after the actuator disk, Δp the pressure jump, v_{in} the inflow velocity, v_a the velocity at the disk, v_{out} the outflow velocity and A the actuator disk area [29]

result of the pressure difference over the actuator disk and therefore can be expressed as the product of the pressure difference and the disk area. The pressure jump is given by

$$\Delta p = p_{after} - p_{before} = \frac{1}{2}\rho(v_{out}^2 - v_{in}^2) = \rho v_b(\frac{1}{2}v_b + v_{in}) = \frac{T}{A}. \tag{2.3}$$

The force, which is only the thrust in this model, is also equal to the change of axial momentum of the flow per unit time [4]. Therefore, another formulation for the thrust is

$$T = \dot{m}(v_{out} - v_{in}) = \rho A v_a(v_{out} - v_{in}) = \rho A(v_{in} + v_p)v_b, \tag{2.4}$$

where $\dot{m}$ is the mass flow per unit time. The delivered power, P_d, is equal to the change per unit time of kinetic energy by the flow, which can be defined as

$$P_d = \frac{\dot{m}}{2}(v_{out}^2 - v_{in}^2) = \frac{1}{2}\rho A(v_{in} + v_p)v_b(v_b + 2v_{in}). \tag{2.5}$$

Furthermore, since friction is neglected, the work done by the thrust of the propeller is equal the delivered power, resulting in

$$P_d = Tv_a = \rho A(v_{in} + v_p)v_b(v_{in} + v_p). \tag{2.6}$$

By substituting equation (2.6) into equation (2.5) it can be derived that

$$v_p = \frac{1}{2}v_b. \tag{2.7}$$

This means that half of the acceleration takes place before the actuator disk and half afterwards.

2.1.2 Propeller efficiency

Even if all energy supplied to the propeller would be converted into axial thrust, the efficiency of the propeller would still not be equal to 100%. The highest possible efficiency, which can only hypothetically be obtained by a propeller in open water with uniform loading, no slipstream rotation and no viscous losses, is known to be the ideal efficiency. Such a hypothetical propeller is known as the actuator disk, which was explained in Section 2.1.1.

The efficiency of a propeller is given by the ratio of useful power over delivered power [27]. As a result the ideal efficiency, derived from Rankine's momentum theory, is defined as

$$\eta_i = \frac{P_{useful}}{P_d} = \frac{Tv_{in}}{Tv_a} = \frac{1}{1 + \frac{v_p}{v_{in}}}. \tag{2.8}$$

From equation (2.3) and equation (2.7) a relation for $\frac{v_p}{v_{in}}$ can be derived, which is given by

$$\frac{v_p}{v_{in}} = -\frac{1}{2} \pm \frac{1}{2}\sqrt{1 + \frac{T}{\frac{1}{2}A\rho}}. \tag{2.9}$$

Ship propellers usually generate thrust in the direction of travel. Therefore the direction of v_p is the same as the direction of v_{in}. This leaves only one physically correct relation between v_p and v_{in} Because of this, the ideal efficiency can be rewritten into

$$\eta_i = \frac{2}{1 + \sqrt{1 + C_t}}, \tag{2.10}$$

where C_t is the dimensionless thrust coefficient defined as

$$C_t = \frac{T}{\frac{1}{2}\rho A v_{in}^2}. \tag{2.11}$$

The dimensionless thrust coefficient is often also called the loading coefficient.

Unfortunately a propeller never operates at the ideal efficiency. Apart from the ideal axial losses, additional axial losses exist due to the fact that a propeller experiences a non-uniform loading and has a finite number of blades. The actual efficiency of a propeller in open water, η_0, is defined as the useful power output divided by the total delivered power $P_{delivered}$, which is given by

$$\eta_0 = \frac{P_{useful}}{P_{delivered}} = \frac{Tv_{in}}{2\pi n Q}, \tag{2.12}$$

where n is the rotation rate and Q is the torque of the propeller [4]. As explained before, some axial energy is lost due to the non-uniform loading and the finite number of blades. Another main loss component is the rotational losses. The flow is rotated by the propeller. Velocity in the tangential and radius direction do not contribute to the thrust in the axial direction and as a consequence these components are losses. A third loss component are the viscous losses, since the flow is not inviscid. Because of this an alternative way to determine the efficiency of the propeller is by determining the losses of the propeller, which is given by

$$\eta_p = 1 - \frac{Losses}{P_{delivered}} = 1 - \frac{AXL}{P_{delivered}} - \frac{ROTL}{P_{delivered}} - \frac{VISL}{P_{delivered}}, \tag{2.13}$$

where AXL refers to the total axial losses, $ROTL$ are the rotational losses and $VISL$ the viscous losses induced by the propeller [30] [31].

2.1.3 Open water performance

It is shown in equation (2.12) that the advance speed of the ship and the rotations per minute (RPM) of the propeller influence the efficiency of the propeller. A propeller is designed for a specific RPM and ship speed, the design point. The propeller does not always operate under these conditions. The operating condition influences the performance of the propeller, therefore we want to calculate the performance at multiple operating conditions. Common measures of the propeller performance are the open water characteristics. These are calculated by determining the thrust and torque of a propeller in open water with a uniform inflow at different advance speeds [4]. This can be done experimentally on model-scale propellers in test basins. Numerical methods can also be used to predict the performance of a propeller. When CFD is used, the thrust and torque are found by integrating the pressure and shear forces over the propeller blades.

The open water characteristics compare the thrust, torque and efficiency at different advance coefficients, J. The dimensionless thrust, K_t, the dimensionless torque, K_q, and the efficiency, η_0, are plotted against the advance coefficient. These charts are called the open water characteristics. A typical example is presented in Figure 2.2, where

$$K_t = \frac{T}{\rho n^2 D^4}, \tag{2.14}$$
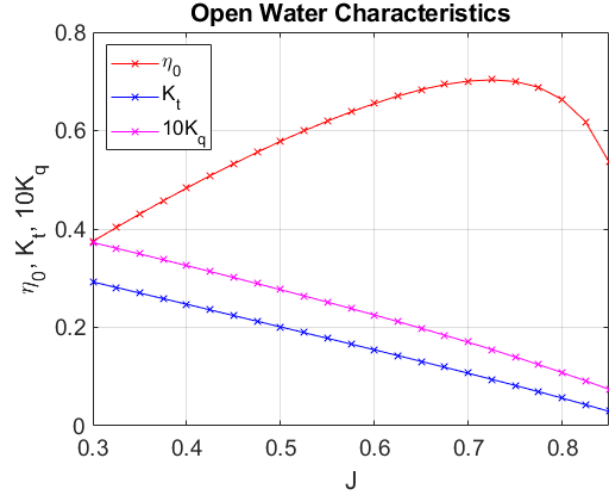
Figure 2.2: Typical open water characteristics graph where K_t is the dimensionless thrust, K_q the dimensionless torque, η_0 the efficiency and J the advance coefficient

$$K_Q = \frac{Q}{\rho n^2 D^5} \tag{2.15}$$

and

$$J = \frac{v_{in}}{nD}, \tag{2.16}$$

where D is the diameter of the propeller.

The thrust and torque are represented in a non-dimensional form because these graphs are general for a specific geometric configuration. The principle of dimensional similarity can therefore be applied to geometrically similar propellers [4].

As explained before, the propeller is optimized for one design point. This will not be the only operating condition. The operating regimes of a propeller normally lies in between the K_t value of 0.2 and the $10K_q$ value of 0.2. For the propeller in Figure 2.2 this would mean that the propellers operating regime is $0.50 < J < 0.65$.

2.2 Conservation equations

In this study the control volume method will be used to measure the energy losses of a propeller in CFD simulations. In this method the three main principles of conservation are applied. These fundamental laws are the conservation of mass, conservation of linear momentum and conservation of energy, also referred to as the continuity equation, the second law of Newton and the first law of thermodynamics, respectively. These equations will be derived in this section.

2.2.1 Conservation of mass

Consider an arbitrary control volume V with control surface S in a fluid as shown in Figure 2.3, where $\mathbf{n}$ = (n_x, n_y, n_z) is the normal vector acting on the control surface and $\mathbf{u} = (u, v, w)$ is the velocity vector. dV represents an infinitesimal small fluid element, with constant fluid properties and surface dS. In this study it is assumed that the control volume has fixed boundaries.

The continuity equation represents the physical principle that mass is conserved. The change of mass over time in the control volume is equal to the net flow through the boundaries. The mass of the infinitesimal fluid element is given by ρdV and the net flow through the boundaries by $\rho(\mathbf{u} \cdot \mathbf{n})dS$. Integrating these properties over the control volume gives

$$\frac{\partial}{\partial t} \int_V \rho dV + \int_S \rho \mathbf{u} \cdot \mathbf{n} dS = 0, \tag{2.17}$$

which is know as the conservation of mass in integral form [32]. This equation can be rewritten into a differential form, with the help of the divergence theorem. The divergence theorem is given by
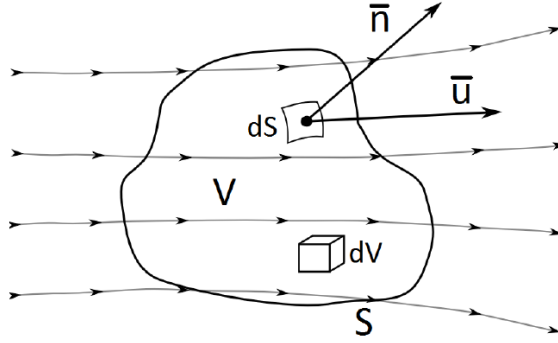
Figure 2.3: An arbitrary control volume V with control surface S, where $\mathbf{n} = (n_x, n_y, n_z)$ is the normal vector acting on the control surface and $\mathbf{u} = (u, v, w)$ is the velocity vector. dV represents an infinitesimal small fluid element with surface dS. [33]

$$\int_V (\nabla \cdot \mathbf{G}) dV = \int_S \mathbf{G} \cdot \mathbf{n} dS \tag{2.18}$$

where $\mathbf{G}$ is an arbitrary continuously differentiable vector field and $\nabla = (\frac{\partial}{\partial x}, \frac{\partial}{\partial y}, \frac{\partial}{\partial Z})$ is the nabla operator [34]. The resulting equations of the conservation of mass therefore becomes

$$\int_V (\frac{\partial \rho}{\partial t} + \nabla \cdot \rho \mathbf{u}) dV = 0. \tag{2.19}$$

The time derivative can be placed inside the integral since the boundaries of the control volume are fixed and therefore its volume does not change. Since the control volume is arbitrarily chosen, the integrand should be zero and the continuity equation in differential form becomes

$$\frac{\partial \rho}{\partial t} + \nabla \cdot \rho \mathbf{u} = 0. \tag{2.20}$$

For an incompressible fluid, where ρ is constant, this equation simplifies to

$$\nabla \cdot \mathbf{u} = 0, \tag{2.21}$$

which is better known as the continuity equation.

2.2.2 Conservation of linear momentum

The conservation of linear momentum is governed by the second law of Newton,

$$\mathbf{F} = \frac{\partial m \mathbf{u}}{\partial t}, \tag{2.22}$$

where $\mathbf{F} = (F_x, F_y, F_z)$ is the force and m is the mass. An expression for the right hand side of equation (2.22) can be derived in an analogous way as for the conservation of mass. This term is the sum of the time rate of change of momentum inside the control volume and the flow of momentum through the control boundaries. An expression for the momentum equation in the x-direction is given by

$$F_x = \frac{\partial}{\partial t} \int_V \rho u dV + \int_S \rho u (\mathbf{u} \cdot \mathbf{n}) dS, \tag{2.23}$$

where the left hand side of equation (2.23) represents the sum of all forces in the x-direction [32]. This term can be split up into body forces that act on the body as a whole and surface forces that act on the surface of the fluid element. The body forces per unit mass acting on a infinitesimal small fluid element are represented by $\mathbf{f} = (f_x, f_y, f_z)$. One example of a body force is gravity. The surface forces on the fluid element are the pressure and the viscous stresses. The forces acting on an infinitesimal small fluid element are visualized in Figure 2.4, where σ is the stress tensor, including the shear stresses and normal stresses. σ can be defined as

$$\sigma = -pI + \tau, \tag{2.24}$$
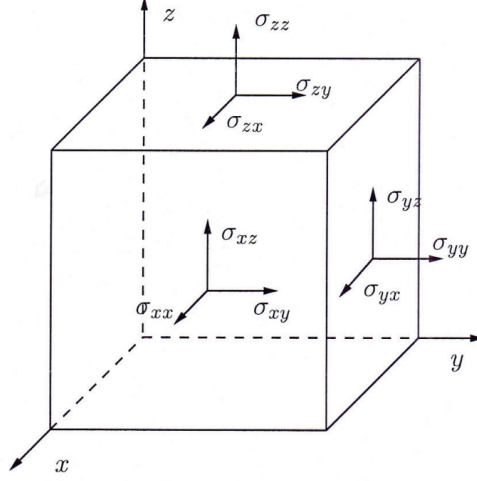
Figure 2.4: The forces acting on an infinitesimal small fluid element, where σ is the stress tensor [35]

where p is the pressure, I the identity matrix and τ the viscous stresses.

An expression for the forces in the momentum equation in the x-direction is

$$F_x = \int_V (-\frac{\partial p}{\partial x} + \frac{\partial \tau_{xx}}{\partial x} + \frac{\partial \tau_{yx}}{\partial y} + \frac{\partial \tau_{zx}}{\partial z} + \rho f_x) \tag{2.25}$$

where τ_{ij} is the viscous stress in the plane perpendicular to the i direction in the j direction [37]. The derivation of the differential form is similar to the derivation of the continuity equation. After substituting equation (2.25), equation (2.23) can be rewritten, using the divergence theorem, into

$$\frac{\partial \rho u}{\partial t} + \nabla \cdot \rho u \mathbf{u} = -\frac{\partial p}{\partial x} + \frac{\partial \tau_{xx}}{\partial x} + \frac{\partial \tau_{yx}}{\partial y} + \frac{\partial \tau_{zx}}{\partial z} + \rho f_x. \tag{2.26}$$

The momentum equation can be derived in a similar way for the y and z direction. The momentum equations in all directions can be expressed in the more convenient vector notation. The momentum equation is given by

$$\frac{\partial (\rho \mathbf{u})}{\partial t} + \nabla \cdot (\rho \mathbf{u}\mathbf{u}) = -\nabla p + \nabla \cdot \tau + \rho \mathbf{f}, \tag{2.27}$$

where τ is the stress tensor. The left hand side of this equation can be rewritten using the formula of divergence for a second order tensor, which is

$$\nabla \cdot (\mathbf{ab}) = (\nabla \cdot \mathbf{a})\mathbf{b} + \mathbf{a} \cdot \nabla \mathbf{b}, \tag{2.28}$$

where $\mathbf{a}$ and $\mathbf{b}$ are arbitrary vectors [34]. The left hand side of equation (2.27) therefore can be rewritten to

$$\mathbf{u}\frac{\partial \rho}{\partial t} + \rho \frac{\partial \mathbf{u}}{\partial t} + \mathbf{u}\mathbf{u} \cdot \nabla \rho + \rho \mathbf{u} \cdot \nabla \mathbf{u} + \rho \mathbf{u} \nabla \cdot \mathbf{u}. \tag{2.29}$$

This equation again can be rearranged and rewritten into

$$\mathbf{u}(\frac{\partial \rho}{\partial t} + \mathbf{u} \cdot \nabla \rho + \rho \nabla \cdot \mathbf{u}) + \rho(\frac{\partial \mathbf{u}}{\partial t} + \mathbf{u} \cdot \nabla \mathbf{u}) = \mathbf{u}(\frac{\partial \rho}{\partial t} + \nabla \cdot (\rho \mathbf{u})) + \rho(\frac{\partial \mathbf{u}}{\partial t} + \mathbf{u} \cdot \nabla \mathbf{u}). \tag{2.30}$$

The leftmost expression enclosed in parentheses on the right hand side of the equal sign can be recognized as the mass continuity equation. As derived in equation (2.20), this is equal to zero. For this reason equation (2.27) can be rewritten into

$$\rho(\frac{\partial \mathbf{u}}{\partial t} + \mathbf{u} \cdot \nabla \mathbf{u}) = -\nabla p + \nabla \cdot \tau + \rho \mathbf{f}. \tag{2.31}$$

For a Newtonian fluid the stress tensor becomes

$$\tau_{ij} = \mu(\frac{\partial u_i}{\partial x_j} + \frac{\partial u_j}{\partial x_i}), \tag{2.32}$$

where μ is the dynamic viscosity of the fluid [36]. Using this relation, equation (2.31) can be rewritten to the well known Navier-Stokes equations,

$$\frac{\partial \mathbf{u}}{\partial t} + \mathbf{u} \cdot \nabla \mathbf{u} = -\frac{1}{\rho}\nabla p + \nu \nabla^2 \mathbf{u} + \mathbf{f}. \tag{2.33}$$

2.2.3   Conservation of energy

The fundamental conservation law of energy is given by the first law of thermodynamics which states that the change of energy of a system is equal to the sum of heat added to the system and work done on the system. The first law of thermodynamics is given by

$$dE = d\dot{Q} + dW, \tag{2.34}$$

where E represents the total energy of the system, including internal energy, kinetic energy and potential energy, $\dot{Q}$ denotes the heat added to the system and W the work performed on the system [38].

By using the three fundamental principles of physics, conservation of mass, Newtons second law and the first law of thermodynamics, the energy equation can be written as

$$\underbrace{\frac{\partial}{\partial t} \int_V \rho E dV}_{1} + \underbrace{\int_S \rho E(\mathbf{u} \cdot \mathbf{n})dS}_{2} = \underbrace{\int_V \rho(\mathbf{u} \cdot \mathbf{f})dV}_{3} - \underbrace{\int_S p(\mathbf{u} \cdot \mathbf{n})dS}_{4} + \underbrace{\int_S (\tau\mathbf{u}) \cdot \mathbf{n}dS}_{5}$$

$$+ \underbrace{\int_V \dot{Q}dV dV}_{6} - \underbrace{\int_S (\mathbf{q} \cdot \mathbf{n})dS)}_{7}, \tag{2.35}$$

where $\mathbf{q}$ is the heat flux [27]. The first term represents the change in energy density in time within the control volume. The second term is the amount of energy that is transported through the control volume per unit time. These two terms represent the change in energy, which must be balanced by the production and net flux of heat in volume V and the work performed on the volume V, according to the first law of thermodynamics. The third term expresses the work performed by the body forced per unit time. The fourth term represents the amount of work performed by pressure forces acting on the surface S per unit time. The fifth term is the work per unit time performed by surface frictional forces. The sixth term is the volumetric heating by external forces, such as absorption and emission of heat by radiation. Finally, the last term represents the heat transfer across the control surface into the volume by thermal heat conduction.

2.2.4   Evaluation of the conservation of energy for a propeller

In order to apply the conservation of energy on a propeller, we consider a control volume surrounding a propeller, as presented in Figure 2.5. The different components of equation (2.35), such as heat, axial energy, rotational losses and viscous losses, will be evaluated in the next sections.
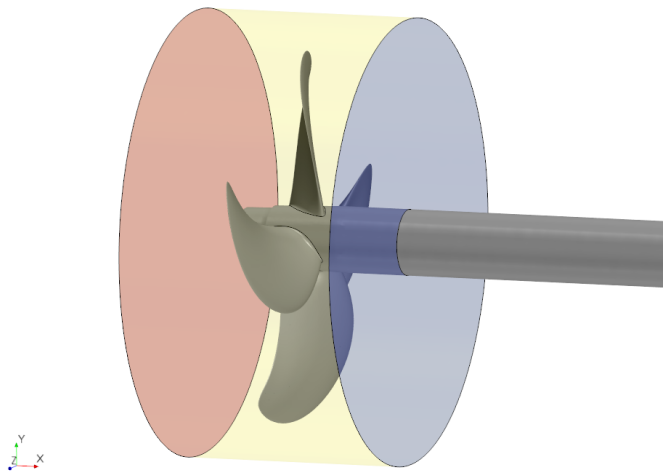
Figure 2.5: A control volume surrounding a propeller, where the flow is going from right to left. The blue surface is the inflow interface, the red surface is the outflow interface and the yellow surface is the cylindrical surrounding surface.

Heat

The sixth and seventh term in equation (2.35) represent the volumetric heating and thermal heat conduction. These two terms both represent heat transfer in the system. Two different claims about the heat in open water simulations have been made. The first claim is that heat transfer does not play a significant role [27]. Therefore terms 6 and 7 in equation (2.35) can be disregarded.

The second claim is that the viscous losses can be evaluated as internal and turbulent kinetic energy. The reasoning behind this is that in a viscous flow kinetic energy of the mean flow is converted into internal energy as heat through the dissipation of turbulent velocity fluctuations and direct viscous dissipation from the mean flow to internal energy [39]. Because of this the internal energy flux should be measurable using heat.

The internal energy is defined as

$$\hat{u} = c_p T, \tag{2.36}$$

where c_p is the specific heat capacity and T the temperature [39]. The increase of temperature due to dissipation is very small. In order to prove that the temperature increase is very small, consider a propeller with a diameter of 7.6 meters based on a propeller designed by Wärtsilä. This propeller has an actuator disk area A of 45.4 m^2, an advance speed of 7.4 m/s, an RPM of 90.9 and a power input of 16000 kW. In order to be able to measure a temperature difference in the simulation, the heated disk needs to be as thin as one grid cell. The size of one grid cell is assumed to be 0.0078125·D, similar to grid cells used in the simulations in this study. Therefore we consider an small disk with a volume of approximately 2700 liter. This volume is transported with a speed of 7.4 m/s by the propeller. The equation for calculating the required energy for a certain water heating process is

$$Q = m c_p \Delta T, \tag{2.37}$$

where Q is the required amount of energy for the process, m the mass of the liquid, c_p the specific heat which is 4.186 J/g°C for water and ΔT the temperature difference [40]. For this specific case we consider an increase in temperature of 1°C for the small disk of 2700 kg. In order to heat this volume by one degree 11300 kJ of energy is needed. The time needed for this process can be calculated by using

$$t = Q/P_{input}, \tag{2.38}$$

where t is the time and P_{input} is the power input. Most of the power input will be used to rotate the propeller. Consequently, a maximum of 10% of the total input is assumed to be lost due to dissipation and converted into heat. The power input used in this calculations is therefore 1600 kW. Using these values, the time it takes to heat the disk by one degree is approximately 7 seconds. The disk of water is advected by the propeller during this process. The disk is transported approximately 52 meters in 7 seconds. This is 6.8 times the diameter of the propeller, which will be far outside of the control volume. Because of this, it can be concluded that the temperature difference between the inflow and outflow of the control volume will be very small, and almost not measurable in CFD simulations. Therefore it is concluded that heat does not play a significant role and that using the temperature increase to calculate the viscous losses is almost impossible.

Energy equation for a propeller in open water

From the previous section we can conclude that heat does not play a significant role. The third term in equation (2.35) can also be omitted. The reason for this is that there are no body forces present in the simulations and gravity is not taken into account, since it does not perform net work on the propeller [27].

Since gravity is not modelled in the simulation and heat is not taken into account, the total energy equals the kinetic energy. The flow velocity components are written in the cylindrical coordinate system of the propeller reference system. The expression for the total energy therefore is

$$E = \frac{1}{2}\rho||\mathbf{u}(r, \theta, x)||^2, \tag{2.39}$$

where r represents the radial component, θ the tangential component and x the axial component. It is convenient to use the cylindrical coordinate system since it makes it easier to distinguish the axial energy component and the rotational energy component, which include the tangential and radial components. In order to further simplify equation (2.35), the work performed by the propeller, which is performed by both pressure and frictional forces, is combined into one term, $W_{propeller}$, which can be determined by

$$W_{propeller} = 2\pi n Q, \tag{2.40}$$

which also can be recognized as $P_{delivered}$ [27]. The work performed by frictional forces on the cylinder surface can be neglected, as it is many orders smaller than the other components. This leaves only the pressure term and the viscous dissipation on the right hand side of equation (2.35). The viscous dissipation term can be separated in two components. The first component is the molecular viscosity. The second component is the turbulent dissipation. This is viscous dissipation of kinetic energy that needs to be included since the turbulence models that are used in the simulations are eddy-viscosity models. More on turbulence modelling and eddy-viscosity models will be explained in Chapter 3. Combining all this simplifies equation (2.35) for a propeller in open water to

$$\underbrace{\frac{\partial}{\partial t} \int_V \frac{1}{2}\rho||\mathbf{u}||^2 dV}_{1} + \underbrace{\int_S \frac{1}{2}\rho||\mathbf{u}||^2(\mathbf{u} \cdot \mathbf{n})dS}_{2} = \underbrace{-\int_S p(\mathbf{u} \cdot \mathbf{n})dS}_{3}$$

$$+ \underbrace{\int_V 2(\mu + \mu_t)||\frac{1}{2}((\nabla\mathbf{u}) + (\nabla\mathbf{u})^T)||^2 dV}_{4} + W_{propeller}, \tag{2.41}$$

where μ_t is the eddy-viscosity [27].

In this study both quasi-steady and transient simulations will be performed, these will be explained further in Chapter 3. In quasi-steady simulations term 1 is equal to zero, since there is no time step. In transient simulations time will play a role. Every simulation will be performed over an integer number of rotations. Since no body forces are present in the simulations, the time derivative of an integer number of rotations should be zero, otherwise the propeller would be drifting. Due to this, the equation can be further simplified to

$$\underbrace{\int_S \frac{1}{2}\rho||\mathbf{u}||^2(\mathbf{u} \cdot \mathbf{n})dS}_{1} = \underbrace{-\int_S p(\mathbf{u} \cdot \mathbf{n})dS}_{2} + \underbrace{\int_V 2(\mu + \mu_t)||\frac{1}{2}((\nabla\mathbf{u}) + (\nabla\mathbf{u})^T)||^2 dV}_{3} + W_{delivered}. \tag{2.42}$$

In this equation, term one represents the kinetic energy. This can be separated in rotational kinetic energy and axial kinetic energy. The second term represents the work done by pressure. The third term represents the viscous losses.

Axial energy

The axial energy is the most important energy for a propeller. The axial energy generates thrust which makes the ship move forward. Unfortunately, not all axial energy can be converted into thrust. Some energy is lost as axial losses. The axial losses can be divided into two parts, the ideal axial losses and the additional axial losses [27]. Accordingly, the total axial losses, AXL, can be determined by

$$AXL = IAXL + AAXL. \tag{2.43}$$

The axial fluxes can be separated in ideal axial losses, $IAXL$, and additional axial losses, $AAXL$, using the actuator disk theory. The ideal axial losses can be defined as

$$IAXL = Tv_{in}(\frac{1}{\eta_i} - 1), \tag{2.44}$$

where η_i is the ideal efficiency as derived in the momentum theory of Rankine [27]. The additional axial losses due to the non-uniform loading and finite number of blades can be obtained by subtracting the total axial fluxes, TAF, with the useful power and the ideal axial losses. This results in

$$AAXL = TAF - P_{useful} - IAXL. \tag{2.45}$$

The total axial energy is not only the result of the axial kinetic energy. As described in the actuator disk model, low and high pressure regions are generated ahead and behind the propeller, which accelerate the flow. This is a continuous energy conversion where work by pressure is converted into axial energy [41]. Therefore, the work performed by pressure on the cylindrical control surface, P, and the axial energy flux, E_x, from term 1 and 2 are combined in one total axial fluxes term, TAF, which is given by

$$TAF = E_x + P \tag{2.46}$$

with

$$E_x = \int_S \frac{1}{2}\rho u_x^2(\mathbf{u} \cdot \mathbf{n})dS \tag{2.47}$$

and

$$P = \int_S p(\mathbf{u} \cdot \mathbf{n})dS. \tag{2.48}$$

Rotational losses

A lot of energy is lost due to the rotation of the water by the propeller. There are two phenomena that are the mean cause of rotational losses, the tip vortices and the hub vortex. These vortices are created by the pressure difference between the face and back of the blades [4]. Particles tend to travel from high to low pressure areas. This is possible at the trailing edge of the propeller, resulting in a circular motion around the edge. Because of this, vortex lines are generated at the blade edges. These vortex lines roll up at the tip and root of the blade, generating tip and root blade vortices. The root blade vortices join into a single vortex at the hub, called the hub vortex.

The rotational losses, $ROTL$, can easily be determined by taking the rotational energy component of the first term of equation (2.42) [27]. This can be expressed as

$$ROTL = \int_S \frac{1}{2}\rho(u_\theta^2 + u_r^2)(\mathbf{u} \cdot \mathbf{n})dS. \tag{2.49}$$

Both the tangential and radial velocity components are considered to belong to the rotational losses, because they do not actively contribute to the thrust production.

Viscous losses

Viscous losses originate from the frictional and, to a small extent, from the form drag of the blade sections [27]. The third term in equation (2.42) represents the viscous dissipation due to molecular dissipation and turbulent eddy-viscosity dissipation.

The norm of the matrix that can be seen in term 3 in equation (2.42) is the so-called Frobenius norm given by

$$||A||_F = \sqrt{\sum_{i=1}^{m}\sum_{j=1}^{n}|a_{ij}|^2}. \tag{2.50}$$

The molecular viscous losses, $MOVL$, can be determined by only taking the molecular viscosity part of the viscous dissipation term, resulting in

$$MOVL = \int_V 2\mu||\frac{1}{2}((\nabla\mathbf{u}) + (\nabla\mathbf{u})^T)||^2 dV. \tag{2.51}$$

Using the Frobenius norm from equation (2.50) the molecular viscous losses can be rewritten into

$$MOVL = \int_V 2\mu\left((\frac{\partial u}{\partial x})^2 + (\frac{\partial v}{\partial y})^2 + (\frac{\partial w}{\partial z})^2 + \frac{1}{2}(\frac{\partial v}{\partial x} + \frac{\partial u}{\partial y})^2 + \frac{1}{2}(\frac{\partial w}{\partial y} + \frac{\partial v}{\partial z})^2 + \frac{1}{2}(\frac{\partial u}{\partial z} + \frac{\partial w}{\partial x})^2\right) dV. \tag{2.52}$$

Likewise, the turbulent dissipation can be evaluated by taking the eddy viscosity part,

$$TUVL = \int_V 2\mu_t||\frac{1}{2}((\nabla\mathbf{u}) + (\nabla\mathbf{u})^T)||^2 dV. \tag{2.53}$$

This can be rewritten, using the Frobenius norm, into

$$TUVL = \int_V 2\mu_t\left((\frac{\partial u}{\partial x})^2 + (\frac{\partial v}{\partial y})^2 + (\frac{\partial w}{\partial z})^2 + \frac{1}{2}(\frac{\partial v}{\partial x} + \frac{\partial u}{\partial y})^2 + \frac{1}{2}(\frac{\partial w}{\partial y} + \frac{\partial v}{\partial z})^2 + \frac{1}{2}(\frac{\partial u}{\partial z} + \frac{\partial w}{\partial x})^2\right) dV. \tag{2.54}$$

Both the molecular viscous losses and the turbulent dissipation are calculated using gradients of the velocity. These gradients often have high values close to the walls. Not all turbulence models can correctly calculate these gradients. When the gradients are not calculated correctly, a different method to calculate the viscous losses can be used, using the turbulent dissipation, ϵ. The equation to calculate these losses is expressed as

$$VISL = \int_V \rho\epsilon dV. \tag{2.55}$$

The turbulent dissipation is a quantity that is modelled in the simulations. $VISL$ unfortunately only represents the turbulent dissipation of the viscous losses, which is the dissipation due to fluctuations in the flow. The dissipation of the mean flow is not calculated. Because of this, calculating the molecular viscous losses and turbulent viscous losses is preferred. The $VISL$ will only be used when we are not able to calculate the $MOVL$ and $TUVL$ correctly.

3 | Numerical methods

Understanding the energy losses is important to be able to save energy in maritime industries. The first studies of energy losses were based on potential flows, which does not take into account the viscous effects. More recently a new method, which does take viscous effects into account, was presented, the control volume method. In the previous chapter the relevant theory regarding the control volume method was presented. Now that the theory is explained, the numerical methods necessary to be able to use the control volume method will be presented.

In Section 3.1 the different aspects of turbulence modelling will be explained. First a brief introduction into turbulence will be given. After this three different computational methods will be reviewed. One of these methods is the RANS method, which is used in this study. The important aspects of RANS modelling, such as the closure problem, different turbulence models and wall treatments will also be explained in this section.

In Section 3.2 the computational domain used in this study will be introduced. The meshing will be explained in Section 3.3. Additionally, different methods of modelling the rotation of the propeller will be explained in 3.4.

3.1 Turbulence modelling

3.1.1 Turbulence

The fluid flow can be characterized as a laminar or turbulent flow. A turbulent flow is a type of fluid flow in which the fluid undergoes irregular fluctuations, or mixing. This is in contrast with laminar flow, in which the fluid moves in smooth paths or layers. The transition from a laminar to a turbulent flow depends on the Reynolds number, a dimensionless quantity that gives a relation between the inertial and viscous forces, defined as

$$\text{Re} = \frac{U_\infty L}{\nu},\tag{3.1}$$

where U_∞ is the characteristic velocity, L the characteristic length scale and ν the kinematic viscosity. For a high Reynolds number, where the inertial forces dominate, the flow becomes turbulent. The viscous forces dampen the fluctuations for lower Reynolds numbers and therefore the flow stays smooth. Turbulent flows are highly unsteady, always 3-dimensional and a large amount of vorticity is present in these flows.

In a turbulent flow the local speed and pressure change unpredictably. An average flow, however, is maintained. A turbulent flow property is visualized in Figure 3.1, where the flow property, velocity in this example, is split into a mean, $\overline{\mathbf{u}}$, and a fluctuating component, $\mathbf{u'}$ [37]. This is called the Reynolds decomposition. This Reynolds decomposition is used to derive the Reynolds averaged equations, which are used in the CFD method RANS modelling.

3.1.2 Computational methods

There are basically three methods in turbulence models, Direct Numerical Simulations (DNS), Large Eddy Simulations (LES) and Reynolds-Averaged Navier-Stokes (RANS) modelling. Various hybrid models are derived from these three methods. A direct numerical simulation is a simulation in which the Navier-Stokes equations are numerically solved without any turbulence model. This means that the whole range of spatial and temporal scales of the turbulence must be resolved, from the smallest dissipative scales up to the integral scales. In theory this is possible. The computational costs for this method are very high. The number of grid points, N, in the simulations should at least be

$$N \sim \text{Re}^{\frac{9}{4}},\tag{3.2}$$
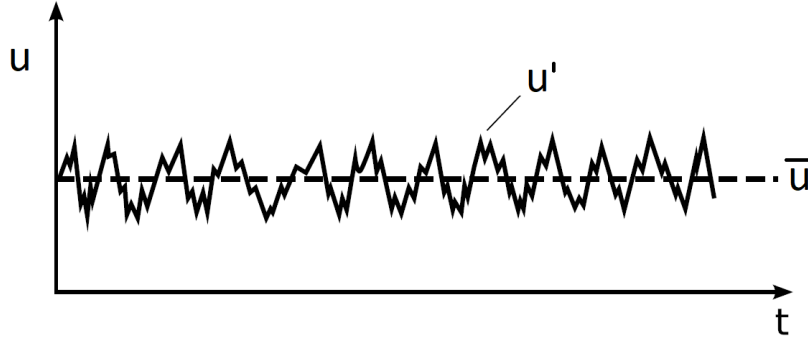
Figure 3.1: An example of a turbulent flow property, where the flow property velocity, **u**, is split into a mean, $\overline{\mathbf{u}}$, and a fluctuating component, **u'** [33]

which is a large amount of grid points for large Reynolds numbers [42]. This method is often not used for commercial applications, since a fast result is required.

LES is another mathematical method that is often used in computational fluid dynamics. The principal idea behind LES is to reduce the computational costs by ignoring the small length scales, which are the most computationally expensive, via a low-pass filtering of the Navier-Stokes equations. These small scales are not irrelevant, and therefore its effect on the flow field are modelled. LES still is very computationally and time expensive, as a result this method is not often used in commercial applications.

The method that is most used for commercial applications, and also in this study, is Reynolds-Averaged Navier-Stokes modelling, which resolves the Reynolds-Averaged Navier-Stokes equations. The derivation of these equations can be found in Appendix A. The Reynolds-Averaged Navier-Stokes equations, in Cartesian tensor notation, are given by

$$\frac{\partial \overline{u_i}}{\partial t} + \frac{\partial \overline{u_i}\,\overline{u_j}}{\partial x_j} = -\frac{1}{\rho}\frac{\partial \overline{p}}{\partial x_i} + \nu \frac{\partial^2 \overline{u_i}}{\partial x_j \partial x_j} + \overline{f_i} - \frac{\partial \overline{u_i' u_j'}}{\partial x_j}. \tag{3.3}$$

A new term is introduced in the RANS equations, the Reynolds stresses. The term at the far right in the equation represents the Reynolds stresses. Herein lies the fundamental problem of turbulence modelling. In order to compute all mean-flow properties of the turbulent flow, we need a model for computing the Reynolds stresses [43].

3.1.3 The closure problem

In the RANS equations the Reynolds stresses are derived. As a consequence, there are 10 unknowns within only 4 equations. Due to this the system is not closed. In quest of additional equations, the moments of the Navier-Stokes equations can be calculated. Using this procedure, differential equations for the Reynolds stress tensor can be derived. This results in six new equations, one for each independent component of the Reynolds stress tensor. 22 unknowns are also derived in these new equations. Because of the non-linearity of the Navier-Stokes equations, when higher order moments are derived, more additional unknowns are also derived. This is known as the closure problem.

Many strategies to close the set of RANS equations exist. In this study, a simple Boussinesq closure is considered only. In this approach the Reynolds stresses are related to the mean time rate of strain of a fluid element, similar to the relations for a Newtonian fluid. An additional flow property is introduced, the eddy-viscosity μ_t. The Reynolds stresses are expressed as

$$-\rho \overline{u_i' u_j'} = \mu_t \left(\frac{\partial \overline{u_i}}{\partial x_j} + \frac{\partial \overline{u_j}}{\partial x_i}\right) - \frac{2}{3}\rho \delta_{ij} k, \tag{3.4}$$

where δ_{ij} is the Kronecker delta.

To determine the eddy-viscosity a number of models are developed. The models are named according to the number of extra transport equations that need to be solved, ranging from zero to two equation models. The choice of the turbulence model depends on the research goal. The two most used and best known turbulence models are the $k - \epsilon$ and $k - \omega$ models. A lot of variations of these models are available. In this study the Standard $k - \epsilon$ model and SST Menter $k - \omega$ model will be used. These models will be called the $k - \epsilon$ and $k - \omega$ model from here forward.

A different method that could be used to close the set of RANS equations is the Reynolds stress model (RSM). In this approach new transport equations for each of the six components of the Reynolds stresses

are introduced. To close the system of equations empirical parameters are used. RSM theoretically gives a more accurate modelling of the Reynolds stresses, but the computational costs are greatly increased [37]. Because of this, the two-equation model approach is favoured in engineering applications and also in this study.

3.1.4 The $k - \epsilon$ and $k - \omega$ model

The $k - \epsilon$ and $k - \omega$ model both have two additional transport equations that need to be solved, one for the specific turbulent kinetic energy, k, and one for the specific turbulent dissipation, ϵ, or the specific turbulent dissipation rate, ω. The $k - \epsilon$ model is known to behave well far away from boundaries, but it is less accurate close to the boundaries [46]. The $k - \omega$ model resolves the near-wall interaction more accurately than the $k - \epsilon$ model. This model is popular for turbomachinery simulations and for simulations where strong vortices are present, such as those originating from wing tips. A disadvantages is that the computational costs for the $k - \omega$ model are higher in comparison with the $k - \epsilon$ model because more grid cells are necessary near the boundaries to fully resolve the boundary layer. The $k - \omega$ model is also quite non-linear, so its convergence is slower and sensitive to initial conditions. Different wall treatments are applied in combination with these models.

3.1.5 Wall treatment

A fully developed turbulent boundary layer can be divided into three different regions, the viscous sublayer, the buffer layer and the log-law region, which are shown in Figure 3.2. The boundary layer is divided in these three regions by the non-dimensional distance from the wall, which is defined as

$$y^+ = \frac{u_\tau y}{\nu}. \tag{3.5}$$

The shear velocity is defined as

$$u_\tau = \sqrt{\frac{\tau_w}{\rho}}, \tag{3.6}$$

where τ_w is the shear-stress at the wall [45]. The region where $y^+ < 5$ is the viscous sublayer, while the region where $y^+ > 30$ is called the log-law region. Everything in between is called the buffer layer.

It is important to remember that it is assume that the boundary layer is turbulent and fully developed. Therefore, it is important to consider if flow separation can occur in the simulations. There are variations of the $k - \omega$ model which are able to accurately predict wall bounded flow separation. When the nature of separation is very strong, the $k - \omega$ model will not be accurate. When this is the case using RSM is an option.

The software program used in this study, STAR-CCM+, provides three different wall treatments. These are the low y^+, high y^+ and all y^+ wall treatment. The names of these values already indicate an important factor of the wall treatment, the value of y^+. Unfortunately y^+ cannot be determined a priori, because of its dependence on the velocity gradient at the wall.

The low y^+ approach assumes that the boundary layer is completely resolved. This leads to more grid cells in the viscous dominated layer, the buffer zone and the logarithmic layer. Hence, a very fine mesh is needed and a y^+ value of 1 or lower is desired.
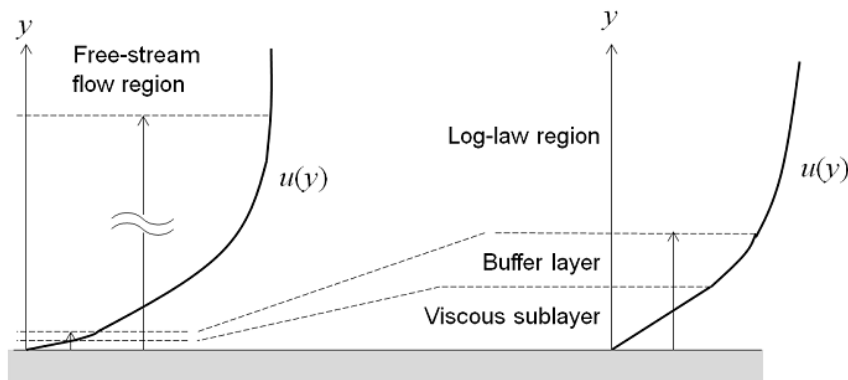
Figure 3.2: A fully developed turbulent boundary layer, divided in three regions by y^+, the non-dimensional distance from the wall [44]

In the high y^+ approach it is assumed that the first grid cell is in the logarithmic part of the boundary layer. In this approach a y^+ value of 30 or higher is desired. This wall treatment uses a wall function to solve the boundary layer. This wall function impose an explicit condition regarding velocity and turbulence in the boundary layer. Due to this, less cells are needed near the surface, leading to a less computationally expensive simulation.

The all y^+ approach is a hybrid between the high and low y^+ wall treatments. It chooses which treatment to use based on the y^+ in the simulation. Because of its ability to choose either the low or high y^+ wall treatment, this treatment is the most user friendly. Less knowledge about the boundary layer is required before starting the simulation.
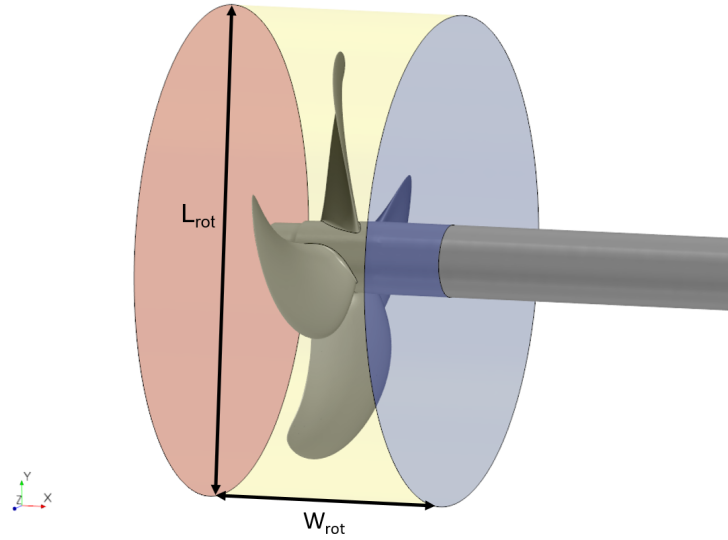
3.2 Computational domain

All the simulations in this study are performed with the same computational domain. A propeller with diameter D is placed inside a virtual test basin, which is the computational domain. This is a box with a length and width of 7 times the diameter of the propeller. This virtual test basin with a propeller is shown in Figure 3.3. The computational domain is chosen sufficiently large so that the boundaries do not affect the flow near the propeller. The surface of the domain upstream of the propeller is a velocity inlet boundary with a uniform inflow. The other surfaces are pressure outlets. The propeller is oriented with the shaft upstream of the propeller. This is called the reverse open water setup. In most open water simulations and experiments the shaft will be downstream of the propeller, to eliminate the effect of the shaft on the uniformity of the inflow. This however removes the hubcap effects, where the hub vortex is generated. The reverse setup is also a more realistic representation. Therefore it is chosen to use the reverse open water setup in this study.

Inside of the computational domain a cylinder surrounding the propeller is present. This is called the rotating region, and can also be used as the control volume in the analysis. In Figure 3.4 a zoomed in view of the rotating region is presented. The length of the rotating region, L_{rot}, is 1.2 times the diameter of the propeller and the width, W_{rot}, is 0.6 times the propeller diameter. These values are chosen based on a study by Schuiling and Terwisga [27]. They investigated two different propellers, one conventional diameter propeller (CDP) and one large diameter propeller (LDP). In their study they used the same dimensions of the control volume for the LDP. The contribution of the energy losses can dependent on the size of the control volume. As a consequence it is necessary to use identical control volumes when comparing the energy fluxes between different propellers [41]. This will be investigated further in Section 4.3. A comparison between the energy losses of the LDP and our propellers can be made using this control volume and rotating region.

It is generally known that changing the rotating region influences the results. These changes are typically small, though not always. When different control volume are used, the rotating region can be kept the same as in this setup. Sometimes, however, it would be more convenient to use a different rotating region. When a different rotating region is used, the results cannot be compared to simulations with a different rotating region without investigating the influence of the different rotating region.
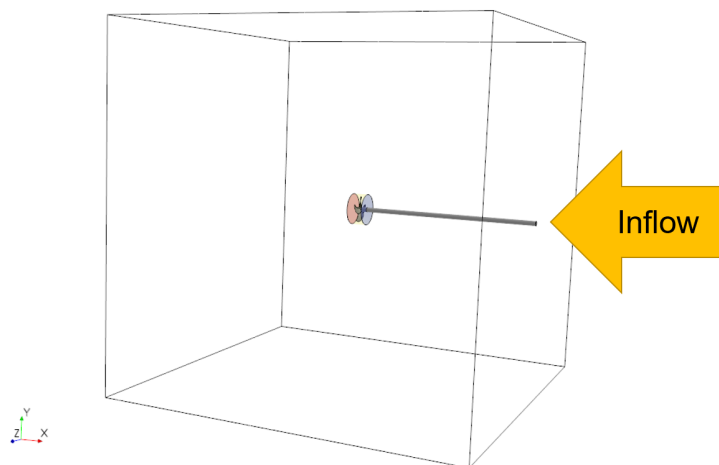
Figure 3.3: Propeller with diameter D inside the computational domain of 7·D, the cylinder surrounding the propeller is the rotating region or control volume with a radius of 0.6 ·D and a length of 1.2 ·D

Figure 3.4: The rotating region inside of the computational domain, where L_{rot} is the length of the rotating region and W_{rot} is the width of the rotating region, where the blue surface is the inflow interface, the red surface is the outflow interface and the yellow surface is the cylindrical interface

3.3 Mesh

The mesh is the representation of the computational domain in smaller discrete cells. The governing equations are solved in each of these cells. A finer mesh will result in more detailed results, but this also increases the computational costs. Therefore, the rotating region, which is the area of interest, has a finer mesh than the far field.

Two different wall treatments will be used in this study, the high y^+ and all y^+ wall treatment. Because of the different approaches of discretization of the boundary layers, different meshes are required. The mesh in the rotating region for both methods is presented in Figure 3.5. The all y^+ wall treatment requires either low or high y^+ value. In this study we will use the all y^+ to fully resolve the boundary layer, resulting in more and smaller prism layers. The transition from prism layers to the background mesh should be smooth. Big differences in sizes or not properly connected cells will result in instabilities in the simulation. Due to this, finer cells are present in the simulation with the all y^+ wall treatment.

(a)   (b)
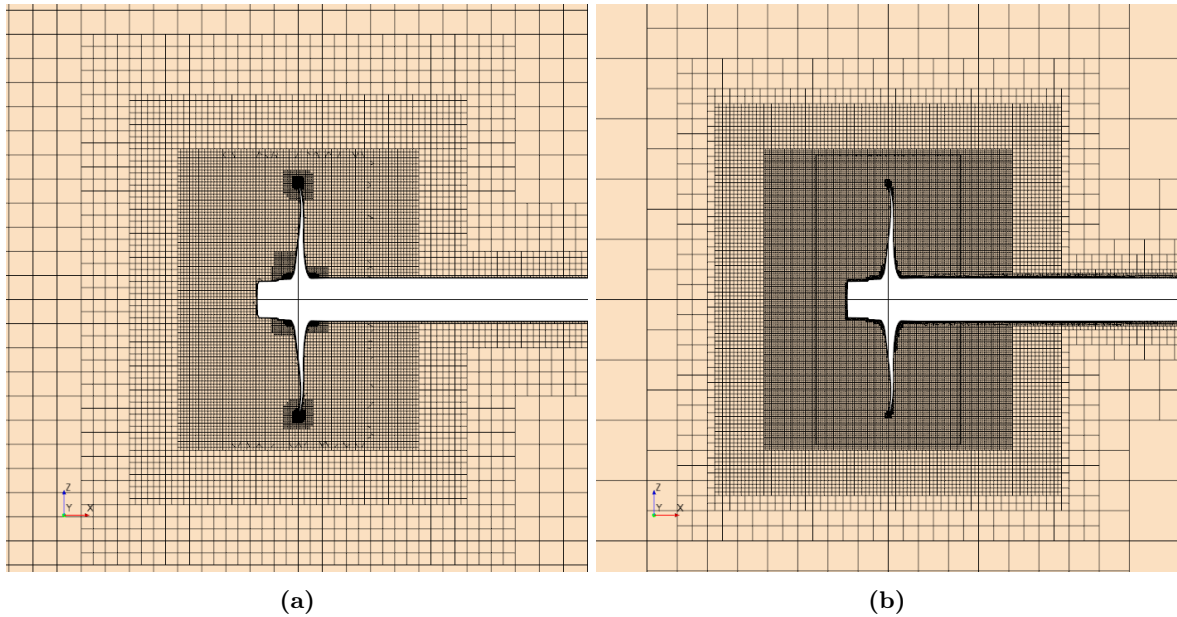
Figure 3.5: The mesh surrounding the rotating region for simulations with (a) the high y^+ wall treatment and (b) the all y^+ wall treatment

(a)   (b)
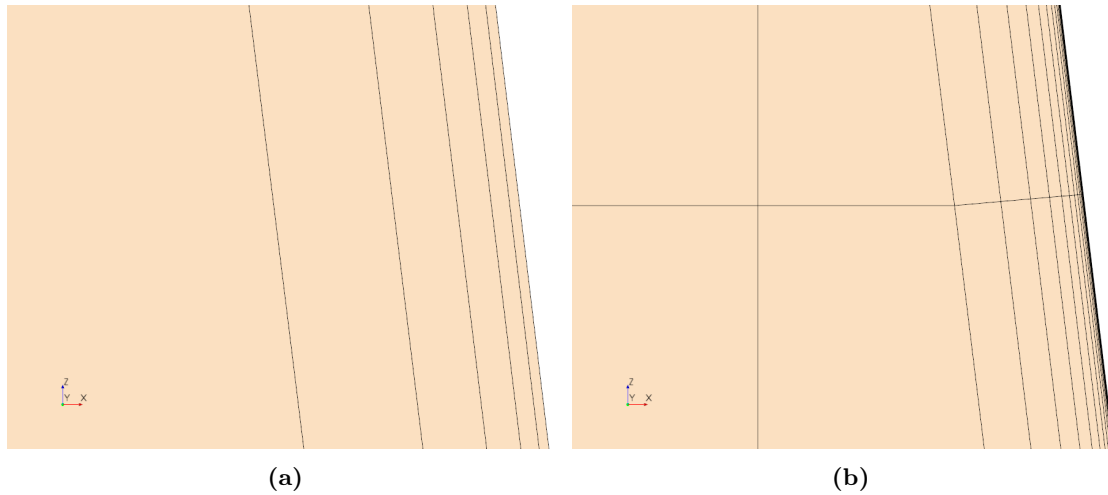
Figure 3.6: The prism layers on one of the blades for simulations with (a) the high y^+ wall treatment and (b) the all y^+ wall treatment

The desired y^+ value can be achieved by changing 3 parameters. These parameters are the stretching factor, the number of prism layers and the total thickness of the prism layer. Wärtsilä developed a method to calculate the values of these parameters. The prism layers on one of the blades for both wall treatments are presented in Figure 3.6. The white part on the right hand side in these figures represents the propeller blade. A clear difference can be noticed in these figures. Bigger and less prism layers are visible in the figure on the left hand side. The first cells are placed in the log-law region, since a wall function is used. The figure on the right hand side shows more and smaller prism layer. The first cells are placed in the viscous sublayer, and therefore the boundary layer will be fully resolved.

3.4   Modelling propeller rotation

As explained in Section 3.2 there is a cylinder, also called the rotating region, present in the computational domain. The motion of the propeller in simulated in this region. The rotation of the propeller will be simulated either with the Moving Reference Frame (MRF) model or the Sliding Mesh (SM) model. When the MRF model is used, the motion is induced by adding a steady rotational velocity in the rotating region. The propeller itself will not move. Therefore it is often referred to as the frozen rotor approach. This method can be used in quasi-steady and transient simulations. Since the propeller is not rotating, the MRF does not take into account the movement of the rotating region with respect to the rest of the computational domain. In order to account for this, new terms are added to the Navier-Stokes equations. The derivation of these terms can be found in Appendix B. The Navier-Stokes equations for a simulation with a rotating control volume are

$$\frac{\partial \mathbf{u}}{\partial t} + \mathbf{u} \cdot \nabla \mathbf{u} = -\frac{1}{\rho} \nabla p + \nu \nabla^2 \mathbf{u} + \mathbf{f} - 2(\mathbf{\Omega} \times \mathbf{u}) - \mathbf{\Omega} \times (\mathbf{\Omega} \times \mathbf{r}), \qquad (3.7)$$

where the two extra terms in this equation can be recognized as the Coriolis acceleration and the centrifugal acceleration, respectively [32]. When using the MRF method, one needs to keep in mind that these two terms contribute to the Navier-Stokes equations.

The second method is the Sliding Mesh (SM) methods. This method can be used in a transient simulation. In this case, the propeller is rotating and the mesh inside the rotating region will adjust at each time step. Since the rotation is taken into account, this gives a more accurate result than the MRF method. This method cannot be used in a steady simulation and is computationally more expensive.

In this study both the MRF and SM method will be used. The MRF is faster, since it can be used in a quasi-steady simulation, resulting in a simulation with less iterations. The MRF will mostly be used in combination with the $k - \epsilon$ model. When more accurate physical results are required the SM method is the better choice, in combination with the $k - \omega$ model.

3.5 Convergence

The results of our simulations are calculated iteratively and should converge to a solution. When the solution is converged is defined by the judgement of the user. In our quasi-steady simulations we use the thrust and torque values as a measure of convergence, along the usual residuals of the mass and momentum equations. We define that the solution is converged when both the thrust and torque have not changed for more than 1% over the last 500 iterations.

In the transient simulation we have chosen to start the simulation as a quasi-steady simulation for 1000 iterations, to generate an initial flow field before rotating the propeller. After this, we rotate the propeller using the SM method. The propeller will first be rotated with steps of 10 degrees for a total of 5 rotations. These 5 rotations are calculated in 900 iterations. The results of the simulations will be more accurate when the propeller is rotated with a smaller angle. The propeller will therefore be rotated with steps of 1 degree for 2 rotations after this. The results of the last rotation, which are the last 1800 iterations, will be averaged and used in the analysis of the transient simulation.

We have not defined when the transient simulation is converged in the simulation. To show that the solution does converge, the thrust calculated at each iteration is presented in Figure 4.3 for both the quasi-steady and transient simulation. The figure on the left hand side shows the thrust of the quasi-steady simulation, which is converged as defined. The figure on the right hand side shows the thrust of the transient simulation. This simulation shows a similar trend in the last rotation, denoted with the dotted line. As a result we can conclude that the solution is converged.
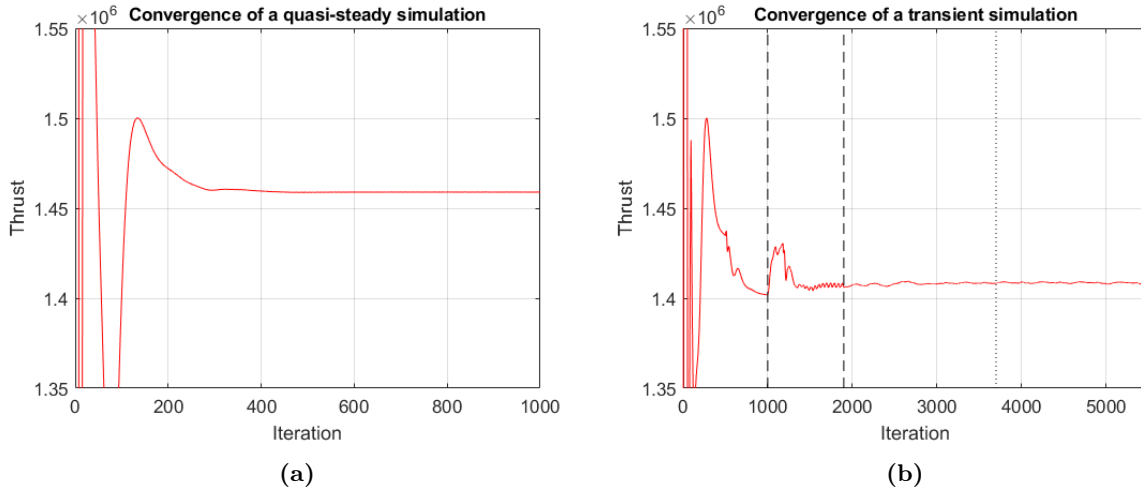
Figure 3.7: Thrust calculate at every iteration for (a) a quasi-steady simulation and (b) a transient simulate

4 | Analysis of the energy losses

In the previous chapters it was explained that different methods have been used to determine energy losses. The relevant theory regarding the control volume method was presented and the numerical methods necessary to be able to use the control volume method were explained.

In this chapter the results of the analysis of the energy losses using the control volume method will be presented. First the three different propellers that are analysed in this study will be introduced. The difference between these propellers will be investigated and the open water characteristics will be presented.

After this, the method by Schuiling & van Terwisga will be used to analyse the energy losses [27]. The losses calculated in our simulations will be compared to their results of an LDP propeller. Next, the results of the transient $k - \omega$ simulations will be compared to the results of the quasi-steady $k - \epsilon$ simulations to investigate whether the computationally less expensive quasi-steady $k - \epsilon$ simulations can give an accurate representation of the energy losses.

Finally, multiple control volumes will be used to evaluate how the choice of control volume is affecting the solution.

4.1 Open water performance

Three different propellers will be analyzed. The first propeller is a 5-blade propeller, with diameter $D = 6.3$ meters, designed in 2006. This propeller is often used as a benchmark case within Wärtsilä, for this reason it will be used in this study to verify the method of calculating the open water characteristics. This propeller, which will be referred to as Propeller 1 from here forward, is presented in Figure 4.1. Propeller 1 is designed for an advance speed of 13 knots, corresponding to $V_{in} = 6.688$ m/s, and an RPM of 110, corresponding to $J = 0.5790$.

The other two propeller are both 4-blade propellers, with diameter $D = 7.6$ meters, which will be referred to as Propeller 2 and 3 from henceforth. Visually there is no difference between these propellers. The difference can be found in the pitch of the blades, the blades of Propeller 2 have a variable pitch while the blade of Propeller 3 have a constant pitch. As a result of this, the flow behind the propeller is affected and the loading on the propeller blades differs. It is expected that this has an influence on the efficiency and energy losses, which will be investigated in this study. Propeller 2 is presented in Figure 4.2 and the difference in blades is visualized in Figure 4.3.

(a)   (b)
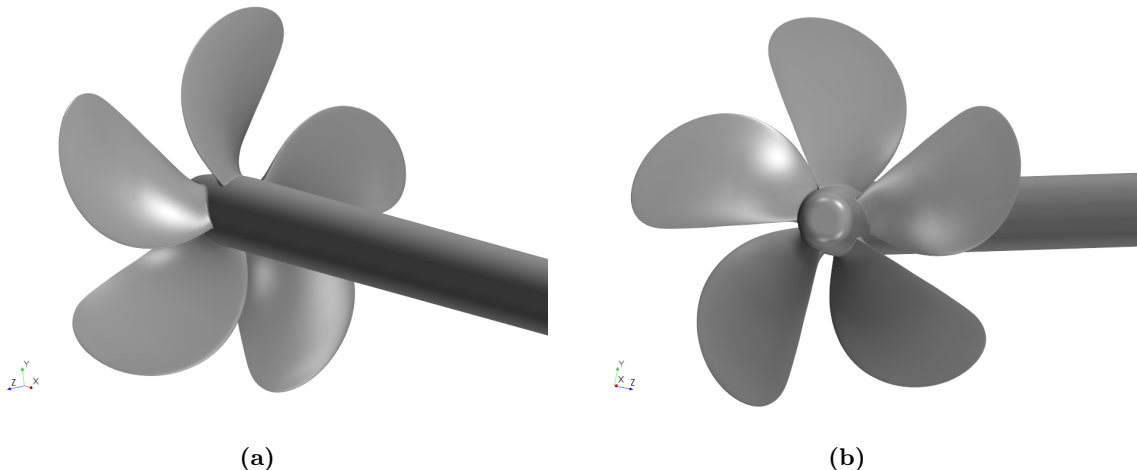
Figure 4.1: Propeller 1, a 5-blade propeller with a diameter of 6.3 meters

(a) **(b)**
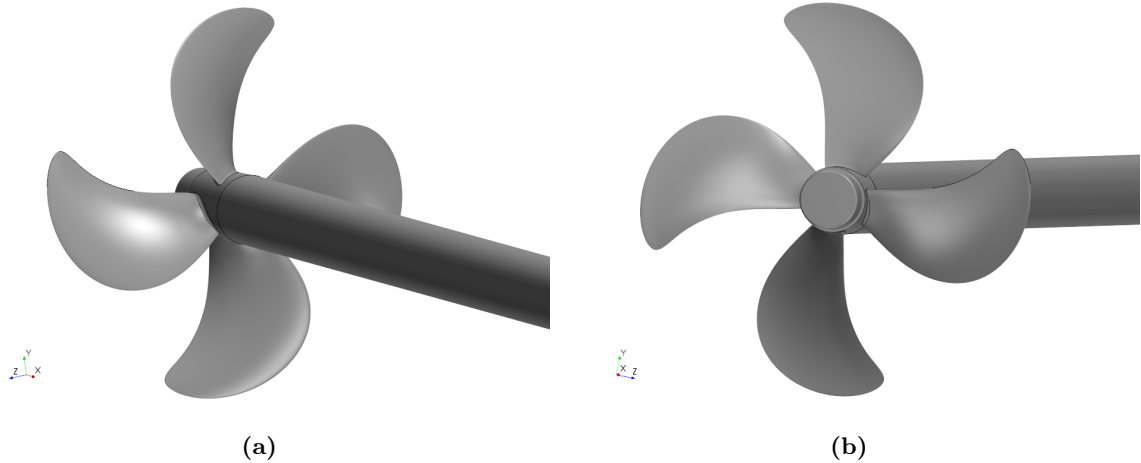
Figure 4.2: Propeller 2, a 4-blade propeller with a diameter of 7.6 meters

(a) **(b)** **(c)**
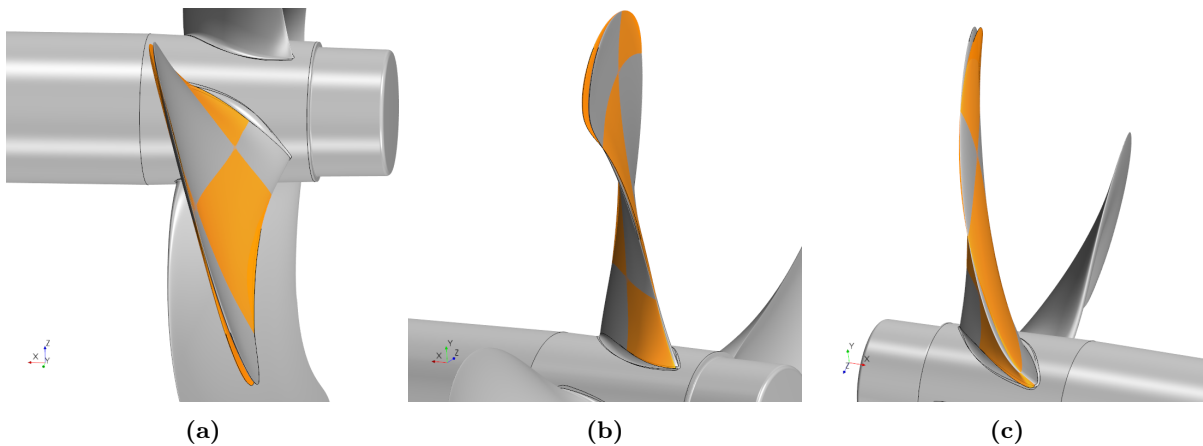
Figure 4.3: Difference in blades between Propeller 2 and Propeller 3, where the orange blade is a blade with variable pitch from Propeller 2 and the grey propeller is Propeller 3

These propellers are designed for an RPM of 91.7, with an advance speed $V_{in} = 7.4$ m/s. Two similar propellers are chosen so the results can be compared without having to take into account the difference in the geometry. In marine industries this is often done at either equal thrust or torque to obtain a fair comparison. In this study we have decided to compare the propellers at equal thrust. This leads to the adjustment of the RPM of Propeller 2 to 90.9.

In order to verify the method that has been used, the open water characteristics of Propeller 1 are compared to the benchmark calculation of Wärtsilä. The thrust and torque component are calculated, in quasi-steady full scale $k - \epsilon$ simulations in combination with the high y^+ wall treatment, at different inflow velocities to obtain the complete open water curves. In Figure 4.4 the y^+ values of Propeller 1 and 2 in these simulations are presented, which shows that the y^+ values are in line with the requirements of the high y^+ wall treatment.

The open water graphs are presented in Figure 4.5. In the operating regime the difference in efficiency in below 0.5%, with a difference less than 0.15% at the operating point. A different mesh and rotating region is used in the benchmark calculations, which can result in small differences in the calculations. Because of the small difference, especially at the design point, we assume that this setup can be used to calculate the thrust, torque and efficiency.

Propeller 2 generates slightly more thrust and torque at identical J values than Propeller 3, which can be caused by the difference in pitch of the blades. The difference in efficiency between Propeller 2 and 3 is 0.2%. The same trends are visible in the open water characteristics, which is expected due to the similarity of the geometries. Consequently, we assume that the thrust, torque and efficiency are calculated correctly in our simulations.

The design parameters of all three the propellers, including the diameter and pitch ratio and the efficiency at the operating point, are presented in Table 4.1. These settings will be used in all the simulations from here forward, except for the calculations of the open water characteristics.
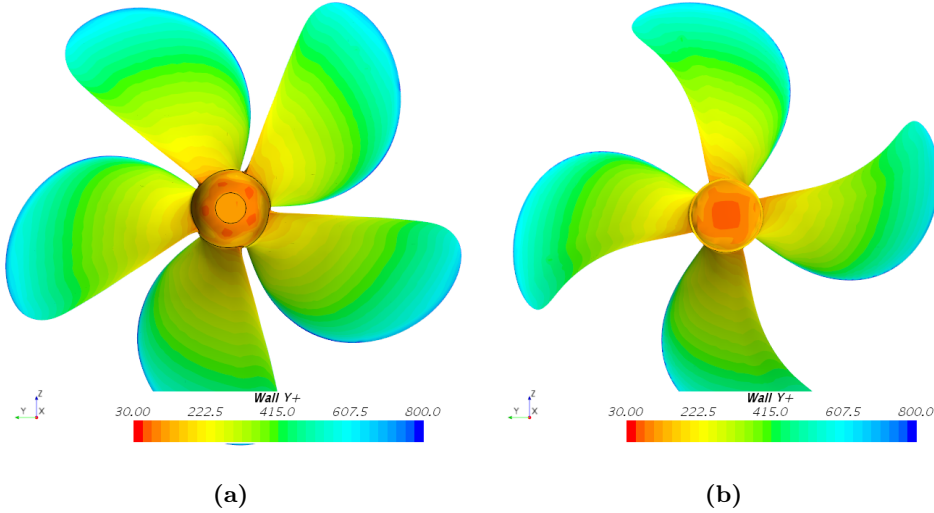
Figure 4.4: The y^+ values of (a) Propeller 1 and (b) Propeller 2 for simulations using the $k - \epsilon$ model in combination with the high y^+ wall treatment
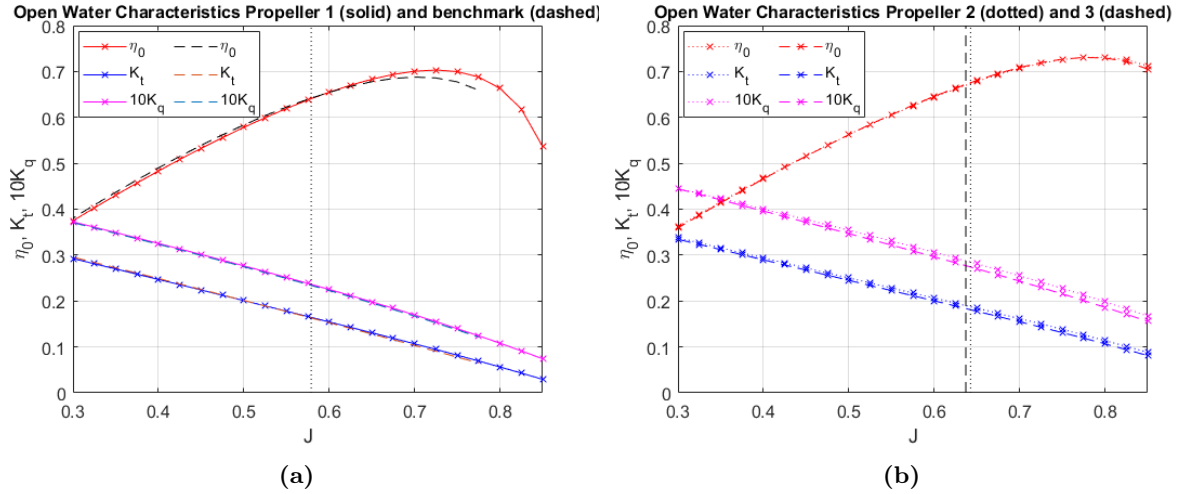
Figure 4.5: Open water characteristics of (a) Propeller 1 and the benchmark, (b) Propeller 2 and Propeller 3, where the black vertical line represents the operating point

Table 4.1: Design parameters of all three the propellers

	Diameter [m]	Pitch Ratio [-]	RPM [rpm]	V_{in} [m/s]	J [-]	η_0 [%]
Propeller 1	6.3	0.8320	110.0	6.688	0.5790	62.50
Propeller 2	7.6	0.8479	90.9	7.4	0.6427	65.52
Propeller 3	7.6	0.8479	91.7	7.4	0.6371	65.39

4.2 Energy analysis using the method by Schuiling & van Terwisga

In this section the method of Schuiling & van Terwisga will be used to analyse the different energy losses of the three propellers [27]. Our transient $k - \omega$ simulations, in combination with the all y^+ wall treatment, will be compared to the simulations performed by Schuiling & van Terwisga to verify the method of calculating the energy losses in our simulations. Unfortunately, due to confidentiality, we were not able to obtain the same propeller geometry. Hereafter, quasi-steady $k - \epsilon$ simulations using the high y^+ function will be performed and compared to the results of the transient $k - \omega$ simulations.
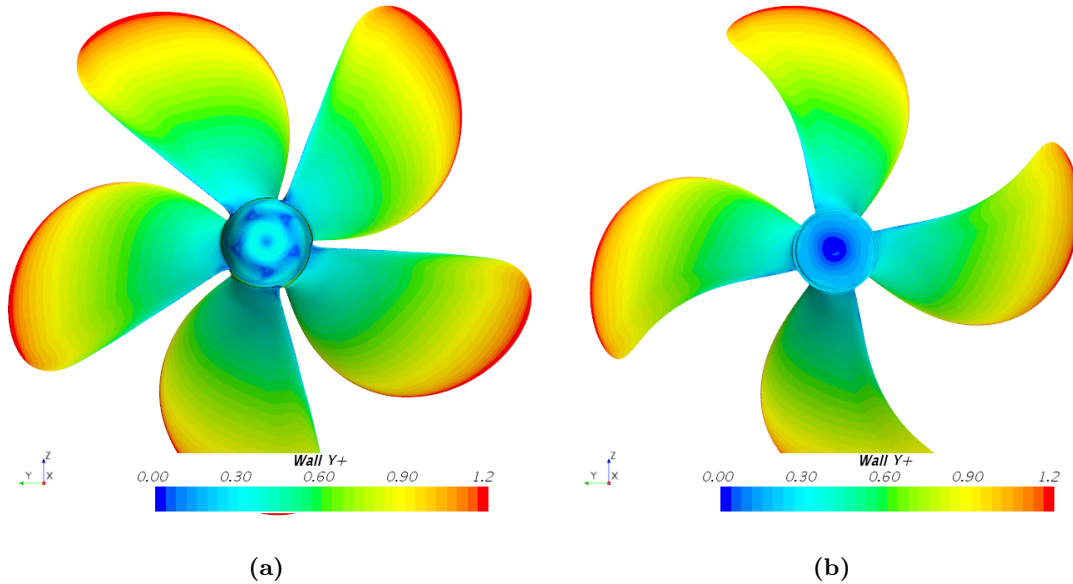
Figure 4.6: The y^+ values of (a) Propeller 1 and (b) Propeller 2 for simulations using the $k - \omega$ model in combination with the all y^+ wall treatment

4.2.1   Transient $k - \omega$ simulations

The simulations in this section are performed using the all y^+ wall treatment. As a consequence of this the mesh is changed, since lower y^+ values are preferred to fully resolve the boundary layer. In Figure 4.6 the y^+ values for Propeller 1 and 2 are presented.

The y^+ values on most of the propeller are in line with the requirements. The values near the tips are 1.2, which is a little above the desired value of 1. These values can be lowered by adding additional mesh refinements near the tip regions, This will lead to a computationally more expensive and less stable simulations. Therefore these values are accepted as a compromise.

In Table 4.2 the results of the simulations are presented. The losses are presented as a percentage of the total delivered power, where the residuals represent the percentage of total delivered power that is not accounted for in either the efficiency or the losses.

Table 4.2: Energy losses for all three the propellers and the propeller used by Schuiling & Terwisga

	Schuiling & van Terwisga [27]	Propeller 1	Propeller 2	Propeller 3
IAXL [%]	15.6	15.71	15.20	15.04
AAXL [%]	2.9	2.89	2.63	2.33
ROTL [%]	7.1	5.80	5.78	5.59
MOVL [%]	1.9	1.78	1.22	1.53
TUVL [%]	4.0	4.08	2.86	3.10
Residual [%]	3.0	5.72	5.16	5.83
$\eta_0[\%]$	65.5	63.84	67.05	66.69

Ideally we would use the same geometry of the propeller as used by Schuiling & van Terwisga. It was not possible to obtain this geometry due to confidentiality. We also do not know the advance speed and RPM of their simulation. The geometry and advance ratio are expected to have an influence on the energy losses and efficiency. Therefore, we do not expect to obtain exactly the same results.

The percentages of energy losses calculated by Schuiling & van Terwisga are in line with the percentages that were calculated in this study. The biggest difference can be observed between the energy residuals. Their residuals are 3.0%, while our simulations have residuals of 5 to 6%, indicating that our simulations are less accurate which can be the result of the difference in meshing. Schuiling & van Terwisga use a more refined mesh, which will generate more accurate results. Their mesh is also structured, while we use an unstructured mesh. The advantages of a structured mesh over an unstructured mesh are

a higher degree of quality and control and a better alignment between the cells, which will result in less computational errors.

It is difficult to compare the energy losses because of the different geometries. We know that the differences in efficiency of propellers are small. The differences in these simulations are within 2%, yielding that differences in energy losses should also be small. The different energy losses are in the same order of magnitude, even for totally different geometries. As a result, we can assume that we can use this method to calculate the energy losses.

The energy losses of Propeller 2 and 3 can be compared, since the geometries are similar. By comparing these losses, we can further verify that the method accurately measures the energy losses. Only small differences in the energy losses of Propeller 2 and 3 can be observed. The ideal axial losses are slightly different, 0.16%. These losses are mostly calculated using the thrust. The RPM of Propeller 2 was adjusted to generate the same thrust. After adjusting the RPM, the thrust of Propeller 2 is less slightly higher, although less than 1%, resulting in more ideal axial losses.

A difference in viscous losses between Propeller 2 and 3 can be noticed. Higher viscous losses could be expected for Propeller 3, since the propeller is rotating faster. Because of this, the velocity of the propeller is larger at the tips. The velocity at the propeller blades should still be zero because of the no slip wall condition. The higher rotation speed can result in higher velocity gradients. Therefore the viscous losses may increase when the RPM is increased. This difference is not caused by the propeller geometry, but by the operating conditions.

After comparing the different energy losses, we can conclude that in transient $k - \omega$ simulations the control volume method can be used to measure the energy losses.

4.2.2 Quasi-steady $k - \epsilon$ simulations

Comparing the two turbulence models

It is interesting to use a quasi-steady simulation with the $k - \epsilon$ model, provided it is accurate enough, since it is computationally less expensive. Because of this, the results of both methods will be compared in this section to evaluate whether the quasi-steady $k - \epsilon$ simulations can be used to calculate the energy losses. The results of the simulations with both models are presented in Table 4.3.

Table 4.3: Energy losses for quasi-steady $k - \epsilon$ simulations and transient $k - \omega$ simulations for all three the propellers

	Propeller 1		Propeller 2		Propeller 3	
	$k - \epsilon$	$k - \omega$	$k - \epsilon$	$k - \omega$	$k - \epsilon$	$k - \omega$
IAXL [%]	15.55	15.71	15.26	15.20	15.19	15.04
AAXL [%]	2.27	2.89	2.57	2.63	2.16	2.33
ROTL [%]	5.58	5.80	5.56	5.78	5.28	5.59
VISL [%]	5.24	-	3.52	-	3.91	-
MOVL [%]	-	1.78	-	1.22	-	1.53
TUVL [%]	-	4.08	-	2.86	-	3.10
Residual [%]	8.79	5.72	7.51	5.16	7.99	5.83
$\eta_0[\%]$	62.50	63.84	65.52	67.05	65.39	66.69

The first important difference to notice are the residuals. The residuals, which were already rather large for the transient simulations, are even higher in the quasi-steady $k - \epsilon$ simulations, resulting in even less accurate simulations. Almost all the energy losses are underpredicted, except for the ideal axial losses of Propeller 2 and 3.

A small difference, approximately 0.2 to 0.3%, can be observed in the rotational losses. The difference can be a result of the different methods of simulating the rotation of the propeller. In the transient simulation the SM method is used, where the propeller is rotated. In the quasi-steady simulation the MRF method is used, where a rotation is imposed on the rotating domain. The difference is rather small and consistent for all three propellers, thus we assume that the steady $k - \epsilon$ simulations can give a general indication of the rotational losses.

The difference in axial losses are not large, but the difference is not consistent between the propellers. The ideal axial losses increased for Propeller 2 and 3, while they are reduced for Propeller 1. A larger

difference between the additional axial losses can be observed for Propeller 1. The effect of the models on the losses seems to be influenced by the geometry of the propeller. Therefore we assume that this analysis method is most useful to analyse propellers with similar geometries, considering that the relative difference between the losses is more important when comparing similar propellers than the exact values of the energy losses.

The viscous losses are more difficult to compare. Schuiling & van Terwisga claimed that the approach of calculating the viscous losses that is used is only valid when the boundary layer is fully resolved in the RANS computation. The viscous dissipation in the cells where wall functions are applied, should be determined in an alternative way [27]. Therefore the turbulent dissipation is used to give an indication of the viscous losses. The same trend between the propellers can be noticed when comparing the $VISL$. The viscous losses are higher for Propeller 1 in comparison with the other two and the viscous losses are higher for Propeller 3 in comparison with Propeller 2, just as shown in the $MOVL$ and $TUVL$. However, a large difference between the values of the losses can be noticed and the dissipation due to the mean flow are not included in these calculations. Due to this it is difficult to calculate the viscous losses in simulations using the high y^+ wall function.

To conclude, the same effect can be observed between Propeller 2 and 3. As a result of this we can conclude that the $k - \epsilon$ simulations can be useful to compare the rotational and axial losses of two propellers with similar geometries, considering that the relative difference between the losses is more important when comparing similar propellers than the exact values of the energy losses. This method should not be used to compare different geometries, since a general correction cannot be formulated. More research can be done to investigate whether a correction can be used.

The viscous losses are difficult to capture, because they mostly occur close to the propeller which is modelled by a wall function. As a consequence, the viscous losses should be calculated with the all y^+ wall treatment in combination with the $k - \omega$ model.

Open water performance

It has been claimed that the J value influences the energy losses. When using the $k - \omega$ model in combination with the all y^+ treatment, we only calculated the operating point because of the computational costs. Using the $k - \epsilon$ model with the high y^+ wall function, the complete open water characteristics can be calculated. To confirm that the advance coefficient has an influence on the energy losses, the different components of the energy losses are calculated in the open water calculations. The resulting open water graphs are presented in Figure 4.7, where the symbols represent the efficiency and energy losses of the $k - \omega$ simulations.

In the open water graphs it can be observed that the J value has a big influence on the energy losses. The ideal axial losses are highly influenced by the advance coefficient. For a low advance coefficient, the value of the loading coefficient is larger. The loading coefficient is related to the ideal axial losses. An increase of C_t corresponds to an increase of $IAXL$ causing higher ideal axial losses for lower J values.

While the ideal axial losses decrease, the additional axial losses increase. The ideal axial losses and additional axial losses are related to each other by equation (2.45). The reduction of the thrust results in a decrease of ideal axial losses and delivered power, which results in an increase of additional axial losses.

Although we should not use this method to calculate the viscous losses, it can be noticed that the viscous losses are also influenced by the advance coefficient. This can be a result of the increasing inflow velocity, which can cause higher velocity gradients, leading to higher viscous losses.

We can conclude that the energy losses are dependent on the advance coefficient. When propellers are compared at equal thrust or torque, this can influence the J value and therefore the energy losses.

4.3 Energy analysis using multiple control volumes

The control volume method is an easy and computationally inexpensive method to give a general idea about the different energy losses of the propeller. Using this method does have some disadvantages. The results could be affected by the choice of control volume and it is difficult to capture different phenomena. Many interesting flow phenomena, such as viscous dissipation, occur close to the propeller, while other processes will occur in their own specific region. To evaluate how the choice of control volume is affecting the results, different control volumes will be investigated in this section. Two configurations will be used: one separates the control volume in cylinders and the other separates the control volume in rings. These configurations are presented in Figure 4.8. The $k - \epsilon$ model, using the MRF method to model the rotation, in combination with the high y^+ wall treatment is used.

(a)

(b)

(c)
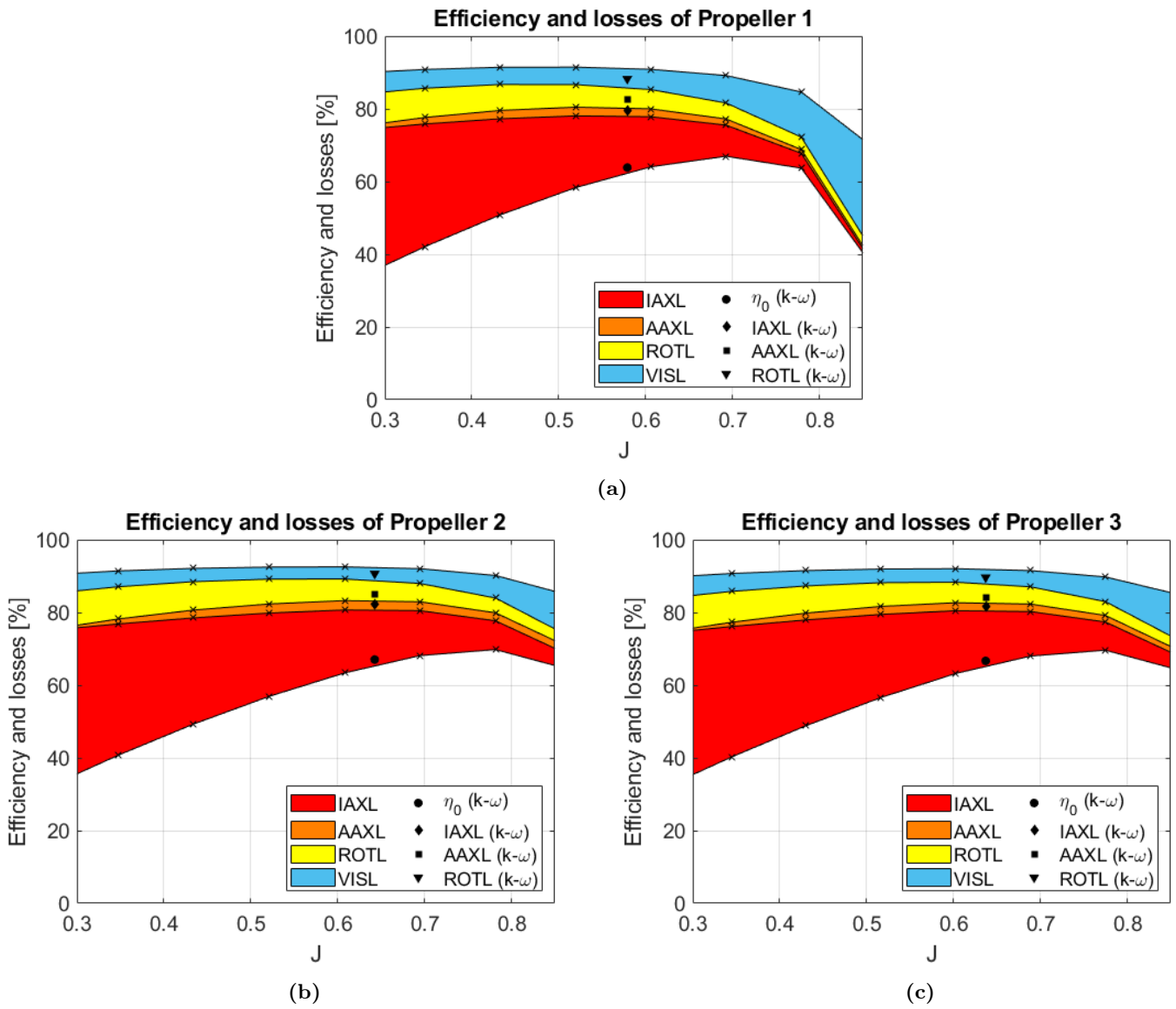
Figure 4.7: Efficiency at different J values including the energy losses of (a) Propeller 1, (b) Propeller 2 and (c) Propeller 3

(a) Configuration 1: Cylinders

(b) Configuration 2: Rings
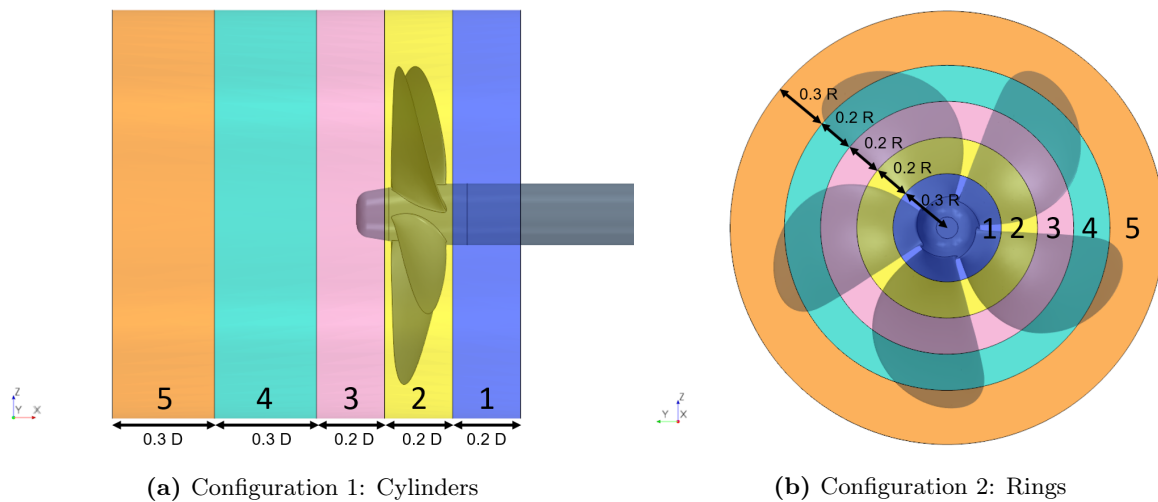
Figure 4.8: The two multiple control volumes configurations

A similar study has been performed by Andersson. She concluded that the distribution of the energy balance is highly dependent on the location of the control volume and that it is important to apply identical control volumes when comparing different design [39]. Our research differs from hers in two ways: we use multiple control volumes in one simulation, which adds extra interfaces, and we use rings instead of cylinders to divide the propeller in different regions.

4.3.1   Configuration 1: Cylinders

In this section the influence of the length of the control volume will be investigated. This will be done by placing 5 different control volumes in the simulation, as visualized in Figure 4.8a. The positions of the cylinders are presented in Table 4.4.

Table 4.4: The positions of the different cylinders used as control volumes

	$x_{in}[m]$	$x_{out}[m]$
Cylinder 1	-0.3 · D	-0.1 · D
Cylinder 2	-0.1 · D	0.1 · D
Cylinder 3	0.1 · D	0.3 · D
Cylinder 4	0.3 · D	0.6 · D
Cylinder 5	0.6 · D	0.9 · D

All the cylinders have three interfaces, just like the original control volume. The original control volume is divided in three cylinders, Cylinder 1, 2 and 3, in this new configuration, resulting in more interfaces in the original control volume, which can influence the results. To investigate whether the results are influenced, we compare the results of the simulation with one control volume to the results of the first three cylinders combined in the simulation with multiple control volumes. These results can be observed in Table 4.5.

Table 4.5: The energy losses in simulations with a single control volume and multiple control volumes

	IAXL [%]		AAXL [%]		ROTL [%]		VISL [%]	
	Single	*Multiple*	*Single*	*Multiple*	*Single*	*Multiple*	*Single*	*Multiple*
Propeller 2	15.26	15.22	2.57	2.44	5.56	5.73	3.52	3.53
Propeller 3	15.19	15.12	2.16	2.03	5.28	5.47	3.91	3.93

Some differences can be noticed between the two different methods. The rotational losses increase and the axial losses decrease. The total control volume in the simulation with the cylinders, which is all 5 of the cylinders combined, is larger than the original control volume. This whole control volume is used as the rotating region. As stated before, it is known that this has an influence on the thrust and torque, which influences the axial losses.

The larger rotating region is also expected to influence the rotational losses. Therefore, a simulation with the cylinders has been performed where Cylinder 4 and 5 are not rotating. The rotational losses calculated in the original control volume of these simulations are 5.62% and 5.32% for Propeller 2 and 3, respectively. Consequently, we can conclude that increasing the rotating region results in more rotational losses.

A small difference is still unaccounted for. This difference can be caused by the additional interfaces present in the simulation. Thus it is important to be consistent in the simulations. If you want to compare propellers, you need to use the same configuration of control volumes since the results are affected.

Different combinations of the cylinders can be used to change the length of the control volume. Some of these combinations, with their corresponding energy losses, are presented in Table 4.6.

The ideal axial losses are not influenced by the choice of control volume, because this loss component is not calculated using the interfaces or volume of the cylinders, in contrast to the other loss components. The rotational losses are affected by the choice of control volume. The rotational losses are higher when Cylinder 1 is used in the control volume. The tangential and radial velocity components are probably

Table 4.6: The energy losses for different configurations of control volumes

	Propeller 2				Propeller 3			
	IAXL [%]	*AAXL [%]*	*ROTL [%]*	*VISL [%]*	*IAXL [%]*	*AAXL [%]*	*ROTL [%]*	*VISL [%]*
Cylinder 1+2	15.22	2.09	7.24	3.40	15.12	1.88	6.97	3.76
Cylinder 2	15.22	3.61	5.81	3.38	15.12	2.03	5.47	3.74
Cylinder 2+3	15.22	3.90	4.34	3.51	15.12	3.34	4.22	3.91
Cylinder 1+2+3	15.22	2.44	5.73	3.53	15.12	2.03	5.47	3.93
Cylinder 1+2+3+4	15.22	2.09	5.32	3.61	15.12	1.70	4.95	4.03
Cylinder 1+2+3+4+5	15.22	2.05	5.22	3.66	15.12	1.38	4.78	4.10

smaller at the inflow interface of Cylinder 1, since the inflow of Cylinder 2 is closer to the propeller and therefore there may be more rotation in this inflow. Less rotation in the inflow can result in a larger difference between the in- and outflow which results in higher rotational losses.

When additional cylinders are added after the control volume, the rotational losses slowly decrease. The rotation of the flow is generated by the propeller and will slowly decay further away from the propeller. Due to this, the rotational losses are lower when the control volume is longer. When there is less rotation in the flow, the axial component of the flow increases and consequently the axial energy increases. The axial energy is related to the additional axial energy by equation (2.45). When the axial energy increases, the additional axial losses decrease. This may explain why the same trend can be noticed in the additional axial losses as in the rotational losses.

To conclude, we have shown that the choice of control volume affects the solution, thus it is important to use the same control volumes when comparing propellers.

4.3.2 Configuration 2: Rings

In this section the control volume will be divided in different rings, as visualized in Figure 4.8b. The radius and volume fractions of the rings are presented in Table 4.7.

Table 4.7: The radius and volume of the different rings used as control volumes

	$z_{in}[m]$	$z_{out}[m]$	**Volume fraction of total control volume [%]**
Ring 1	$0 \cdot D$	$0.3 \cdot D$	4.6
Ring 2	$0.3 \cdot D$	$0.5 \cdot D$	11.1
Ring 3	$0.5 \cdot D$	$0.7 \cdot D$	16.9
Ring 4	$0.7 \cdot D$	$0.9 \cdot D$	22.6
Ring 5	$0.9 \cdot D$	$1.2 \cdot D$	44.7

Using different rings as control volumes could be useful to evaluate in which region the most energy is lost, which can be useful to determine whether a ESD can sufficiently increase the efficiency of a propeller. Additional interfaces are added in between the rings, which can influence the efficiency and energy losses. To investigate this influence, the energy losses in all rings combined are compared to the energy losses of a single control volume. The results of this comparison are presented in Table 4.8.

Table 4.8: The energy losses in simulations with a single control volume and multiple control volumes

	IAXL [%]		AAXL [%]		ROTL [%]		VISL [%]	
	Single	*Multiple*	*Single*	*Multiple*	*Single*	*Multiple*	*Single*	*Multiple*
Propeller 2	15.26	15.27	2.57	2.30	5.56	5.58	3.52	3.36
Propeller 3	15.19	15.17	2.16	1.88	5.28	5.29	3.91	3.71

Only small differences can be noticed between the two simulations in the ideal axial losses and rotational losses. Introducing more interfaces in the simulation does not seem to have a significant influence on these losses.

A larger difference can be noticed between the additional axial losses. This component of the losses is dependent on axial energy, work by pressure, ideal axial losses and delivered power as stated in equation (2.45). The ideal axial losses are slightly influenced by the interfaces present in the control volume, therefore a small difference can be expected between the two simulations for all four the components necessary to calculate the additional axial losses. If all these little difference are added together, this can result in a larger difference between the additional axial losses of the two configurations, which can explain why the differences between the two configurations is larger for the additional axial losses than the ideal axial losses and rotational losses.

Since the differences are small, we assume that this configuration can be used to investigate the energy losses in different rings. It is still important to be consistent. If you want to compare propellers, the same configuration of control volumes should be used.

The difference in blades between Propeller 2 and 3, variable and constant pitch, should result in a different loading of the blades. To confirm this, we calculate the thrust generated in each ring. These results are presented in Table 4.9.

Table 4.9: The thrust of Propeller 2 and 3 in the different rings

	T [kN]	
	Propeller 2	*Propeller 3*
Ring 1	26.5	25.2
Ring 2	193.7	184.9
Ring 3	441.0	408.2
Ring 4	598.9	593.3
Ring 5	198.7	238.2

From the table we can conclude that the loading is different. More thrust is generated in the first four rings by Propeller 2, which is balanced by the additional thrust generated in Ring 5 by Propeller 3.

The percentages of the different loss components in every ring are calculated to investigate in which region the different energy losses are most dominant. These results are presented in Table 4.10.

Table 4.10: The loss components in the rings normalized by the loss components in the total control volume

	Propeller 2				Propeller 3			
	IAXL [%]	*AAXL [%]*	*ROTL [%]*	*VISL [%]*	*IAXL [%]*	*AAXL [%]*	*ROTL [%]*	*VISL [%]*
Ring 1	1.8	-23.5	11.8	6.8	1.7	-23.4	14.6	6.5
Ring 2	13.3	-1.7	22.4	7.4	12.7	-123.9	20.5	7.0
Ring 3	30.2	127.4	31.2	19.6	28.2	96.3	27.8	19.1
Ring 4	41.1	155.7	1.4	40.2	40.8	200.5	3.8	37.6
Ring 5	13.6	-158.7	33.0	25.6	16.5	-163.8	33.5	30.1

Most of the rotational losses are expected to appear close to the hub and at the tip of the blades due to the hub vortex and tip vortices. Some rotational losses are also expected in the other rings as a consequence of the rotational slipstream created by the propeller. The largest percentage of rotational losses are observed in Ring 5 but only a small percentage is present in Ring 1. The volume fraction increases with increasing radii, as shown in Table 4.7, which can result in smaller percentages of rotational losses in the first ring. Therefore, the percentage of losses are divided by the volume fraction to obtain the energy density in each ring. The results of this are presented in Table C.1. From this table we can conclude that the energy density of the rotational losses is the highest in the first ring, as expected due to the small volume and the high rotational losses because of the hub vortex.

The distribution of the rotational losses is different between the two propellers. More rotational losses are measured in Ring 1 and 5 for Propeller 3, while more rotational losses can be noticed Ring 2 and 3

for Propeller 2. This knowledge can be important when deciding whether a propeller can benefit from an Energy Saving Device. A Propeller Boss Cap Fins, for example, is expected to suppress the hub vortex. Based on this, the PBCF may be more effective for Propeller 3 since more rotational losses are present close to the hub.

The axial losses are highly dependent on the thrust and therefore also show the same trend as the thrust. In the regions where the most thrust is generated, the largest percentage of ideal axial losses and additional axial losses are measured. When Propeller 2 generated more thrust in a ring, the axial losses are also higher in comparison with Propeller 3.

Negative values of additional axial losses indicate that the axial energy, E_x, and work by pressure, P, are lower than the delivered power and ideal axial losses in these regions. The E_x might be low in the first regions, since most of the flow is rotated by the propeller and root blade vortices and a hub vortex are generated. In the last region the same effect may be measured due to the tip vortices and the contraction of the flow after the propeller. To be able to give a better explanation for the additional losses, E_x and P should be investigated further in the different rings.

To conclude, this configuration of the control volumes can be used to investigate the energy losses in different regions around the propeller. This can be useful if we want to investigate whether a ESD can significantly increase the efficiency of a propeller

4.4   Recap

In this chapter the control volume method was used to investigate the energy losses of a propeller in open water. First the three different propellers were introduced and the open water characteristics were presented.

Hereafter, the method by Schuiling & van Terwisga was used to analyse the energy losses [27]. The simulations were performed using the SST $k - \omega$ model with the Sliding Mesh (SM) method to simulate the rotation. The energy losses were in the same order of magnitude as the propeller from Schuiling & van Terwisga. As a result of this, we assumed that the control volume method can be used to measure the energy losses in transient $k - \omega$ simulations. Our energy residuals, however, are much higher, which can be the result of the difference in mesh.

Next, the results of the transient $k - \omega$ simulations were compared to the results of quasi-steady $k - \epsilon$ simulations to investigate whether the computationally less expensive quasi-steady $k - \epsilon$ simulations can give an accurate representation of the energy losses. The residuals were increased even more, which results in less accurate simulations. Similar effects of the different turbulence models were shown for Propeller 2 and 3. Therefore we concluded that the quasi-steady Standard $k - \epsilon$ simulations can be used to give a general indication of the rotational and axial losses for similar propellers, considering that the relative difference between the losses is more important when comparing the propellers than the exact values of the energy losses. A wall function was used in these simulations, as a consequence the molecular viscous losses and turbulent viscous losses could not be calculated. The $k - \omega$ model should be used when the viscous losses are calculated.

After this, the energy losses were calculated at multiple advance coefficients, which showed that the advance coefficient influences the energy components. Thus it is important to compare propellers at similar advance coefficients.

Finally, multiple control volumes were used to evaluate how the choice of control volume is affecting the solution. First the control volume was divided in multiple cylinders. These simulations confirmed that the choice of control volume affects the results, yielding that it is important to use identical control volumes when comparing propellers.

Next, the control volume was separated in multiple rings to evaluate the energy losses in different areas around the propeller. This can be a useful tool to investigate whether an Energy Saving Device can sufficiently increase the efficiency of a propeller.

5 | Analysis of the Propeller Boss Cap Fins (PBCF)

In the previous chapters it was explained that different methods have been used to determine energy losses. The relevant theory regarding the control volume method was presented and the numerical methods necessary to be able to use the control volume method were explained. This control volume method was used in Chapter 4, using either one of multiple control volumes. The control volume method will now be used to investigate the effects of the PBCF.

First the different PBCFs will be presented. Their effects on the open water characteristics will be calculated. Next the effect of the PBCF on the energy losses will be investigated using the method by Schuiling & van Terwisga [27]. Additionally, the energy losses will be investigated using multiple control volumes to evaluate the effect of the PBCF in different regions.

Finally a parametric study of the PBCF will be done. Four different parameters will be changed, the pitch angle, the length of the fin, the outer radius of the PBCF and the phase shift angle. The effects of these changes on the efficiency and the energy losses will be investigated.

5.1 Open water performance

A lot of energy is lost at the hub due to the hub vortex. The presence of the hub vortex is a result of the merging of the vortices generated at the blade roots. These vortices are generated due to the difference in pressure between the face and back sides of the blades. The hub vortex wastes a lot of energy since it introduces a strong adverse swirl into the propeller slip stream [47].

The Propeller Boss Cap Fins is a hubcap with small fins attached to it, introduced in 1988 by Ouchi, with the intention to reduce the hub vortex by stopping the merger of the root blade vortices. Lesser adverse separated axial vortices will be generated in place of the strong hub vortex [23]. The PBCF has multiple positive effects, such as the reduction of hub drag, the reduction of net torque and the increase of thrust.

Wärtsilä has designed a PBCF, called the EnergoProFin (EPF). In order to investigate how the energy losses are affected by a PBCF, a geometry of a PBCF based on the EPF has been designed. This geometry is a simplified version of the EPF. The fins are simple straight airfoils, without camber. Camber is expected to be an important design factor of the PBCF, but is difficult to implement in a parametric design. Therefore we have chosen to not incorporate this in our geometry.

A PBCF is designed based on the geometry of the propeller. The number of blades of the propeller, for example, is often the number of fins of the PBCF, which results in different PBCFs for the studied propellers. In Figure 5.1 Propeller 1 is presented with and without the PBCF and Figure 5.2 shows the design of the PBCF for Propeller 2 and 3.

We know from the previous chapter that the energy losses are dependent on the J value. Furthermore, it is claimed that the PBCF reduces the net torque and increases the thrust, which will increase the efficiency. The torque and thrust also depend on the advance coefficient, thus it is interesting to investigate how the PBCF influences the open water characteristic. The simulations are performed on full scale using the $k - \epsilon$ model in combination with the high y^+ wall treatment. In Figure 5.3 the y^+ values of Propeller 1 and 2 are shown, which are in line with the requirements for the high y^+ wall treatment.

The effects of the PBCF on the open water characteristics are presented in Figure 5.4. The graphs clearly show that the thrust is increased and the torque is reduced in the complete operating regime, causing the efficiency to increase as well.

In the previous chapter, in Figure 4.7, it has been shown that the rotational losses decrease when J increases. Since the PBCF is designed to decrease the rotational losses, we expect that the efficiency increase is lower at higher J values. This effect can be observed in the graphs of Figure 5.4.
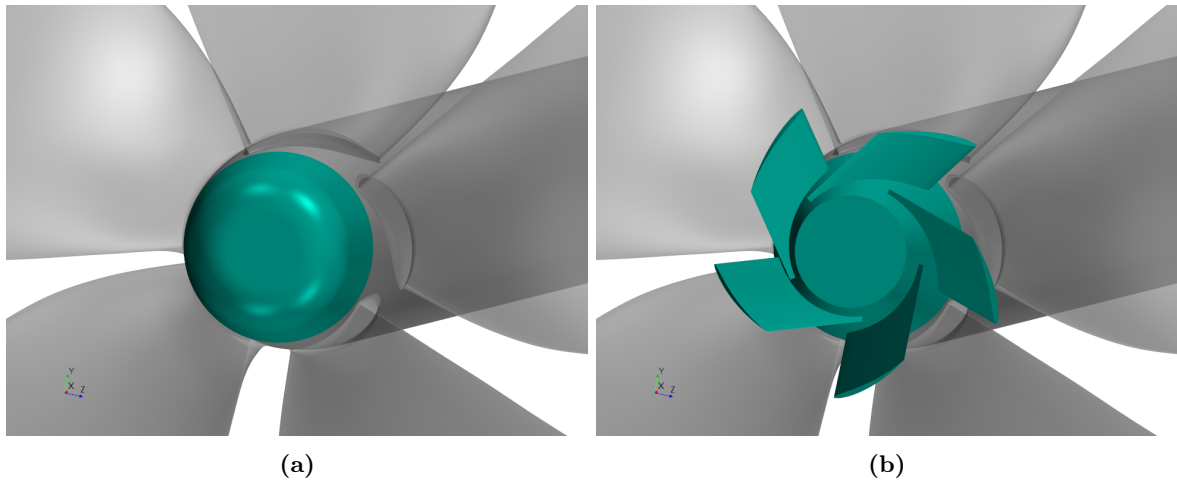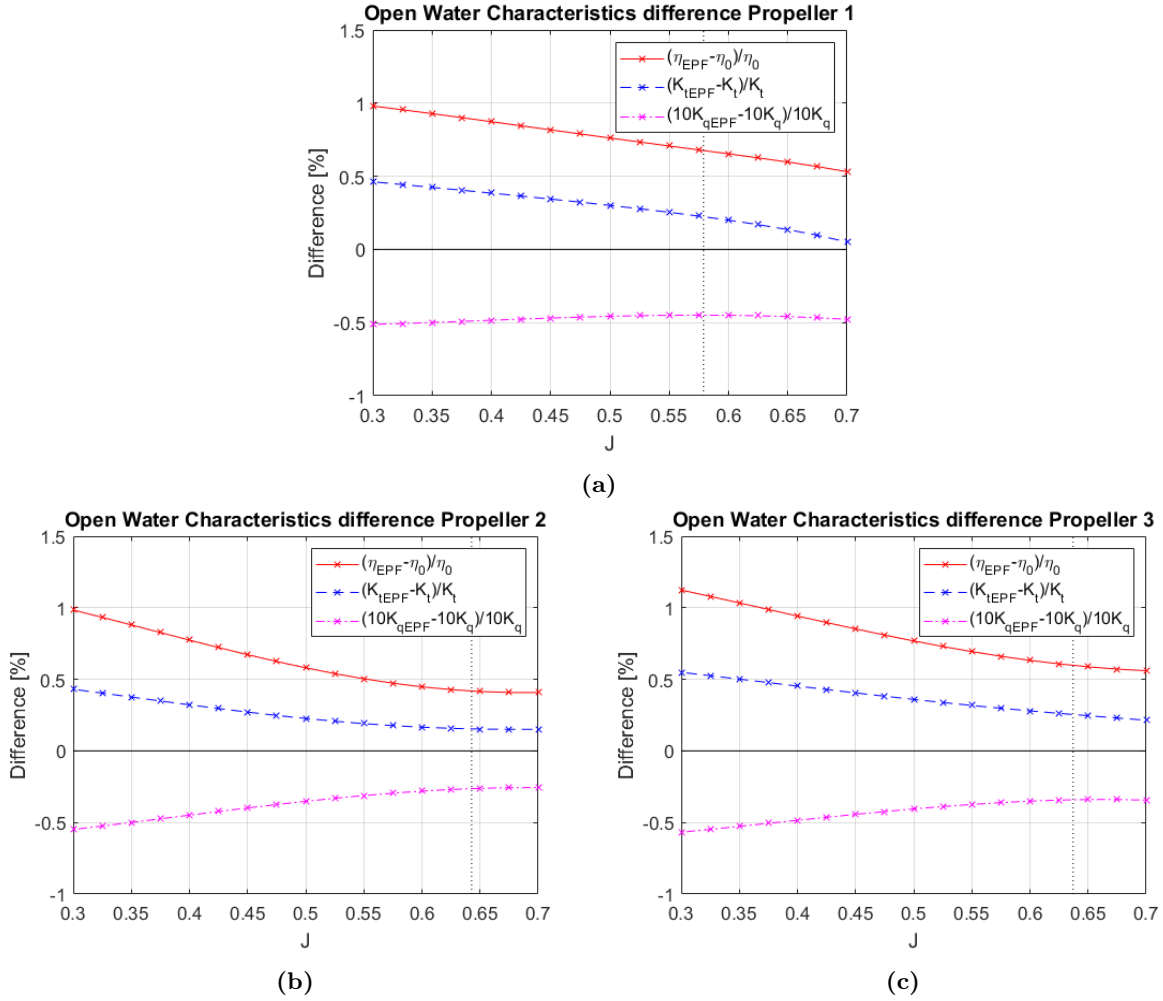
Figure 5.1: The hubcap of Propeller 1 (a) without PBCF and (b) with PBCF
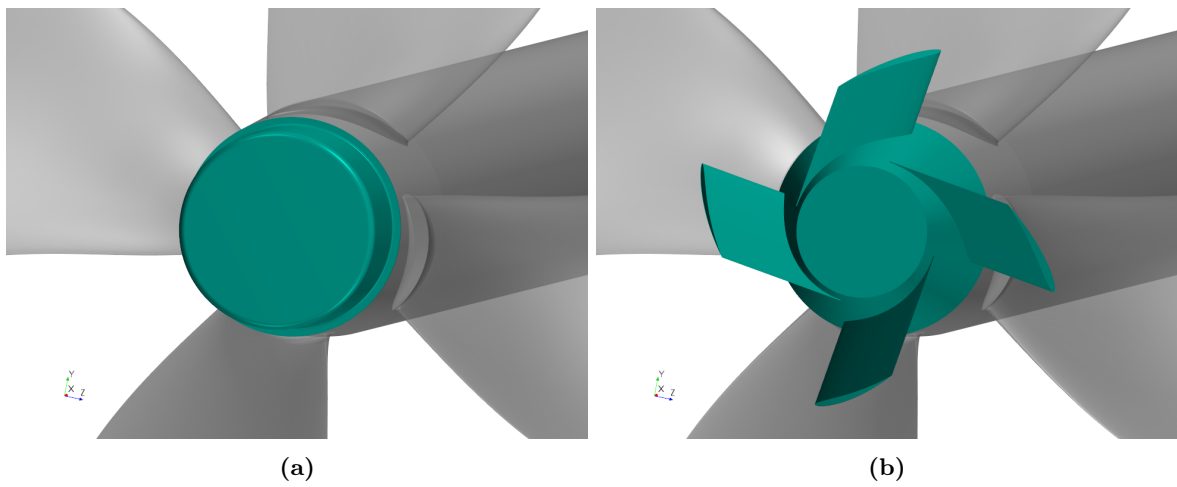
Figure 5.2: The hubcap of Propeller 2 (a) without PBCF and (b) with PBCF
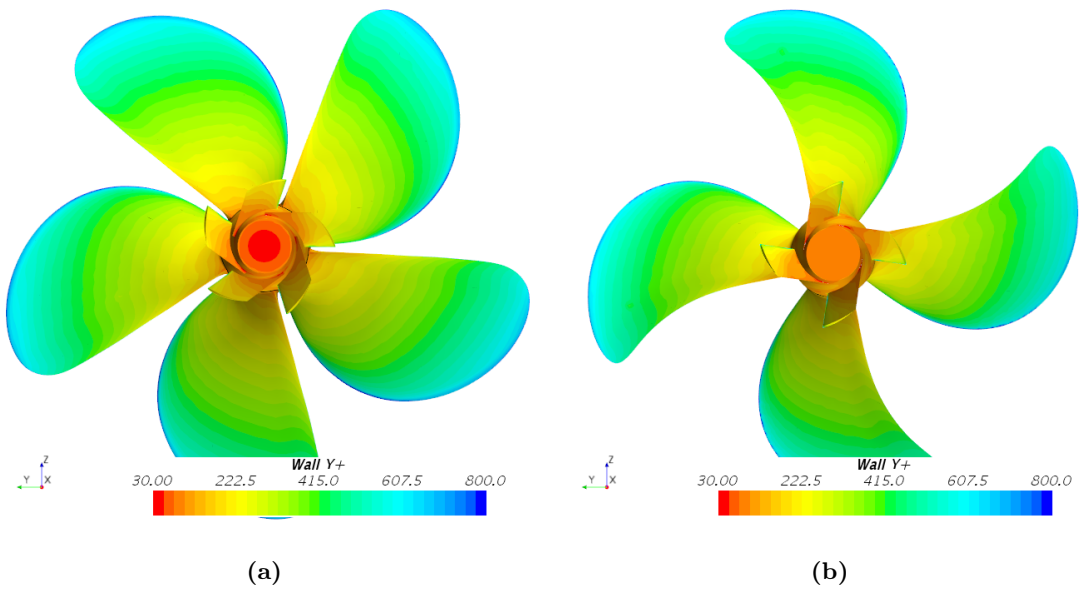
Figure 5.3: The y^+ values of (a) Propeller 1 and (b) Propeller 2 for simulations using the $k - \epsilon$ model in combination with the high y^+ wall treatment

(a)

(b)

(c)

Figure 5.4: The difference in open water characteristics with the PBCF for (a) Propeller 1, (b) Propeller 2 and (c) Propeller 3

5.2   Energy analysis using the method by Schuiling & van Terwisga

In this section the method of Schuiling & van Terwisga will be used to analyze the influence of the PBCF on the efficiency and the different energy losses of the three propellers, using transient $k - \omega$ simulations [27]. The different effects of the PBCF will be investigated in these simulations. The all y^+ wall treatment is used in $k - \omega$ simulations. Therefore, it is important to check the y^+ around the PBCF. The y^+ values, presented in Figure 5.5, including the PBCF are conform the requirements.

In Table 5.1 the results of the simulations using the control volume method by Schuiling & van Terwisga are presented for all three the propellers. A clear difference between the rotational losses can be observed. The rotational losses are decrease for every propeller, which is the design purpose of the PBCF. The decrease of these losses are not consistent between the propellers, the rotational losses are reduced less for Propeller 2, while the effect on Propeller 1 is the largest. This yields that the geometry of the propeller affects the influence of the PBCF on the rotational losses. The PBCF may be less effective for Propeller 2, since less energy was present close to the hub, as was shown in Table C.1.

The PBCF should stop the merger of the root blade vortices, which should be the reason for the reduction of rotational losses. To confirm this, the vorticity in the x-direction in the x, y-plane is calculated and displayed in Figure 5.6. The figure on the left hand side, without the PBCF, clearly shows a strong vortex originating at the hub, which can be recognized as the hub vortex. In the figure on the right hand side, with the PBCF, this strong vortex is suppressed. Small blobs of vorticity are present in the wake of the propeller with the PBCF. This confirms that less strong axial vortices are present instead of the hub vortex, as predicted.

The PBCF does not seem to have an influence on the additional axial losses of Propeller 2, whereas
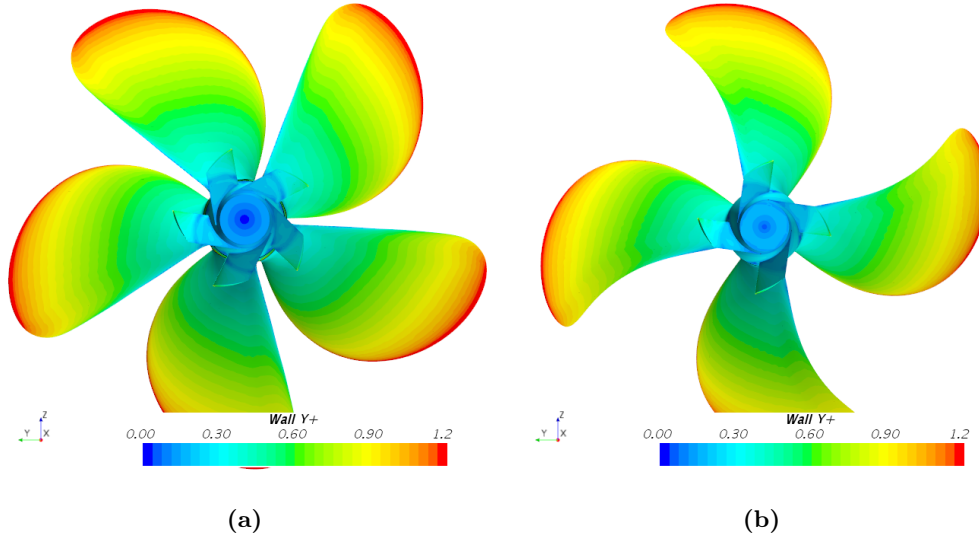
Figure 5.5: The y^+ values of (a) Propeller 1 and (b) Propeller 2 for simulations using the $k - \omega$ model in combination with the all y^+ wall treatment
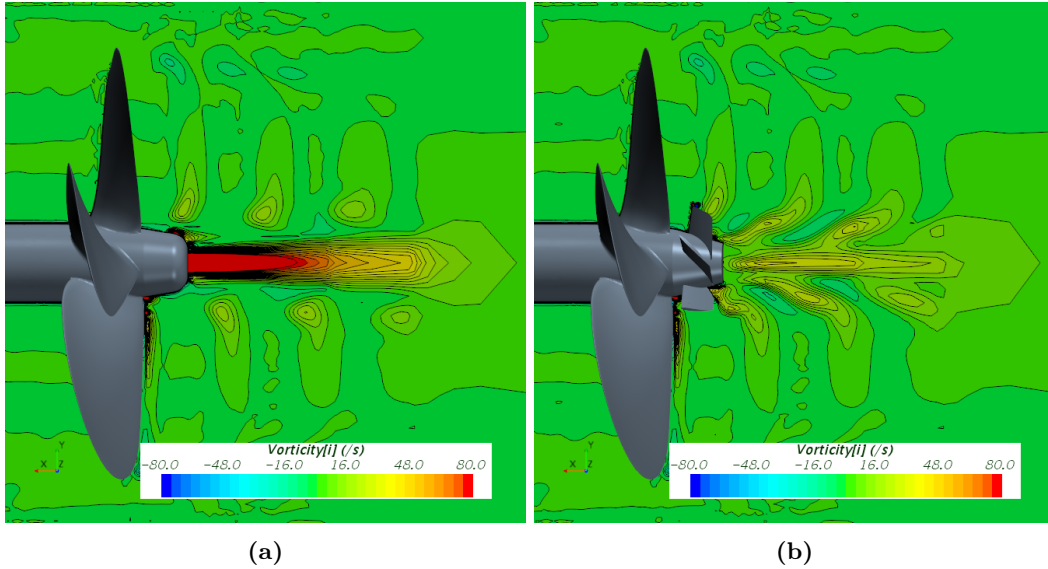
Figure 5.6: Vorticity (x-component) behind Propeller 1 (a) without PBCF and (b) with PBCF, which shows that the PBCF reduces the hub vortex

Table 5.1: Comparison of energy losses with and without the PBCF

	IAXL [%]	AAXL [%]	ROTL [%]	MOVL [%]	TUVL [%]	η_0[%]
Propeller 1	15.71	2.89	5.80	1.78	4.08	63.84
Propeller 1 with PBCF	15.94	2.47	5.28	1.80	4.09	64.49
Difference	0.23	-0.42	-0.52	0.02	0.01	0.65
Propeller 2	15.20	2.63	5.78	1.22	2.86	67.05
Propeller 2 with PBCF	15.27	2.64	5.49	1.23	2.84	67.26
Difference	0.07	0.01	-0.29	0.01	-0.02	0.21
Propeller 3	15.04	2.33	5.59	1.53	3.10	66.69
Propeller 3 with PBCF	15.23	2.11	5.21	1.26	2.95	67.41
Difference	0.19	-0.22	-0.38	-0.27	-0.15	0.72

these losses are reduced for the other propellers. The axial losses are dependent on the thrust and torque. Because of this, we investigate the influence of the PBCF on the thrust and torque on the hub and hubcap. The other components are not taken into account, because the PBCF does not have an significant influence on these components. The thrust and torque on all components can be found in Table C.2. The torque and thrust on the hub and hubcap are presented in Table 5.2.

Table 5.2: The torque (Q) and thrust (T) on the hub, hubcap and PBCF

		Q [Nm]	T [N]
Propeller 1	*Hub & Hubcap*	$1.78 \cdot 10^2$	$-1.14 \cdot 10^4$
Propeller 1 (PBCF)	*Hub & PBCF*	$-2.88 \cdot 10^3$	$-7.28 \cdot 10^3$
	Difference	$-3.06 \cdot 10^3$	$4.12 \cdot 10^3$
Propeller 2	*Hub & Hubcap*	$3.95 \cdot 10^2$	$-7.26 \cdot 10^3$
Propeller 2 (PBCF)	*Hub & PBCF*	$-4.83 \cdot 10^3$	$-7.70 \cdot 10^3$
	Difference	$-5.23 \cdot 10^3$	$-0.44 \cdot 10^3$
Propeller 3	*Hub & Hubcap*	$3.70 \cdot 10^2$	$-1.15 \cdot 10^4$
Propeller 3 (PBCF)	*Hub & PBCF*	$-5.56 \cdot 10^3$	$-8.75 \cdot 10^3$
	Difference	$-5.93 \cdot 10^3$	$2.78 \cdot 10^3$

The total amount of torque and thrust generated by Propeller 1 is less due to the geometry of the propeller, consequently the values cannot directly be compared. It can be observed that the torque reduces for all three propellers, as predicted. The thrust, however, reduces for Propeller 2, while it increases for Propeller 1 and 3. This could be the reason why the additional axial losses are not reduced for Propeller 2.

In this section we investigated how the PBCF affects the energy losses and if the expected phenomena occur. The rotational losses reduce, as a result of the suppression of the hub vortex.

5.3 Energy analysis using multiple control volumes

In the previous section we investigated the effect of the PBCF on the energy losses in the complete control volume. Earlier we have introduced a method with multiple control volumes to investigate the different energy losses in separate regions. In this section, this method will be used to investigate the difference in energy losses between the propeller with and without a PBCF in different regions around the propeller. Only the second configuration of the multiple control volumes, as shown in Figure 4.8b, will be used.

From these simulations we can conclude that the PBCF only significantly affects the energy losses in the first ring. The differences between the energy densities of the simulations with and without the PBCF are presented in Table C.3. The biggest difference can be observed between the rotational losses, which is the purpose of the PBCF.

The difference between the rotational losses in the first ring without and with the PBCF and the percentage of recovered rotational losses in this ring are calculated and presented in Table 5.3.

Table 5.3: The effect of the PBCF on the rotational losses close to the hub

	Difference in ROTL [%]	Percentage of losses recovered [%]
Propeller 2	-0.28	42.4
Propeller 3	-0.35	45.5

Although the total amount of rotational losses, in the original control volume, was higher for Propeller 2, the PBCF is more effective for Propeller 3. This is the result of the different distribution of the rotational losses. A higher percentage of the rotational losses was present in the first ring for Propeller 3. 42 to 46 % of the rotational losses in this ring are recovered by the PBCF, while the losses in the other rings are not affected. Hence not the total amount of rotational losses, but the rotational losses close to the hub can give a good indication whether a PBCF can sufficiently increase the efficiency of a

propeller, indicating that using multiple control volumes can be useful to investigate the distribution of the rotational losses before recommending a PBCF.

5.4 Parametric study of the PBCF

In the previous section it was shown that the PBCF increases the efficiency by suppressing the hub vortex. The design of the PBCF was a simplification of the EPF developed by Wärtsilä. To investigate whether we can improve this design using the control volume method, a parametric study of the PBCF has been performed and analysed. Four different parameters will be varied, the pitch angle of the fin α, the outer radius of the PBCF R_{fin}, the length of the fin L_{fin} and the the phase shift angle β. A schematic representation of these parameters is presented in Figure 5.7 and the initial values of the parameters are shown in Table 5.4.

Normally all the parameters are varied simultaneously in a parametric study. This would result in more that 350 000 simulations. Therefore, it has been chosen to use a parametric sweep for every parameter instead, indicating that only one parameter is changed, while the other parameters are kept constant at their original value as shown in Table 5.4. The results of the parametric sweep can be dependent on the settings of the other parameters, as a consequence the results of the parametric sweep might be different when the other parameters are varied simultaneously.

Table 5.4: Initial values of the parameters of the PBCF

	α [deg]	R_{fin}/R_{prop} [-]	L_{fin}/L_{max} [-]	β [deg]
Propeller 1	40	0.30	1.0	62
Propeller 2	37	0.30	1.0	8
Propeller 3	37	0.30	1.0	8

For these simulations it has been chosen to use the $k - \epsilon$ model with the MRF method to model the rotation, in combination with the high y^+ wall treatment. These methods have been chosen since a lot of simulations need to be performed for each parameter before a trend can be observed. After the parametric study three settings of the varied parameter will be chosen and three new simulations with these settings will be performed using the quasi-steady $k - \omega$ model in combination with the all y^+ wall treatment. These simulations will be used to investigate why one setting performs better than the other. The $k - \omega$ model is chosen since it solves the boundary layers more accurately, which is more useful when visually investigating the influence of the parameters.

(a)   (b)
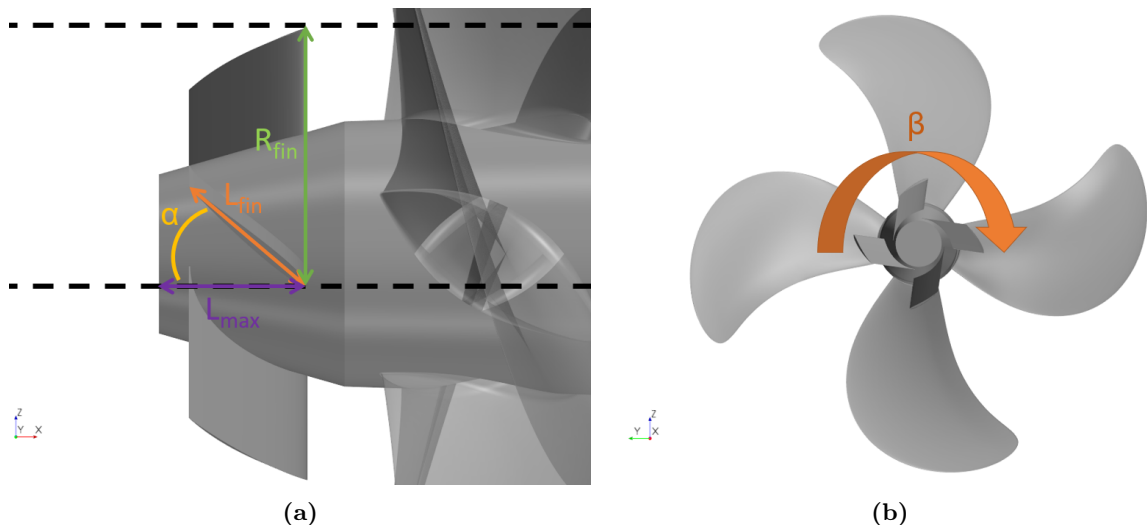
Figure 5.7: The schematic representation of the parameters of the PBCF, where α is the pitch angle of the fin, R_{fin} the outer radius of the PBCF, L_{fin} the length of the fin, β the phase shift angle and L_{max} the maximum length of the fin at $\alpha = 0°$
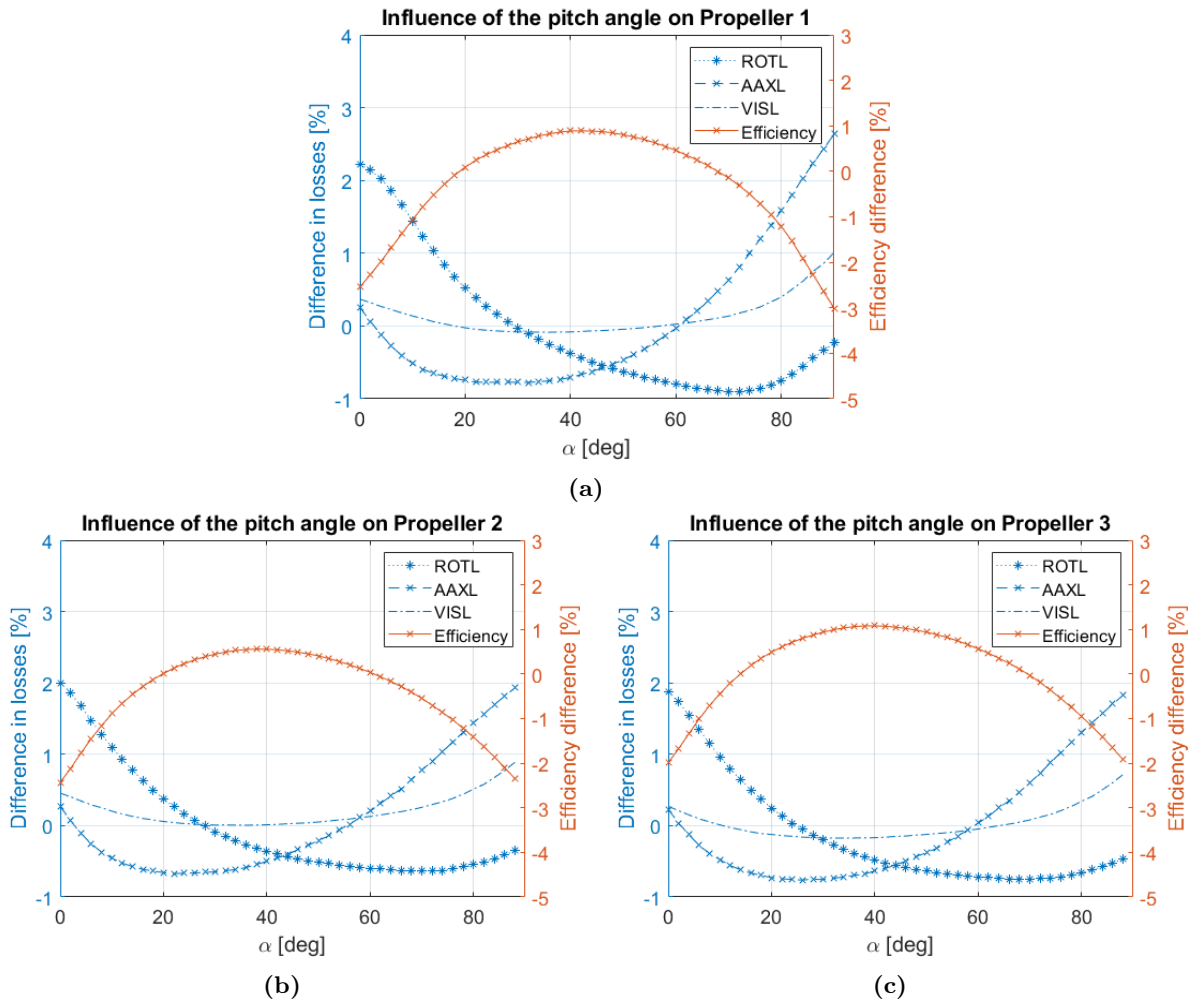
Pitch angle of the fins (α)

The first parameter that will be varied is α, the pitch angle of the fins. Often it is claimed that the combination of the pitch, the length of the fin and the outer diameter of the PBCF is important [23]. In this section the influence of the pitch angle of the fin on the efficiency and energy losses will be investigated. The pitch angle will be varied from 0 to 90 degrees with a step of 2 degrees for all three the propellers. An angle of 0 degrees is parallel to the inflow and an angle of 90 degrees is perpendicular to the inflow. The results of this parametric studies are shown in Figure 5.8.

The graphs clearly show that α has a big influence on the efficiency of the propeller. Similar curves of the efficiency and losses can be seen for all three of the propellers, but the optimum efficiency is slightly different, approximately 42 degrees for Propeller 1 and 38 degrees for Propeller 2 and 3.

The efficiency increases when α is larger, mostly caused by the reduction of rotational losses. When $\alpha > 40°$, the efficiency starts to decrease as a consequence of the increase in additional axial losses and eventually also the increase in rotational losses. These effects will be investigated in simulations of Propeller 2 with $\alpha = 28°$, $40°$ and $54°$. First it is interesting to see if the hub vortex is suppressed by the PBCF, since this is the purpose of the PBCF. In order to investigate this, the vorticity in the x-direction in the x, y-plane is plotted in Figure 5.9.

These figures clearly show that the hub vortex is suppressed by the PBCF for all three α. A smaller hub vortex is still present for lower α, as shown in Figure 5.9a. The angle of the fins is closer to the angle of the inflow at lower α, which makes it easier for the flow to pass the fins. The fins affect the flow, since the reduction of the hub vortex can be noticed, but will not completely prevent the root blade vortices from merging further away from the hub. The fins do generate some additional rotational losses, causing the increase of rotational losses at small α instead of a reduction.

(a)

(b)

(c)

Figure 5.8: The influence of the pitch angle α on the efficiency and energy losses for (a) Propeller 1, (b) Propeller 2 and (c) Propeller 3

(a) Propeller 2 with $\alpha = 28°$ **(b)** Propeller 2 with $\alpha = 40°$

(c) Propeller 2 with $\alpha = 54°$
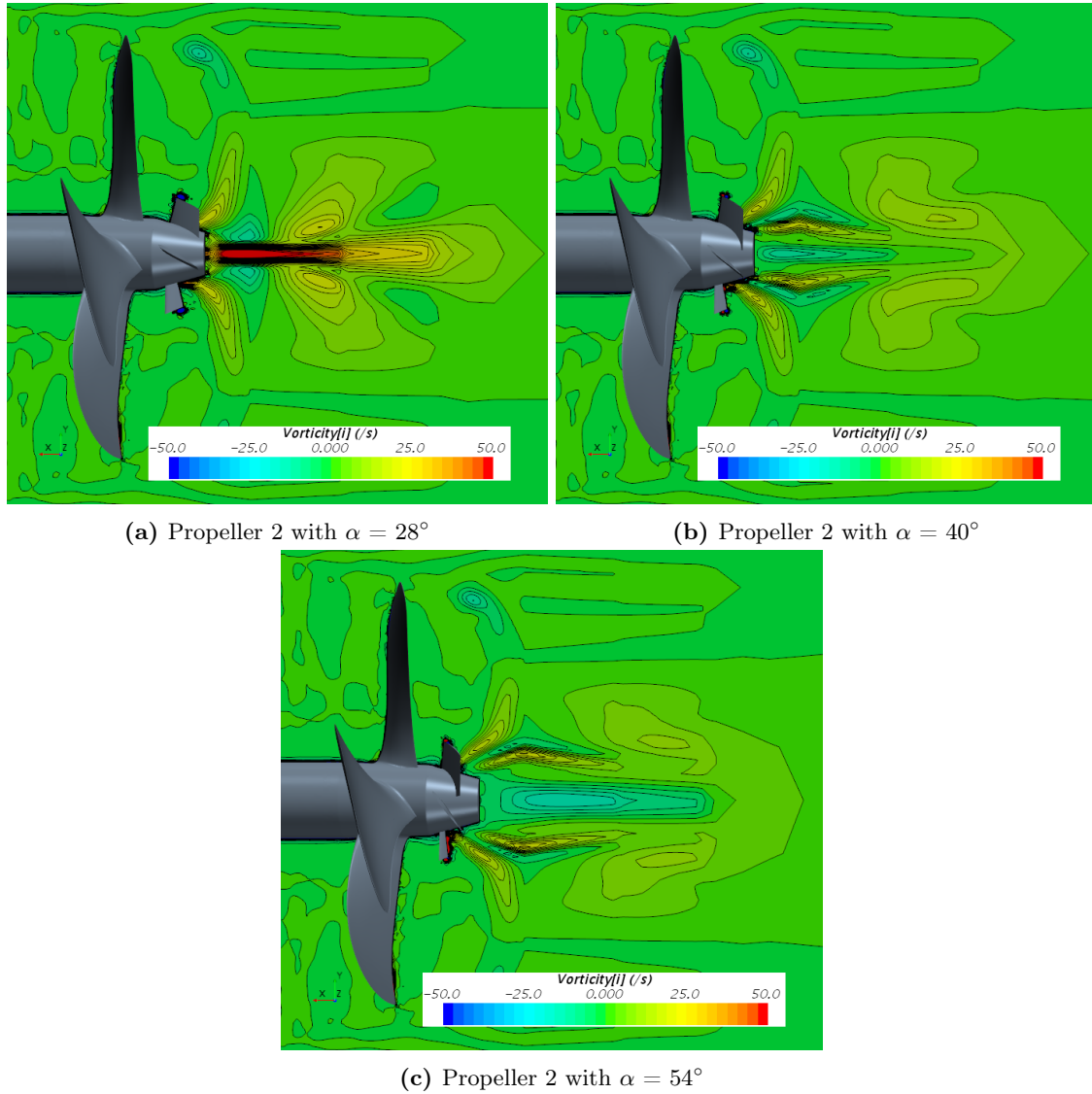
Figure 5.9: The influence of the pitch angle α on the vorticity (x-component), which shows that the reduction of the hub vortex increases when α is larger

The rotational losses start to increase when $\alpha > 70°$, which can be caused by the large angle of attack (AOA). The AOA is the angle between the chord line of the fin and the inflow. This inflow differs for every propeller, considering that different geometries cause different flows behind the propeller. Consequently, the angle at which the rotational losses start to increase may differ for different propellers. At large AOA, the flow around the fin can no longer conform over the surface of the fin leading to separation as shown in Figure 5.10. Separation creates turbulence in the wake of the fin and increases the drag, which explains why the rotational losses increase after $\alpha > 70°$.

The additional axial losses increase when $\alpha > 25°$. A larger volume of water is transported by the fins at larger angles. Energy is lost in this process and due to this the additional axial losses increase.

In conclusion, the pitch angle α has a large influence on the efficiency. The optimal pitch angle of the fins is approximately 40 degrees, but ultimately depends on the angle of attack of the fins, which is different for different propellers. Therefore the optimal pitch angle depends on the propeller.

Radius of the PBCF (R_{fin})

The second parameter that is varied is the outer radius of the PBCF. In previous studies it has been suggested that the radius has a big influence on the efficiency [1] [23] [24]. It has been claimed that the optimal radius of the PBCF should be between 20 and 25% of the radius of the propeller [48]. In this section the influence of the radius of the PBCF on the efficiency and energy losses will be investigated. The radius will be varied from 0.2 to 0.5 times the radius of the propeller. Lower radii are not possible,
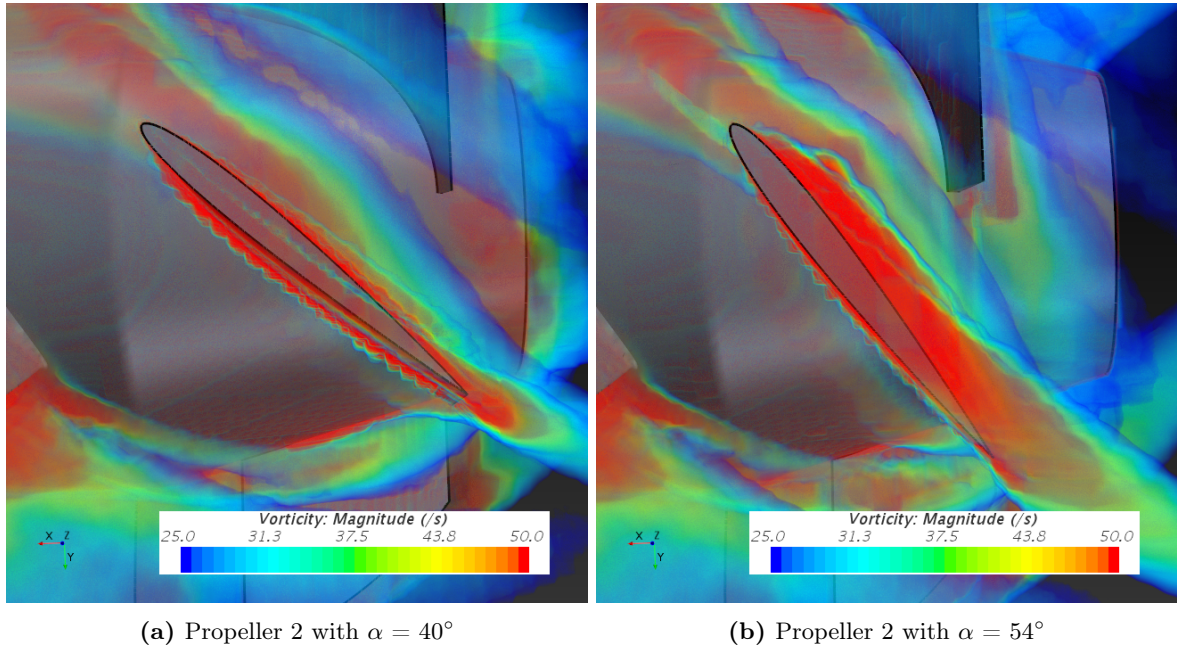
(a) Propeller 2 with $\alpha = 40°$ **(b)** Propeller 2 with $\alpha = 54°$

Figure 5.10: The vorticity (magnitude) around a fin in the x, y-plane, showing separation at large α

(a)

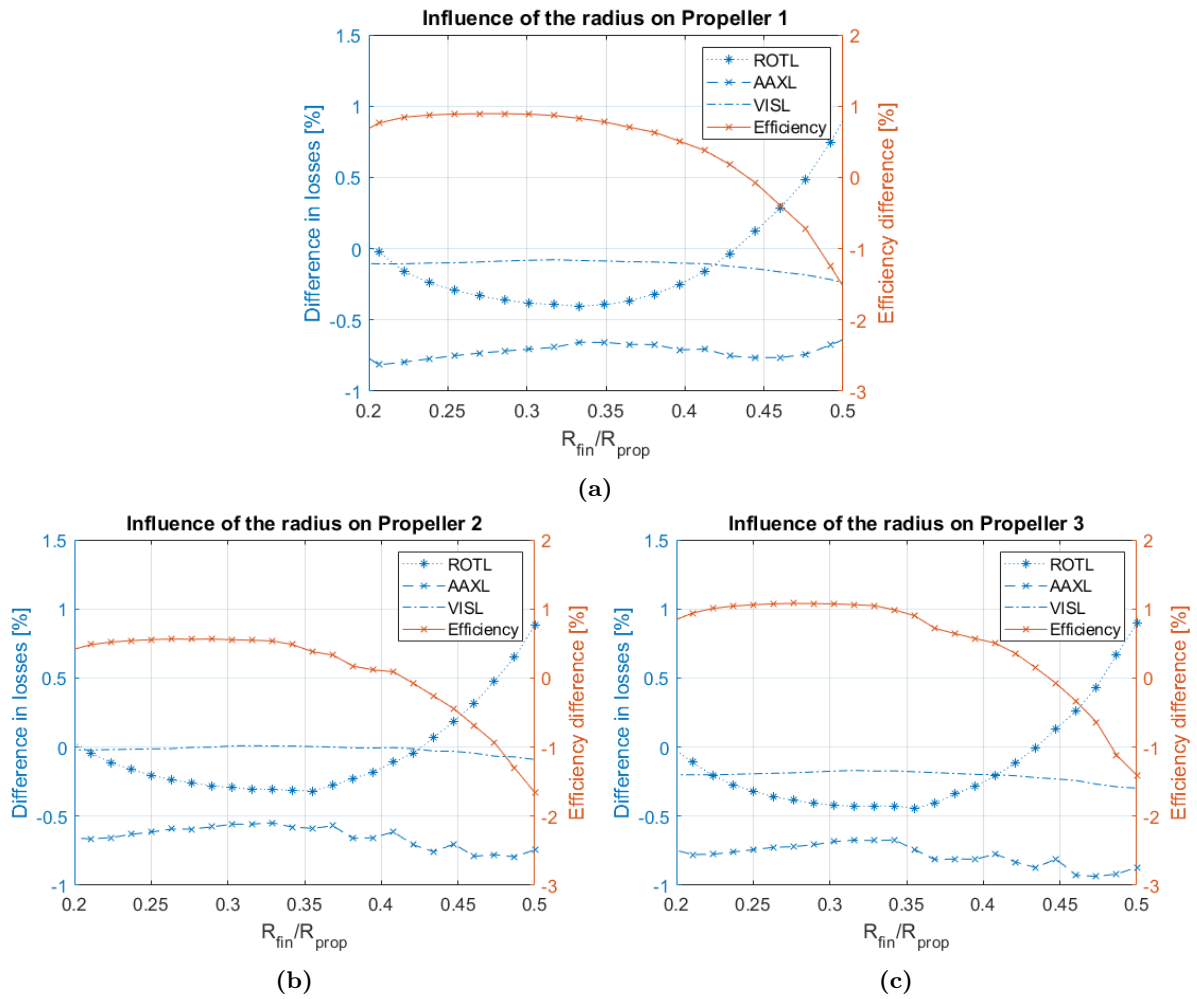**(b)**   **(c)**

Figure 5.11: The influence of the radius of the PBCF R_{fin} on the efficiency and energy losses for (a) Propeller 1, (b) Propeller 2 and (c) Propeller 3

because the hubcap has a radius larger than this. The results of the parametric studies are shown in Figure 5.11.

These graphs show that the radius has an influence on the efficiency. When $0.25 < R_{fin}/R_{prop} < 0.32$, the efficiency is not significantly affected. The efficiency drops fast when $R_{fin}/R_{prop} > 0.32$, which is simultaneous with the increase of rotational losses. Only a small effect on the additional axial losses can be observed. The additional losses increase for larger radii, which can be explained by the same argument as in the previous section. A larger volume of water is transported causing the additional axial losses to increase. When $R_{fin}/R_{prop} < 0.35$ the additional axial losses start to decrease. At this radius, the additional thrust that is generated by the fins overcomes the additional losses caused by the transport of water.

To further investigate why the rotational losses increase when $R_{fin}/R_{prop} > 0.32$, we will take a closer look at the vorticity in simulations of Propeller 2 at $R_{fin}/R_{prop} = 0.21$, 0.26 and 0.37. To confirm that the PBCF suppresses the hub vortex, as it is designed to do, the vorticity in the x-direction in the x, y-plane is shown in Figure 5.12. These figures clearly show a reduction of the hub vortex. The hub vortex is less suppressed at $R_{fin}/R_{prop} = 0.21$. The fin is too small to the affect the whole root blade vortex, part of the vortex easily travels over it. This leads to the merging of part of these vortices further away from the hub.

The rotational losses increase when $R_{fin}/R_{prop} > 0.35$. Vorticity is present in the wake of the fins. The wake of the fin with a higher radius is larger, which results in more vorticity and as a result more rotational losses, as shown in Figure 5.13. In this figure more vorticity can also be observed at the tip of the taller fin, leading to more rotational losses as well.

In conclusion, the optimal radius of the PBCF is $0.25 < R_{fin}/R_{prop} < 0.32$. No significant influence of the radius can be measured in this region.
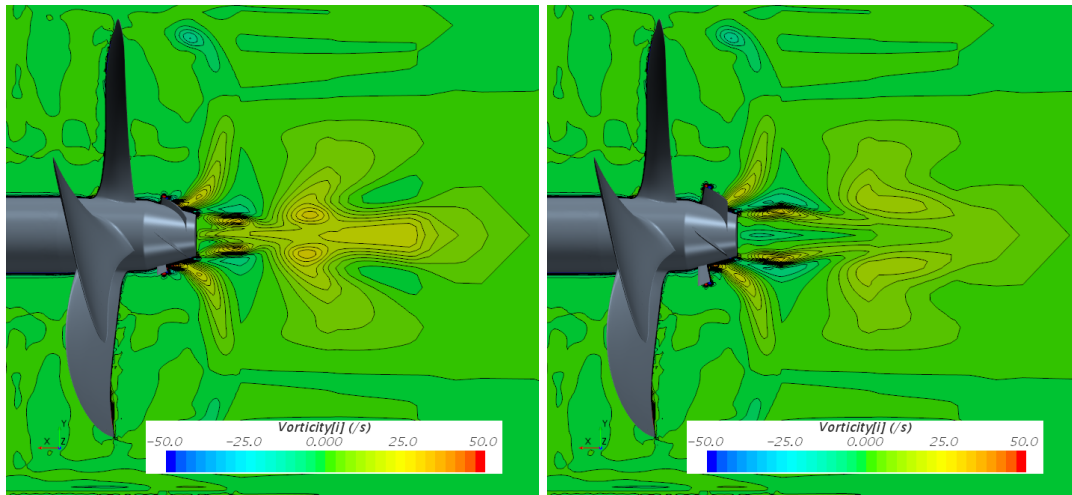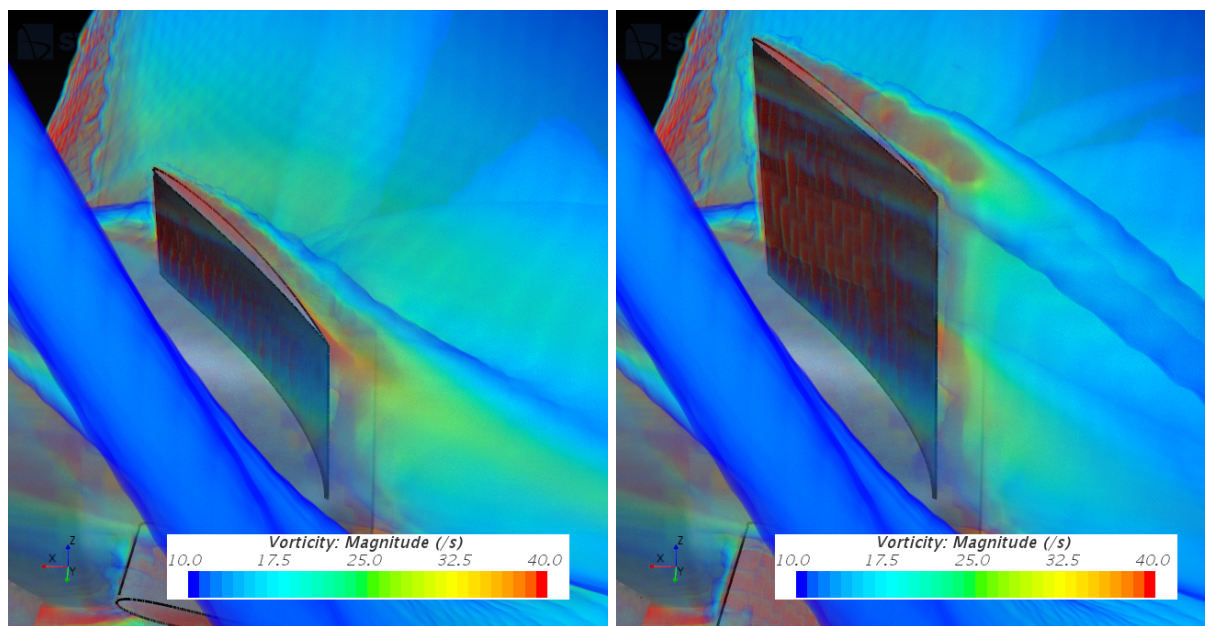

(a) Propeller 2 with $R_{fin}/R_{prop} = 0.21$ **(b)** Propeller 2 with $R_{fin}/R_{prop} = 0.26$
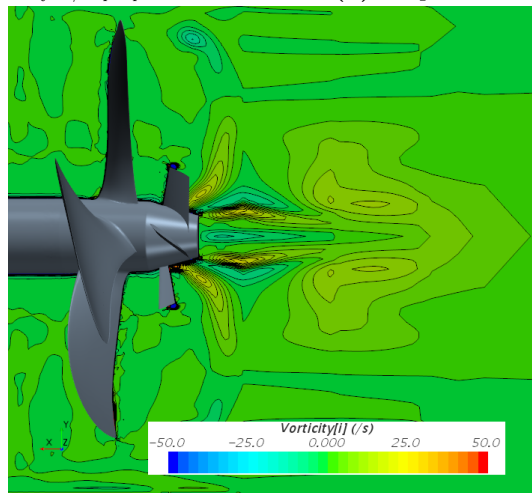
(c) Propeller 2 with $R_{fin}/R_{prop} = 0.37$

Figure 5.12: The vorticity (x-component) in the x, y-plane for different settings of R_{fin}/R_{prop}

(a) $R_{fin}/R_{prop} = 0.26$

(b) $R_{fin}/R_{prop} = 0.37$

Figure 5.13: Vorticity (magnitude) around a fin of the PBCF of Propeller 2
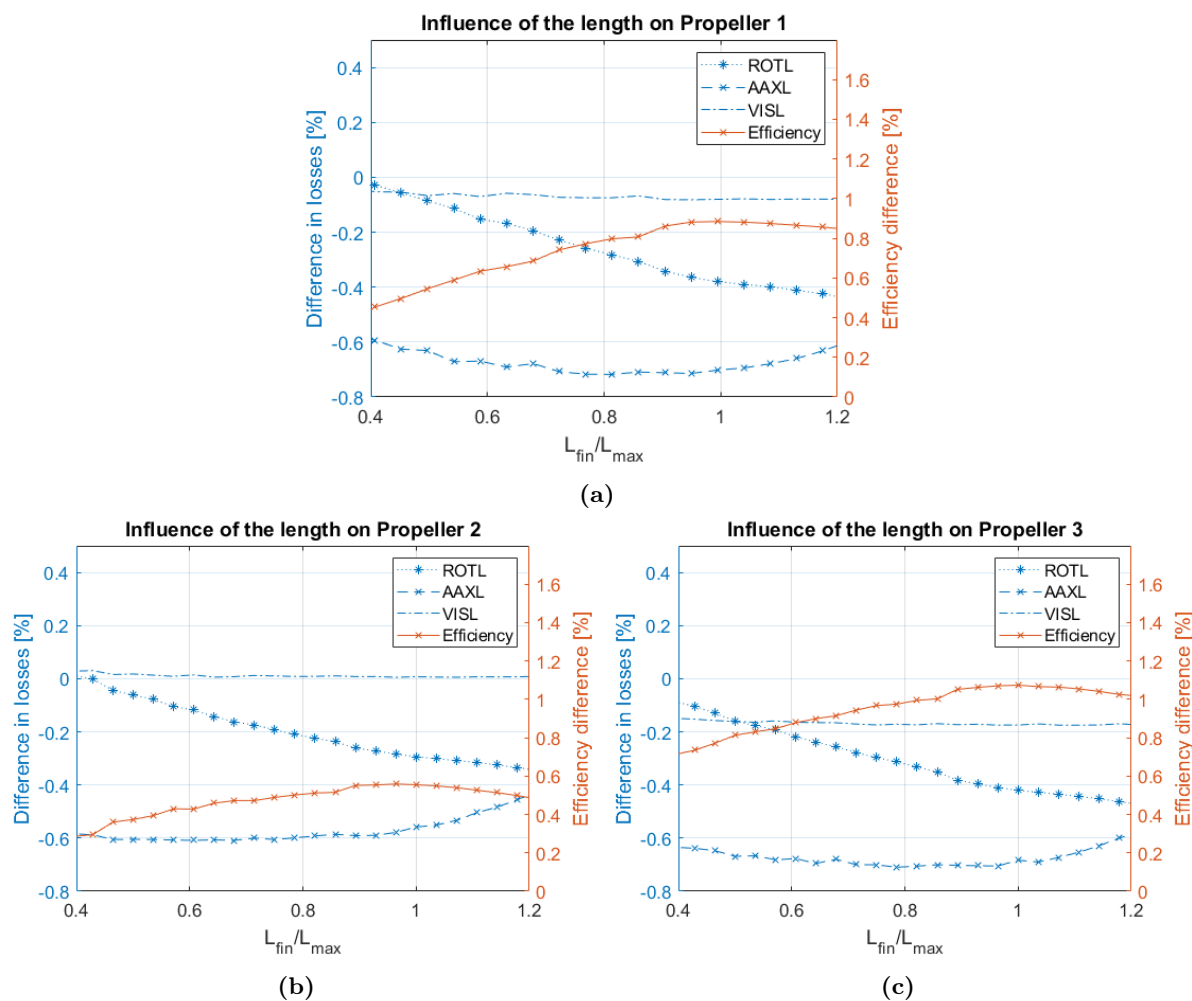

(a)

(b)

(c)

Figure 5.14: The influence of the length of the fins of the PBCF L_{fin} on the efficiency and energy losses for (a) Propeller 1, (b) Propeller 2 and (c) Propeller 3

Length of the fins (L_{fin})

The third parameter that is varied is the length of the fins on the PBCF. From previous parametric studies it can be assumed that the diameter and length ratio is an important factor [1] [23] [24]. In this section the influence of the length of the fins on the efficiency and energy losses will be investigated. The length will be varied from 0.4 to 1.25 times L_{max}, which is the maximum length of the fins at $\alpha = 0°$ as defined in Figure 5.7a. The results of the parametric studies are shown in Figure 5.14.

The graphs show that the length has an influence on the efficiency and energy losses. The efficiency increases until a $L_{fin}/L_{max} = 1$, hereafter the efficiency slowly decreases. The rotational losses decrease when L_{fin} is increased, while the additional axial losses increase when $L_{fin}/L_{max} > 1$. To further investigate these effects, we will simulate Propeller 2 with a PBCF with $L_{fin}/L_{max} = 0.43$, 1.0 and 1.21. To investigate if the PBCF suppresses the hub vortex at these settings, the vorticity in the x-direction in the x,y-plane is presented in Figure 5.15. In the figure on the top left, $L_{fin}/L_{max} = 0.43$, we can clearly observe a hub vortex in the wake of the propeller, although smaller and less strong than the original hub vortex. In the other two figures the hub vortex can not be observed. The root blade vortices can more easily flow around smaller fins. As a result, the root blade vortices are less affected by the PBCF and still merge together after the hubcap. Therefore, the fins should be long enough to keep the vortices from merging after the hubcap.

The hub vortex is reduced more when L_{fin} is larger, leading to a reduction of rotational losses. The additional axial losses increase when $L_{fin}/L_{max} > 1$. The same argument as in the previous sections can be used to explain this. The area of the fins increase, causing the volume of water that is transported to increase as well. Axial energy is lost in this process, resulting in an increase in additional axial losses.

In conclusion, L_{fin} has an influence on the efficiency of the propeller. The optimal length of the fin is approximately L_{max}.


(a) $L_{fin}/L_{max} = 0.43$

(b) $L_{fin}/L_{max} = 1.0$

(c) $L_{fin}/L_{max} = 1.21$
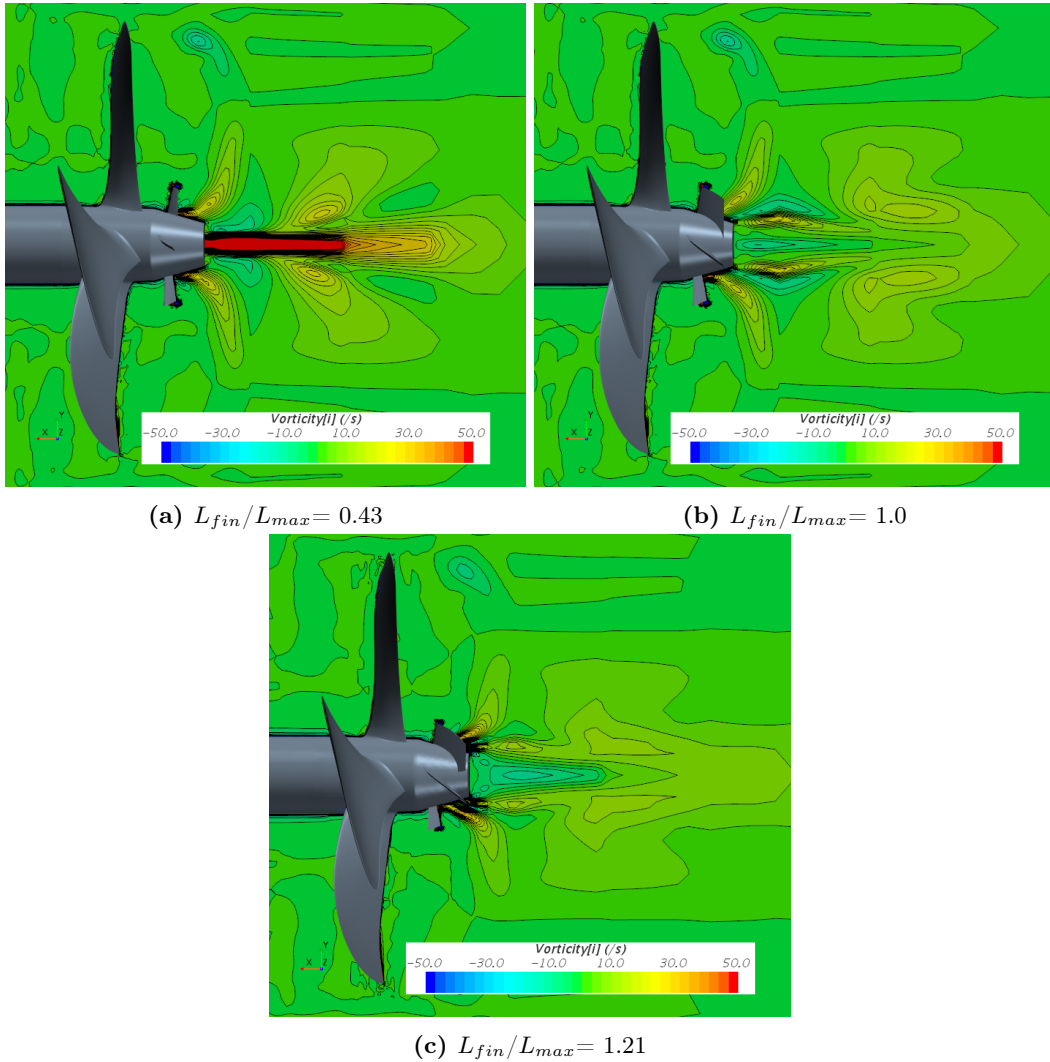
Figure 5.15: The vorticity (x-component) in the x,y-plane for different settings of L_{fin}/L_{max}
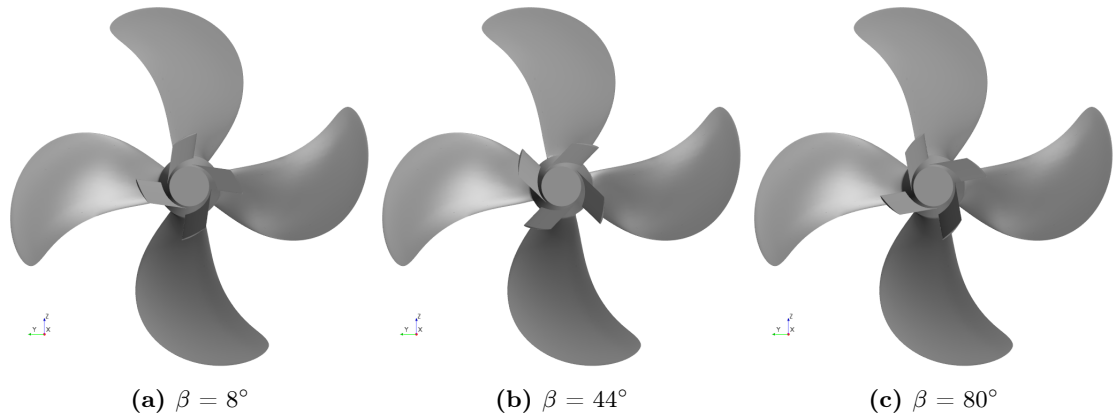
Phase shift angle (β)

The last parameter that is varied is the phase shift angle β. The phase shift angle is an interesting parameter of the PBCF. Some contradictory statements have been made about the positioning of the PBCF in previous studies. One study claims that the trailing edge of the propeller and the leading edge of the PBCF should be such that the PBCF is placed in the middle of the blades passages [48]. Different studies claim that the phase shift angle has no influence on the efficiency gain [1] [23]. In this section the influence of the phase shift angle of the PBCF on the efficiency and energy losses will be investigated. The PBCF is rotated over 72 degrees for Propeller 1 and 90 degrees for Propeller 2 and 3, due to symmetry. The PBCF is rotated with steps of 2 degrees. In our design of the PBCF the front of the first fin, at $\beta = 0$, is positioned at $(x, y) = (0, 0)$. Due to this, the phase shift angle is not directly related to the blades of the propellers. As a consequence of this, a difference in the results of the parameteric study, as presented in Figure 5.16, is expected.

Almost no influence on the efficiency can be observed in these graphs. The effects on the rotational and additional axial losses are larger. These two losses seem to balance each other, when the rotational losses increase, the additional axial losses decrease. To further investigate this effect, simulations of Propeller 2 with $\beta = 8°$, 44° and 80° are performed. The position of the fins of these PBCFs in relation to the propeller blades are shown in Figure 5.17. To investigate if the PBCF suppresses the hub vortex for all three β the vorticity in the x-direction in the x, y-plane for all three the settings is shown in Figure 5.18.

It can be observed that the hub vortex is suppressed for all β, while the rotational losses of the PBCF with $\beta = 44°$ are higher. The fins of the PBCF with $\beta = 44°$ are placed in the wake of the propeller blades, where the root blade vortices are generated. Initially vorticity is created around the fins of the PBCF, as shown in Figure 5.10a. The root blade vortices passing the fins are strengthened by the vorticity around
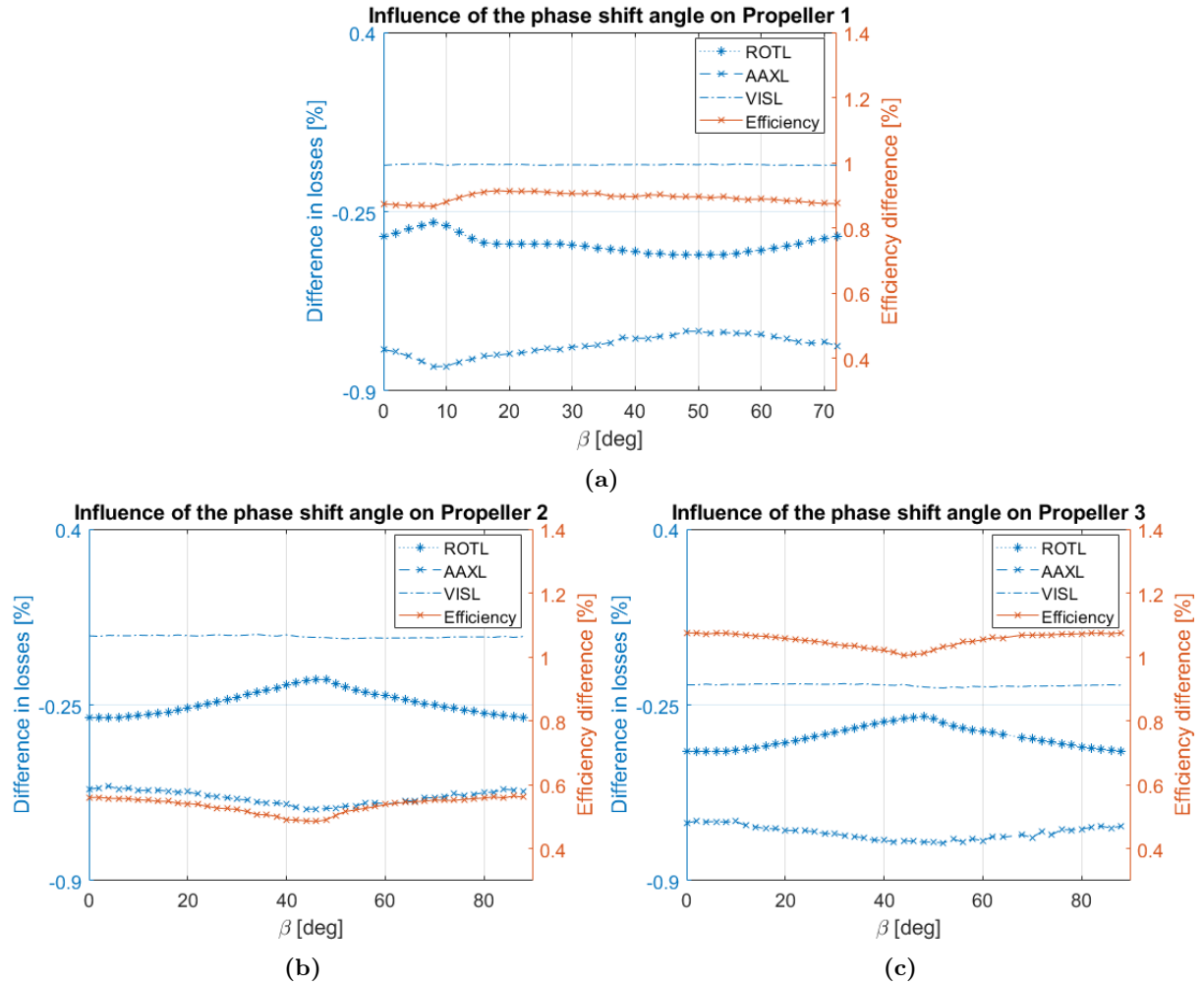
Figure 5.16: The influence of the phase shift angle β on the efficiency and energy losses for (a) Propeller 1, (b) Propeller 2 and (c) Propeller 3

(a) $\beta = 8°$ **(b)** $\beta = 44°$ **(c)** $\beta = 80°$

Figure 5.17: The different settings of the phase shift angle β on Propeller 2 used in the quasi-steady $k - \omega$ simulations

(a) Propeller 2 with $\beta = 8°$ **(b)** Propeller 2 with $\beta = 44°$

(c) Propeller 2 with $\beta = 80°$
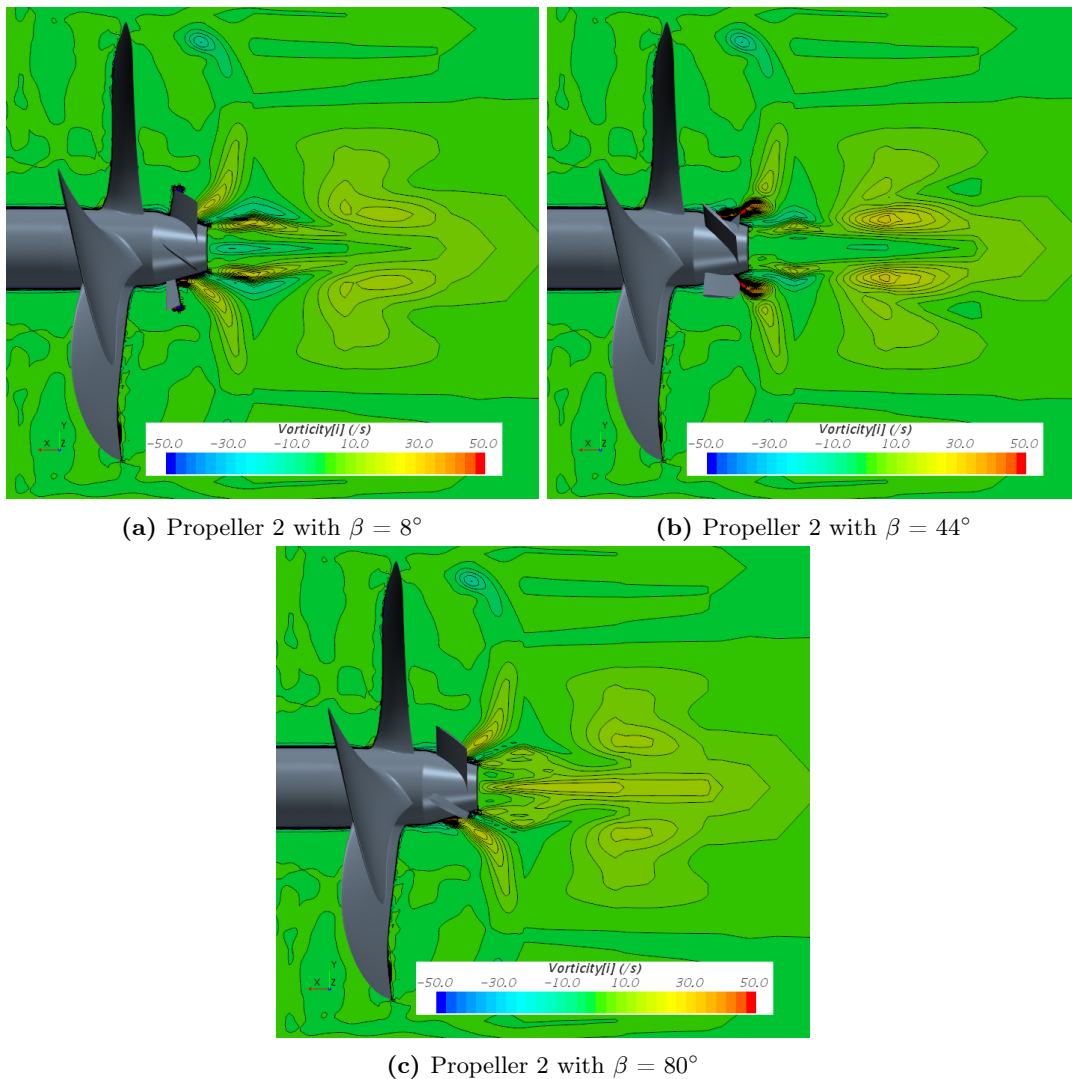
Figure 5.18: The vorticity (x-component) in the x, y-plane for different settings of β

the fins, resulting in stronger vortices, as shown in Figure 5.19. No interaction between the vorticity around the fins and the root blade vortices of the PBCFs with $\beta = 8°$ and $80°$ is possible, leading to less rotational losses compared to $\beta = 44°$.

This also gives an explanation why the additional axial losses are reduced when the rotational losses are increased. The flow passes the fin, creating additional vorticity around the fin. When the root blade vortices pass the fin, the stream passing the fin already contains vorticity. As a result of this, no additional

(a) Propeller 2 with $\beta = 8°$

(b) Propeller 2 with $\beta = 44°$

(c) Propeller 2 with $\beta = 80°$
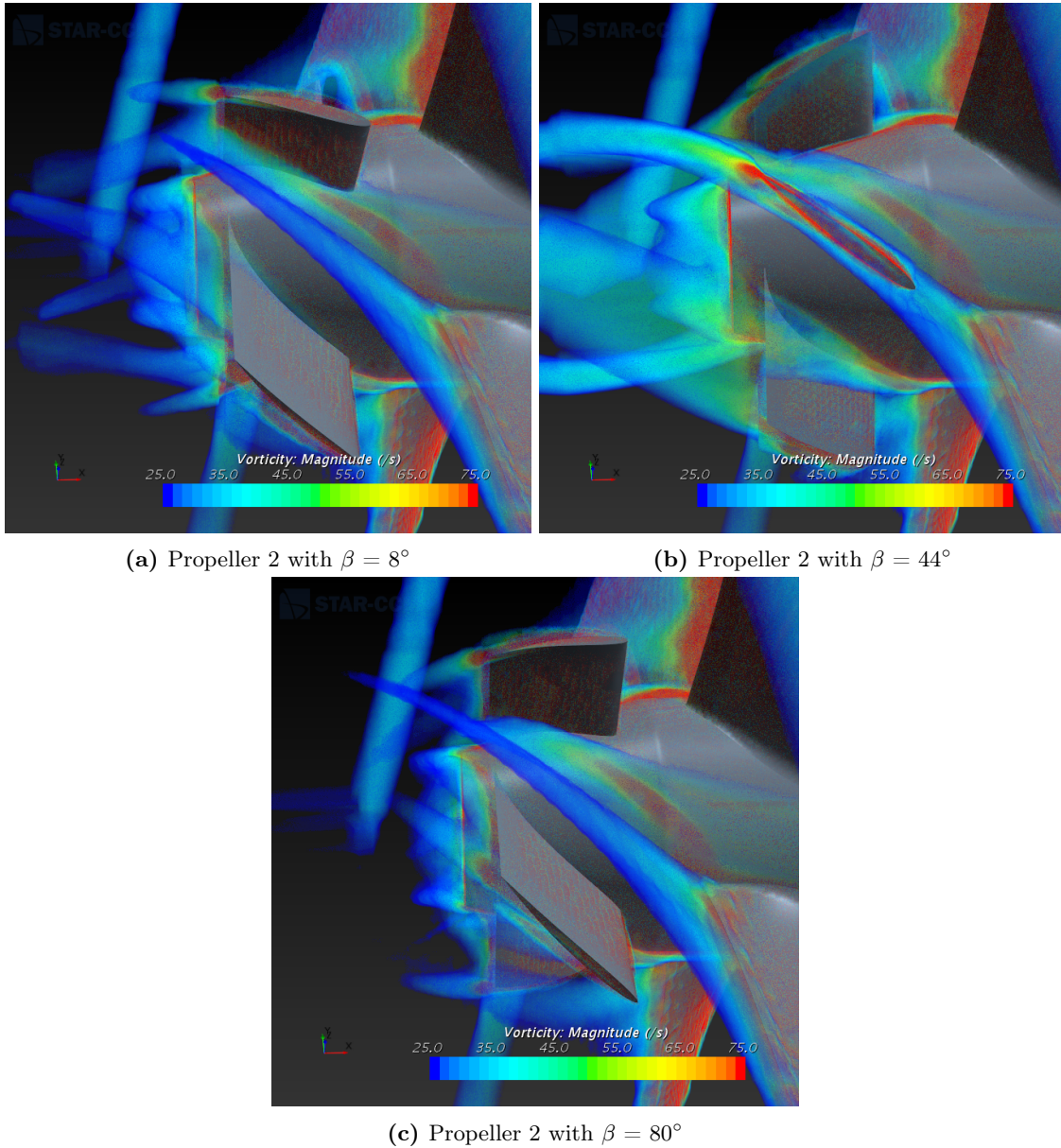
Figure 5.19: The vorticity (magnitude) around the fins of Propeller 2 with 3 different settings of β

axial energy is lost. In the simulations with $\beta = 8°$ and $80°$, the root blade vortices do not interact with the fins, while the fins still generate vorticity. The axial flow approaching the fin is converted in a rotating flow, resulting in additional axial losses. As a consequence, the additional axial losses are higher when the rotational losses are lower due to the positioning of the fins.

In conclusion, the phase shift angle β does not have a significant influence on the efficiency enhancement by the PBCF. The rotational and additional axial losses are slightly influenced by the phase shift angle, due to the positioning of the fins related to the propeller blades.

Effect of the parameters on the efficiency

The influence of the parameters on the efficiency and energy losses has been investigated separately. It was shown that the enhancement of the efficiency is affected by the geometry of the PBCF. In this section we will compare the effects of the parameters on the efficiency to analyze which parameter is most important. The comparison of these parameters boss Propeller 3 is presented in Figure 5.20. The parameters are scaled on their minimum and maximum values in the parametric study, as presented in Table 5.5.

The graph clearly shows that the influence of the phase shift angle β is almost insignificant, as was concluded in the previous section. This yields that β does not have to be optimized for every propeller.

Table 5.5: Minimum and maximum values of the varied parameters

	Minimum	Maximum
α [°]	0	90
R_{fin}/R_{prop}	0.2	0.5
L_{fin}/L_{max}	0.4	1.2
β [°]	0	72 or 90
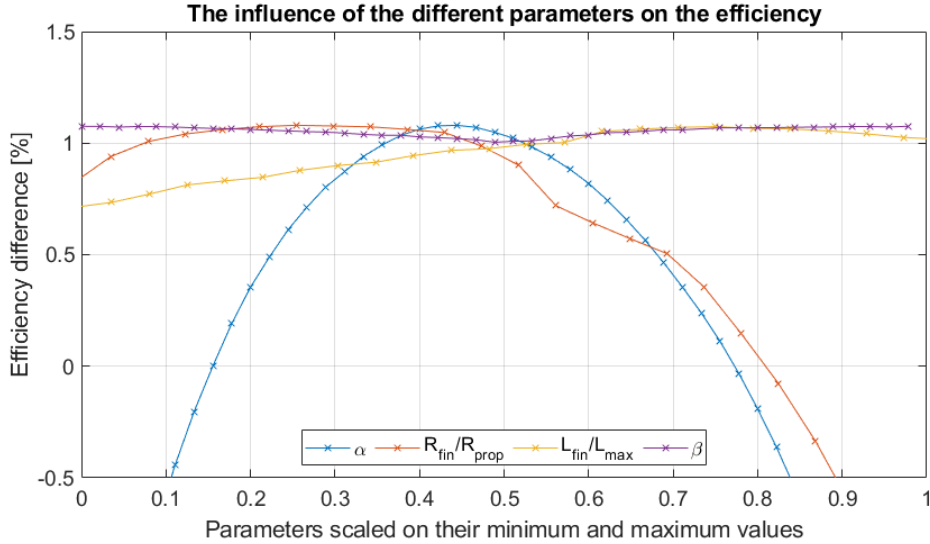
Figure 5.20: The influence of the parameters on the efficiency for Propeller 3, where the parameters are scaled on their minimum and maximum values in the parametric study

The length of the fins L_{fin} has a larger influence on the efficiency than β. The efficiency increases with increasing length. When $L_{fin}/L_{max} > 0.9$, only small effects on the efficiency can be noticed. Therefore, it is less important to optimize the length of the fins when a sufficiently large fin is chosen.

The outer radius R_{fin} only has a big influence on the efficiency when the radius is too large. When $0.25 < R_{fin}/R_{prop} < 0.32$, the influence is insignificantly small. Therefore the radius does not have to be optimized either when designing a PBCF. Choosing a radius within $0.25 < R_{fin}/R_{prop} < 0.32$ should result in the most efficient radius.

The pitch angle α has the biggest influence on the efficiency. This curve clearly has a optimum. When a different pitch angle is chosen, this has a big influence on the efficiency. A general optimum of α cannot be defined, since we assumed that it is affected by the angle of attack which is different for different propellers. Consequently, the pitch angle α is the most important parameter to optimize when designing a PBCF for a propeller.

5.5 Recap

In this chapter we used the control volume method to investigate the effects of the PBCF. First the different PBCF were presented and their effects on the open water characteristics were calculated. In the open water characteristics it was shown that the PBCF increases the efficiency in the complete operating regime.

Next the effects of the PBCF on the energy losses were investigated. It was shown that the PBCF suppresses the hub vortex and because of this reduces the rotational losses.

Additionally, the energy losses were investigated using multiple control volumes to evaluate the effect of the PBCF in different regions. The multiple control volume configuration showed that the rotational losses are only reduced close to the hub. Thus the percentage of rotational losses close to the hub can provide a good indication whether a PBCF can sufficiently enhance the efficiency of a propeller. If the percentage of rotational losses close to the hub is higher, the possible efficiency enhancement is higher.

Finally, the control volume method was used in a parametric study to optimize the design of the

PBCF. Four different parameters were varied: the pitch angle α, the outer radius of the PBCF R_{fin}, the length of the fins L_{fin} and the phase shift angle β.

The optimal pitch angle of the fins is approximately 40 degrees, but ultimately depends on the angle of attack of the fins. The optimal radius of the PBCF is $0.25 < R_{fin}/R_{prop} < 0.32$. The optimal length of the fin is approximately L_{max}. The phase shift angle does not have a significant influence on the efficiency enhancement by the PBCF.

After using the methods to analyse the energy losses for a propeller with a PBCF, it can be concluded that the control volume method can be a helpful tool to investigate whether an Energy Saving Device can significantly enhance the efficiency of a propeller.

6 | Conclusion

The goal of this study was to analyse the energy losses of a propeller using the control volume method and to improve this method by using multiple control volumes. After this, the control volume method was used to investigate the effects of the PBCF and to evaluate when a PBCF can sufficiently increase the efficiency of the propeller.

First, we compared the results of the simulations of our propellers to the results of a previous study using the control volume method. The simulations were performed using the SST $k - \omega$ model with the Sliding Mesh (SM) method to simulate the rotation. As a result, we assumed that the control volume method can be used to measure the energy losses in transient $k - \omega$ simulations.

Hereafter, the same propellers were analysed using the $k - \epsilon$ method with the Moving Reference Frame (MRF) method to simulate the rotation. These results were compared to the results of the transient $k - \omega$ simulations. From this comparison, it could be assumed that the quasi-steady Standard $k - \epsilon$ simulations can be used to give a general indication of the large scale energy losses. Similar differences between the two simulations were observed for Propeller 2 and 3. Because of this, it is assumed that this method can be useful to analyse propellers with similar geometries, considering that the relative difference between the losses is more important when comparing the propellers than the exact values of the energy losses. The viscous losses cannot be calculated with this method.

Next two different configurations with multiple control volumes were investigated. These simulations confirmed that the choice of control volume affects the results. Therefore it is important to use identical control volumes when comparing propellers. Multiple control volumes in one simulation can also be useful to investigate the energy losses at different areas around the propeller.

The introduced methods were used to analyse the effects of the PBCF. The PBCF suppresses the hub vortex and as a result of this reduces the rotational losses. The multiple control volume configuration showed that the rotational losses are only reduced close to the hub. This implies that the percentage of rotational losses close to the hub can provide a good indication whether a PBCF can sufficiently enhance the efficiency of a propeller. If the percentage of rotational losses close the the hub is higher, the possible efficiency enhancement is higher.

Finally, the control volume method was used in a parametric study to optimize the design of the PBCF. Four different parameters were varied: the pitch angle α, the outer radius of the PBCF R_{fin}, the length of the fins L_{fin}, and the phase shift angle β.

The optimal pitch angle of the fins is approximately 40 degrees, but ultimately depends on the angle of attack of the fins. The optimal radius of the PBCF is $0.25 < R_{fin}/R_{prop} < 0.32$. The optimal length of the fin is approximately L_{max}, which is the length of the fin at $\alpha = 0°$. The phase shift angle does not have a significant influence on the efficiency enhancement by the PBCF.

After using the methods to analyse the energy losses for a propeller with a PBCF, it can be concluded that the control volume method can be a helpful tool to investigate whether an Energy Saving Device can significantly enhance the efficiency of a propeller.

Bibliography

[1] Lim, S.S., Kim, T.W., Lee, D.M., Kang, C.G., Kim, S.Y. (2014) Parametric study of propeller boss cap fins for container ships *Int. J. Nav. Archit. Ocean Eng.* **6** 187-205

[2] Peña, B., Ponkratov, D., Fitzsimmons, P., Muk-Pavic, E. (2017) Energy Saving Devices: The State of the Art

[3] Schuiling, B. (2016) The Design and Numerical Demonstrations of a New ESD *16th Numerical Towing Tank Symposium*

[4] Carlton, J. (2007) *Marine propellers and propulsion* Elsevier Ltd, ISBN 978-07506-8150-6

[5] Waterborne, source of innovation `https://www.waterborne.eu/showcases/energy-saving/`

[6] Becker Marine Systems, `https://www.becker-marine-systems.com/products/product-detail/becker-mewis-duct.html`

[7] Ship technology (photo courtesy of Wärtsilä) `https://www.ship-technology.com/uncategorised/newswartsila-to-supply-fixed-pitch-propellers-for-greek-aframax-tankers-4850980/`

[8] Wikipedia, the free encyclopedia `https://nl.wikipedia.org/wiki/Bestand:Grim%27s_Vane_Wheel-03.jpg`

[9] Zondervan, G. (2011) Fuel saving in ship propulsion application and design of pre-swirl stators *The Royal Institution of Naval Architects*

[10] Huang S., Huang Z. (2016) Investigation on Energy-Saving Effectiveness of Pre-Swirl Duct Based on CFD *10th International Conference on Hydrodynamics*

[11] Kawamura, T., Ouchi, K., Takeuchi, S. (2013) Model and full scale CFD analysis of propeller boss cap fins (PBCF) *Third Internation Symposium on Marine Propulsion*

[12] Funeno, I. (2002) On viscous flow around marine propellers *J. Kansai Soc. Nav. Archit. Jpn.* **238** 17-27

[13] Ouchi, K., Ogura, M. (1988) A research and development of PBCF (propeller boss cap fins), improvement of flow from propeller boss *J. Soc. Nav. Archit.* **163** 66-78

[14] Nojiri, T., Ishii, N., Kai, H. (2011) Energy saving technology of PBCF (propeller boss cap fins) and its evolution *International propulsion symposium, Japan Institute of Marine Engineering*

[15] Hansen, H. R., Dinham-Peren, T., Nojiri, T. (2011) Model and Full Scale Evaluation of a 'Propeller Boss Cap Fins' Device Fitted to an Aframax Tanker *Second International Symposium on Marine Propulsors*

[16] International Towing Tank Conference (2014) 27th Propulsion Committee Proceedings

[17] Wärtsilä Ship Design for Aframax `https://edisciplinas.usp.br/mod/resource/view.php?id=1636673`

[18] Wärtsilä EnergoProFin calculator `https://www.wartsila.com/services-catalogue/propulsion-services/energoprofin/calculator`

[19] GloMEEP, Global maritime energy efficiency partnership `https://glomeep.imo.org/technology/propulsion-improving-devices-pids/`

[20] Mizzi, K., Demirel, Y. K., Banks, C., Turan, O., Kaklis, P., Atlar, M. (2017) Design optimisation of Propeller Boss Cap Fins for enhanced propeller performance *Applied Ocean Research* **62** 210-222

[21] MOL Techno-Trade `http://www.pbcf.jp/english/faq/index.html#t6_01`

[22] Sonistics `https://www.sonistics.com/2014/04/underwater-pbcf-installations-bring-immediate-fuel-savings/`

[23] Seo, J., Lee, S.J., Han, B., Rhee, S.H. (2016) Influence of Design Parameter Variations for Propeller-Boss-Cap-Fins on Hub Vortex Reduction *Journal of Ship Research* **60 (4)** 203-218

[24] Gaggero, S. (2018) Design of PBCF energy saving devices using optimization strategies: A step towards a complete viscous design approach *Ocean Engineering* **159** 517-538

[25] Lockley, P., Jarabo-Martin, A. (2011) *Ship Efficiency: The guide* Fanthom, ISBN 978-0956825902

[26] Dyne, G. (1995) The Principles of Propulsion Optimization *The Royal Institution of Naval Architects*

[27] Schuiling, B., van Terwisga, T. (2016) Energy analysis of a propeller in open water using a RANS method *24th International HISWA Symposium on Yacht Design and Yacht Construction* ISBN 978-94-6186-749-0

[28] Rankine, W.J.M. (1865) On the Mechanical Principles of the Action of Propellers *Institution of Naval Architects* **6**, 13-39

[29] Wikipedia, the free encyclopedia, "Momentum theory" `https://en.wikipedia.org/wiki/Momentum_theory`

[30] Dyne, G. (1993) On the efficiency of a propeller in uniform flow *The Royal Institution of Naval Architects*

[31] van Terwisga, T. (2013) On the working principles of Energy Saving Devices *Third International Symposium on Marine Propulsors*

[32] Fox, R.W, McDonald A.T. (2011) *Introduction to Fluid Mechanics* John Wiley & Sons, Inc., ISBN 0470547553

[33] Rijpkema, D.R. (2008) Numerical Simulations of Single-Phase and Multi-Phase Flow over a NACA 0015 Hydrofoil *Master of Science Thesis, Delft University of Technology*

[34] Aris, R. (1962) *Vectors, Tensors, and the Basic Equations of Fluid Mechanics* Dover Publications, Inc., ISBN 0-486-66110-5

[35] Wikiversity, "Fluid Mechanics for Mechanical Engineers/Differential Analysis of Fluid Flow `https://en.wikiversity.org/wiki/Fluid_Mechanics_for_Mechanical_Engineers/Differential_Analysis_of_Fluid_Flow`

[36] Weltym J.R., Wicks, C.E., Wilson, R.E., Rorrer, G.L. (2008) *Fundamentals of Momentum, Heat, and Mass Transfer* John Wiley & Sons, Inc., ISBN 978-0470128688

[37] Versteeg, H.K., Malalasekera, W. (1995) *An introduction to Computational Fluid Dynamics* Longman Group Ltd, ISBN 0-582-21884-5

[38] Batchelor, G.K. (2000) *An Introduction to Fluid Dynamics* Cambridge University Press, ISBN 0-521-66396-2

[39] Andersson, J., Eslamdoost, A., Capitao Patrao, A., Hyensjö, M., Bensow, R.E. (2018) Energy balance analysis of a propeller in open water *Ocean Engineering* **158**, 162-170

[40] Carter, A.H. (1999) *Classical and Statistical Thermodynamics* Pearson Education, ISBN 9780137792085

[41] Andersson, J. (2018) Using Energy Fluxes to Analyze the Hydrodynamic Performance of Marine Propulsion Systems *Thesis for the degree of licentiate of engineering in thermo and fluid dynamics, Chalmers Universituy of Technology*

[42] Nieuwstadt, F.T.M. (2016) *Turbulentie* Epsilon Uitgaven, ISBN 978-90-5041-028-1

[43] Wilcox, D.C. (2006) *Turbulence Modeling for CFD* DCW Industries, Inc., ISBN 978-1-928729-08-2

[44] COMSOL Multiphysics
`https://www.comsol.com/blogs/which-turbulence-model-should-choose-cfd-application/`

[45] Eça, L., Saraiva, G., Vaz, G., Abreu, H. (2015) The pros and cons of wall functions *ASME 34rd International Conference on Ocean, Offshore and Arctic Engineering*

[46] Menter, F.R. (1994) Two Equation Eddy-Viscosity Turbulence Models for Engineering Applications *AIAA Journal* **32** 1598-1605

[47] Atlar, M., Patience, G. (1998) An investigation into effective boss cap designs to eliminate propeller hub vortex cavitation. *7th International Symposium on Practical Designs of Ship and Mobile Units*

[48] Hsin, C.Y., Lin, B.H., Lin, C.C. (2009) The optimum design of a propeller energy-saving device by computational fluid dynamics *Computational Fluid Dynamics 2008* 655-660

A | Reynolds averaged equations

Using the Reynolds decomposition, the Reynolds averaged equations can be derived. This can be done by used the following 6 rules,

1. $\overline{a\mathbf{u}} = a\overline{\mathbf{u}}$,
2. $\overline{\mathbf{u} + \mathbf{v}} = \overline{\mathbf{u}} + \overline{\mathbf{v}}$,
3. $\overline{\frac{\partial \mathbf{u}}{\partial x}} = \frac{\partial \overline{\mathbf{u}}}{\partial x}$,
4. $\overline{\mathbf{u}'} = 0$,
5. $\overline{\overline{\mathbf{u}}} = \overline{\mathbf{u}}$,
6. $\overline{\overline{\mathbf{u}}\mathbf{v}} = \overline{\mathbf{u}} + \overline{\mathbf{v}}$,

where a is a scalar.

Reynolds averaged continuity equation

First, the continuity equation, equation (2.20), will be averaged. The continuity equation can be written in tensor notation as

$$\frac{\partial u_i}{\partial x_i} = 0. \tag{A.1}$$

By substituting the Reynolds decomposition $\overline{u_i} + u_i'$ into the equation, the following equation is formed,

$$\frac{\partial(\overline{u_i} + u_i')}{\partial x_i} = 0. \tag{A.2}$$

After averaging this equation and applying the rules of Reynolds decompositions, the Reynolds averaged continuity equation is derived. This equation is given by

$$\frac{\partial \overline{u_i}}{\partial x_i} = 0. \tag{A.3}$$

Because of this, it can also be concluded that

$$\frac{\partial u_i'}{\partial x_i} = 0. \tag{A.4}$$

Reynolds-Averaged Navier-Stokes equations

The Navier-Stokes equations can also be Reynolds averaged. The Navier-Stokes equations in tensor notation can be written by

$$\frac{\partial u_i}{\partial t} + u_j \frac{\partial u_i}{\partial x_j} = -\frac{1}{\rho}\frac{\partial p}{\partial x_i} + \nu \frac{\partial^2 u_i}{\partial x_j \partial x_j} + f_i. \tag{A.5}$$

After substituting the Reynolds decompositions for u_i, u_j, p and f_i and using

$$u_j \frac{\partial u_i}{\partial x_j} = \frac{\partial u_i u_j}{\partial x_j} - u_i \frac{\partial u_j}{\partial x_j} = \frac{\partial u_i u_j}{\partial x_j} \tag{A.6}$$

due to the continuity equation, equation (A.5) can be rewritten to

$$\frac{\partial(\overline{u_i} + u_i')}{\partial t} + \frac{\partial((\overline{u_i} + u_i')(\overline{u_j} + u_j'))}{\partial x_j} = -\frac{1}{\rho}\frac{\partial(\overline{p} + p')}{\partial x_i} + \nu \frac{\partial^2(\overline{u_i} + u_i')}{\partial x_j \partial x_j} + (\overline{f_i} + f_i'). \tag{A.7}$$

After averaging this equation and using the rules for Reynolds averaging, the previous derived equations and the chain rules for derivation, this equation can be rewritten to the Reynolds-Averaged Navier-Stokes equations, which are given by

$$\frac{\partial \overline{u_i}}{\partial t} + \frac{\partial \overline{u_i}\,\overline{u_j}}{\partial x_j} = -\frac{1}{\rho}\frac{\partial \overline{p}}{\partial x_i} + \nu \frac{\partial^2 \overline{u_i}}{\partial x_j \partial x_j} + \overline{f_i} - \frac{\partial \overline{u_i' u_j'}}{\partial x_j} \tag{A.8}$$

where the new term at the far right is called the Reynolds stresses.

B | Navier-Stokes equations for a rotating control volume

Modelling the propeller rotation with the Moving Reference Frame (MRF) does not take into account the movement of the rotating region with respect to the rest of the computational domain. In order to account for this, new terms are added to the Navier-Stokes equations. The derivation of these equations starts at the second law of Newton. The second law of Newton can be rewritten to

$$\mathbf{F} = \frac{\partial m\mathbf{u}}{\partial t} = \int_V \mathbf{a}\rho dV \tag{B.1}$$

where $\mathbf{a}$ is the acceleration. Consider a moving and rotating control volume, with coordinate system xyz. This control volume is located at $\mathbf{R}$ relative to the fixed frame with coordinate system XYZ. Now consider a particle at position $\mathbf{r}$ from the control volume, as can be seen in Figure B.1, with $\mathbf{r} = \hat{i}x + \hat{j}y + \hat{k}z$ in reference to the rotating control volume.
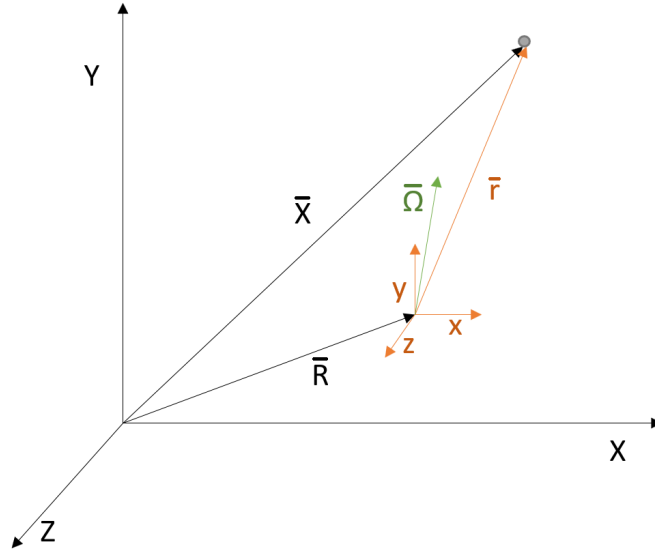
Figure B.1: A schematic overview of a rotating and translating reference system with coordinates xyz inside a fixed frame with coordinates XYZ and its distance to a particle, where the symbols with overbars represent vectors

Relative to the fixed frame this particle is positioned at $\mathbf{X} = \mathbf{R} + \mathbf{r}$. The velocity of this particle, in reference to the fixed framed is

$$\mathbf{u}_{XYZ} = \frac{\partial \mathbf{X}}{\partial t} = \frac{\partial \mathbf{R}}{\partial t} + \frac{\partial \mathbf{r}}{\partial t}, \tag{B.2}$$

The derivative of $\mathbf{R}$ with respect to time can be defined as the velocity at which the control volume is moving, u_{CV}. However both the orientation and the magnitude of $\mathbf{r}$ are functions of time. Therefore

$$\frac{\partial \mathbf{r}}{\partial t} = \frac{\partial (\hat{i}x + \hat{j}y + \hat{k}z)}{\partial t} = \hat{i}\frac{\partial x}{\partial t} + x\frac{\partial \hat{i}}{\partial t} + \hat{j}\frac{\partial y}{\partial t} + y\frac{\partial \hat{j}}{\partial t} + \hat{k}\frac{\partial z}{\partial t} + z\frac{\partial \hat{k}}{\partial t}. \tag{B.3}$$

The velocity of the particle relative to the control volume can be defined as

$$\mathbf{u}_{xyz} = \hat{i}\frac{\partial x}{\partial t} + \hat{j}\frac{\partial y}{\partial t} + \hat{k}\frac{\partial z}{\partial t} \tag{B.4}$$

and

$$\mathbf{\Omega} \times \mathbf{r} = x\frac{\partial \hat{i}}{\partial t} + y\frac{\partial \hat{j}}{\partial t} + z\frac{\partial \hat{k}}{\partial t}, \tag{B.5}$$

where $\mathbf{\Omega} = (\Omega_x, \Omega_y, \Omega_z)$ is the rotation speed of the control volume. Because of this the velocity of the particle relative to the fixed frame can be defined as

$$\mathbf{u}_{XYZ} = \mathbf{u}_{CV} + \mathbf{u}_{xyz} + \mathbf{\Omega} \times \mathbf{r}. \tag{B.6}$$

This gives an acceleration relative to the fixed frame of

$$\mathbf{a}_{XYZ} = \frac{\partial \mathbf{u}_{CV}}{\partial t} + \frac{\partial \mathbf{u}_{xyz}}{\partial t} + \frac{\partial (\mathbf{\Omega} \times \mathbf{r})}{\partial t}. \tag{B.7}$$

The derivative of $\mathbf{u}_{CV}$ with respect of time can be defined as the accelation of the control volume, $\mathbf{a}_{CV}$. Similar to the derivation for the velocity, it can be shown that

$$\frac{\partial \mathbf{u}_{xyz}}{\partial t} = \mathbf{a}_{xyz} + \mathbf{\Omega} \times \mathbf{u}_{xyz} \tag{B.8}$$

and

$$\frac{\partial (\mathbf{\Omega} \times \mathbf{r})}{\partial t} = \frac{\partial \mathbf{\Omega}}{\partial t} \times \mathbf{r} + \mathbf{\Omega} \times \frac{\partial \mathbf{r}}{\partial t} = \frac{\partial \mathbf{\Omega}}{\partial t} \times \mathbf{r} + \mathbf{\Omega} \times (\mathbf{\Omega} \times \mathbf{r}). \tag{B.9}$$

Substituting these two equations gives an acceleration of

$$\mathbf{a}_{XYZ} = \mathbf{a}_{CV} + \mathbf{a}_{xyz} + 2(\mathbf{\Omega} \times \mathbf{u}_{xyz}) + \frac{\partial \mathbf{\Omega}}{\partial t} \times \mathbf{r} + \mathbf{\Omega} \times (\mathbf{\Omega} \times \mathbf{r}). \tag{B.10}$$

In the case of the MRF simulation the control volume is rotating at a constant speed and not translating. Therefore the acceleration can be simplified to

$$\mathbf{a}_{XYZ} = \mathbf{a}_{xyz} + 2(\mathbf{\Omega} \times \mathbf{u}_{xyz}) + \mathbf{\Omega} \times (\mathbf{\Omega} \times \mathbf{r}). \tag{B.11}$$

Because of this the force becomes

$$\mathbf{F} = \frac{\partial m\mathbf{u}}{\partial t} + \int_V (2(\mathbf{\Omega} \times \mathbf{u}) + \mathbf{\Omega} \times (\mathbf{\Omega} \times \mathbf{r}))\rho dV. \tag{B.12}$$

Using the same method as described in Section 2.2.2 it can be derived that the Navier-Stokes equation for a simulation with a rotating control volume becomes

$$\frac{\partial \mathbf{u}}{\partial t} + \mathbf{u} \cdot \nabla \mathbf{u} = -\frac{1}{\rho}\nabla p + \nu\nabla^2 \mathbf{u} + \mathbf{f} - 2(\mathbf{\Omega} \times \mathbf{u}) - \mathbf{\Omega} \times (\mathbf{\Omega} \times \mathbf{r}). \tag{B.13}$$

The two extra terms in this equation can be recognized as the Coriolis acceleration and the centrifugal acceleration, respectively.

C | Tables

Energy densities

Table C.1: The different energy losses normalized by the volume fraction

	Propeller 2				Propeller 3			
	IAXL [%]	*AAXL [%]*	*ROTL [%]*	*VISL [%]*	*IAXL [%]*	*AAXL [%]*	*ROTL [%]*	*VISL [%]*
Ring 1	0.060	-0.116	0.148	0.051	0.057	-0.096	0.167	0.052
Ring 2	0.182	-0.004	0.113	0.023	0.174	-0.016	0.097	0.023
Ring 3	0.273	0.174	0.103	0.039	0.253	0.107	0.087	0.042
Ring 4	0.277	0.158	0.004	0.060	0.274	0.167	0.009	0.062
Ring 5	0.046	-0.082	0.041	0.019	0.056	-0.069	0.040	0.025

Torque and thrust on the different components of the propellers

Table C.2: The torque (Q) and thrust (T) on the propeller blades, the hub & hubcap and the total torque and thrust, separated in the pressure and shear components

		Q [pressure]	Q [shear]	Q [total]	T [pressure]	T [shear]	T [total]
Propeller 1	*Propeller*	$7.35 \cdot 10^5$	$6.22 \cdot 10^4$	$7.97 \cdot 10^5$	$8.99 \cdot 10^5$	$-1.06 \cdot 10^4$	$8.88 \cdot 10^5$
	Hub & Hubcap	$-6.78 \cdot 10^{-3}$	$1.78 \cdot 10^2$	$1.78 \cdot 10^2$	$-1.09 \cdot 10^4$	$-5.30 \cdot 10^2$	$-1.14 \cdot 10^4$
	Total	$7.35 \cdot 10^5$	$6.24 \cdot 10^4$	$7.98 \cdot 10^5$	$8.88 \cdot 10^5$	$-1.11 \cdot 10^4$	$8.77 \cdot 10^5$
Propeller 1 (PBCF)	*Propeller*	$7.34 \cdot 10^5$	$6.22 \cdot 10^4$	$7.96 \cdot 10^5$	$8.99 \cdot 10^5$	$-1.06 \cdot 10^4$	$8.88 \cdot 10^5$
	Hub & PBCF	$-3.15 \cdot 10^3$	$2.74 \cdot 10^2$	$-2.88 \cdot 10^3$	$-6.67 \cdot 10^3$	$-6.05 \cdot 10^2$	$-7.28 \cdot 10^3$
	Total	$7.31 \cdot 10^5$	$6.25 \cdot 10^4$	$7.93 \cdot 10^5$	$8.92 \cdot 10^5$	$-1.12 \cdot 10^4$	$8.81 \cdot 10^5$
Propeller 2	*Propeller*	$1.56 \cdot 10^6$	$8.77 \cdot 10^4$	$1.64 \cdot 10^6$	$1.44 \cdot 10^6$	$-1.22 \cdot 10^4$	$1.42 \cdot 10^6$
	Hub & Hubcap	$3.31 \cdot 10^1$	$3.92 \cdot 10^2$	$3.95 \cdot 10^2$	$-6.48 \cdot 10^3$	$-7.78 \cdot 10^2$	$-7.26 \cdot 10^3$
	Total	$1.56 \cdot 10^6$	$8.81 \cdot 10^4$	$1.64 \cdot 10^6$	$1.43 \cdot 10^6$	$-1.29 \cdot 10^4$	$1.42 \cdot 10^6$
Propeller 2 (PBCF)	*Propeller*	$1.56 \cdot 10^6$	$8.77 \cdot 10^4$	$1.64 \cdot 10^6$	$1.44 \cdot 10^6$	$-1.22 \cdot 10^4$	$1.43 \cdot 10^6$
	Hub & PBCF	$-5.36 \cdot 10^3$	$5.28 \cdot 10^2$	$-4.83 \cdot 10^3$	$-6.64 \cdot 10^3$	$-1.06 \cdot 10^3$	$-7.70 \cdot 10^3$
	Total	$1.55 \cdot 10^6$	$8.82 \cdot 10^4$	$1.64 \cdot 10^6$	$1.43 \cdot 10^6$	$-1.32 \cdot 10^4$	$1.42 \cdot 10^6$
Propeller 3	*Propeller*	$1.53 \cdot 10^6$	$9.29 \cdot 10^4$	$1.63 \cdot 10^6$	$1.43 \cdot 10^6$	$-1.29 \cdot 10^4$	$1.42 \cdot 10^6$
	Hub & Hubcap	$2.11 \cdot 10^1$	$3.68 \cdot 10^2$	$3.70 \cdot 10^2$	$-1.07 \cdot 10^4$	$-7.94 \cdot 10^2$	$-1.15 \cdot 10^4$
	Total	$1.53 \cdot 10^6$	$9.33 \cdot 10^4$	$1.63 \cdot 10^6$	$1.42 \cdot 10^6$	$-1.37 \cdot 10^4$	$1.41 \cdot 10^6$
Propeller 3 (PBCF)	*Propeller*	$1.53 \cdot 10^6$	$8.89 \cdot 10^4$	$1.62 \cdot 10^6$	$1.43 \cdot 10^6$	$-1.23 \cdot 10^4$	$1.42 \cdot 10^6$
	Hub & PBCF	$-6.08 \cdot 10^3$	$5.16 \cdot 10^2$	$-5.56 \cdot 10^3$	$-7.68 \cdot 10^3$	$-1.07 \cdot 10^3$	$-8.75 \cdot 10^3$
	Total	$1.52 \cdot 10^6$	$8.94 \cdot 10^4$	$1.61 \cdot 10^6$	$1.42 \cdot 10^6$	$-1.34 \cdot 10^4$	$1.41 \cdot 10^6$

Difference in energy losses without and with the Propeller Hub Cap Fins in the different rings

blob:https://web.whatsapp.com/5e4d0059-f0b4-4e91-b8cd-949b1cffaaf5

Table C.3: The difference between the results of the simulations without and with the PBCF normalized by the volume fraction

	Propeller 2				Propeller 3			
	IAXL	*AAXL*	*ROTL*	*VISL*	*IAXL*	*AAXL*	*ROTL*	*VISL*
Ring 1	0.003	-0.010	-0.064	0.005	0.005	-0.012	-0.076	0.001
Ring 2	0.002	-0.001	-0.003	0.000	0.001	-0.001	0.000	0.000
Ring 3	0.002	0.000	0.000	0.000	0.002	0.001	0.000	0.000
Ring 4	0.001	0.001	0.000	0.000	0.002	-0.001	0.000	0.000
Ring 5	0.001	0.000	0.000	0.000	0.000	0.000	-0.001	0.000